Coordination Chemistry Reviews 549 (2026) 217365

Contents lists available at ScienceDirect

Coordination Chemistry Reviews

journal homepage: www.elsevier.com/locate/ccr

Review

Electrochemical and spectroelectrochemical investigation of the chemical, structural and electronic properties of molecular metal carbonyl nanoclusters☆

Tiziana Funaioli [a,*], Marco Bortoluzzi [b], Giulio Bresciani [a], Cristiana Cesari [c], Cristina Femoni [c], Maria Carmela Iapalucci [c], Stefano Zacchini [c,*]

[a] Dipartimento di Chimica e Chimica Industriale, Università di Pisa, Via G. Moruzzi 13, 56124, Pisa, Italy
[b] Dipartimento di Scienze Molecolari e Nanosistemi, Ca' Foscari University of Venice, Via Torino 155, 30175 Mestre, Ve, Italy
[c] Dipartimento di Chimica Industriale "Toso Montanari", Università di Bologna, Via P. Gobetti 85, 40129 Bologna, Italy

ARTICLE INFO

Dedicated to Professor Resnati, celebrating a career in chemical bonds on the occasion of his 70th birthday.

Keywords:
Cluster compound
Carbonyl ligand
Electrochemistry
Molecular metal nanocluster
Spectroelectrochemistry

ABSTRACT

Electrochemical and spectroelectrochemical (SEC) techniques are widely employed in inorganic, coordination and organometallic chemistry. Nanoelectrochemistry and, in particular, the electrochemical study of atomically precise ligand protected metal nanoclusters has received great interest in the last decade. Molecular metal carbonyl clusters (MMCCs) are low valent atomically precise nanoclusters protected on the surface by a layer of CO ligands. Their metal cores may comprise from a few to some tens of metal atoms. Several electrochemical and SEC methods may be employed to study the redox properties of MMCCs. The reversible redox activity of MMCCs may originate from *ad hoc* conditions, in the case of lower nuclearity clusters, or incipient metallization of their metal core, as their sizes increase. Besides supplying information on the electronic and redox properties of MMCCs, electrochemical and SEC studies, supported by chemical, structural and computational investigation, can shed light on the structural changes induced by redox reactions of MMCCs. Moreover, the redox properties of MMCCs may be tuned by tailored chemical modifications. As *a bonus*, electrochemistry may be used to indirectly proof the hydride nature of larger MMCCs. Further information on the chemical properties of MMCCs may be gathered combining electrochemical, SEC, chemical, spectroscopic, structural and computational studies. This review will cover these different aspects of the electrochemical investigation of MMCCs, by exploring general principles and representative examples.

1. Introduction

It is difficult to overestimate the importance of electrochemistry in the landscape of fundamental research and of application areas [1,2]. A variety of novel and multi-disciplinary electrochemical techniques are available today and are applied in various fields of chemistry, biology and physics, such as: electrochemical energy storage and conversion, corrosion protection, electrolytic organic or inorganic processes for fine chemicals or large industrial scale productions, metal plating, modern electroanalytical techniques (sensors and biosensors), electrochemistry applied to biological systems (energy transfer and uses in cells, cellular communication, biological redox processes, electrocatalysis). All these applications require a fundamental knowledge of the electrochemical behavior of the different species involved.

Electrochemical techniques have been widely applied to the investigation of inorganic, coordination and organometallic compounds. Indeed, inorganic electrochemistry is nowadays well-developed and can give several information on the redox properties of inorganic compounds, for fundamental and applicative purposes [3–5]. Among the different classes of inorganic compounds that can be electrochemically studied, molecular metal nanoclusters are attracting an increasing interest, and nanoelectrochemistry is becoming of paramount relevance [6]. This is somehow due to the recent developments of nanochemistry, particularly regarding atomically precise metal nanoclusters. Several papers and reviews on this topic have appeared in the last years, mainly focusing on ligand protected coinage metal molecular nanoclusters

☆ This article is part of a Special issue entitled: 'Chemical Bonds' published in Coordination Chemistry Reviews.

* Corresponding authors.
E-mail addresses: tiziana.funaioli@unipi.it (T. Funaioli), stefano.zacchini@unibo.it (S. Zacchini).

https://doi.org/10.1016/j.ccr.2025.217365
Received 2 October 2025; Received in revised form 5 November 2025; Accepted 5 November 2025

[7–17]. Also, the electrochemistry of such coinage metal nanoclusters has been studied, concerning both fundamental aspects as well as their applications in electrocatalysis and electrochemical sensing [18–23].

Molecular metal carbonyl clusters (MMCCs) represent another class of atomically precise metal nanoclusters, which is nowadays well-developed [24–37]. MMCCs are composed of a metal core, usually in a low-oxidation state (formally zero or slightly negative), protected on its surface by high-field CO ligands. Other ligands (such as phosphines) may be present in the coordination sphere of MMCCs, and main group elements can be found on their surfaces as well located within their metal cores in semi-interstitial and fully interstitial positions. The overall sizes of MMCCs are usually comprised in the 0.9–2.1 nm range, as for ultrasmall metal nanoparticles, atomically precise metal nanoclusters and ligand protected coinage metal molecular nanoclusters [38].

The study of MMCCs has largely contributed to Cotton's definition of metal clusters and to the development of the cluster-surface analogy by Muetterties [39–41]. The redox properties of MMCCs have been investigated by electrochemical and spectroelectrochemical (SEC) methods [42–52]. It has been shown that larger MMCCs are often redox active displaying several reversible redox processes. Along this review, we will often refer to such redox active MMCCs as electron-sinks, electron-sponges or multivalent clusters. In view of this electron-sink behavior and their nanometric dimensions, multivalent MMCCs may be viewed as molecular nanocapacitors, whose metal core, protected by an insulating layer of CO ligands, may be charged and discharged at well-defined potentials, by the addition/removal of one-electron per time.

Several reviews on the electrochemistry of MMCCs have appeared before the year 2003 [43–49,51,52]. The most recent reviews on this topic have been published by Longoni *et al.* and Zanello *et al.* between 2006 and 2012 [4,42,50]. Since then, different research papers on electrochemical and SEC investigation of MMCCs have been added to the literature. Moreover, MMCCs have found interesting applications in electrocatalysis in recent years, mainly thanks to the work of Berben and co-workers [53–58].

Since electrocatalysis by MMCCs has been recently reviewed [25], we have focused the present review on the electrochemical and SEC methods for the investigation of MMCCs, and the information that can be obtained concerning their chemical, structural and electronic properties. After this brief Introduction, Section 2 will be dedicated to the description of the main electrochemical and SEC methods for the investigation of MMCCs, concerning their setup and experimental aspects, as well as the different techniques that can be used, and the information that can be obtained. Section 3 will present an investigation of the electronic properties of MMCCs by electrochemistry, including both general considerations on the electronic and redox status of the metal core of MMCCs with increasing sizes, as well as some representative examples of multivalent MMCCs. The interplay between electrochemical properties and structural features of MMCCs will be discussed in Section 4, focusing both on the structural changes induced by redox reactions on MMCCs, and on the effects of structural changes on the redox properties of MMCCs. Further chemical information obtained by electrochemical studies of MMCCs will be briefly included in Section 5. All along this review, we will refer (somehow arbitrarily) to low, mid and high nuclearity MMCCs within the following ranges (which should be taken very roughly) of metal atoms: <10 (low), 10–20 (mid), >20 (high). All the electrochemical potentials along with the text have been reported relative to SCE.

2. Electrochemical and spectroelectrochemical methods for the investigation of MMCCs

MMCCs exhibit rich redox properties, and electrochemistry has become a readily available routine technique for their characterization. Like the various spectroscopies, so the different electrochemical techniques provide unequivocal fingerprints of the clusters [4,51,59]. Moreover, giving prompt information about the existence and the relative stability of different redox states of the clusters, electrochemical studies can guide and facilitate the work of the synthetic chemist.

The investigation of the redox behavior of MMCCs requires a careful experimental setup and a comprehensive approach combining various electrochemical and SEC techniques (Table 1). These systems, often sensitive to air and moisture and prone to decomposition upon redox changes, demand specific attention in terms of solvent selection, electrode configuration, and cell design.

2.1. Electrochemical setup and experimental considerations

Electrochemical measurements are typically carried out in water or in aprotic organic solvents such as dichloromethane, acetone, acetonitrile, dimethylsulfoxide (DMSO), dimethylformamide (DMF) or tetrahydrofuran (THF), which are often selected for their wide electrochemical windows, low viscosity, and good solubility for both the analyte and the supporting electrolyte [60,61] When a MMCC is investigated, the use of an aprotic organic solvent is mandatory and it is important to select a solvent that can be rigorously dried and deoxygenated prior to use. The presence of residual water can lead to parasitic proton-coupled reactions or hydrolysis of sensitive species, while dissolved oxygen is electroactive and may be reduced at the working electrode, giving rise to overlapping signals and consumption of reactive intermediates. Furthermore, oxygen can oxidize reduced forms of MMCCs or promote decomposition of low-valent species, compromising both spectral and voltammetric analyses. For these reasons, electrochemical solvents are typically purified by distillation over drying agents under inert atmosphere, stored on molecular sieves and transferred using standard Schlenk techniques [62–64].

To ensure sufficient ionic conductivity, especially in organic solvents such as CH_2Cl_2 or THF where conductivity is inherently low, by minimizing solution resistance and suppressing migration currents, the use of a proper supporting electrolyte is fundamental. Generally, supporting electrolytes should be chosen to have a high solubility in the solvent and to not interfere with the redox processes and/or with the species in solution. In this context, tetraalkylammonium salts of weekly coordinating anions (e.g., hexafluorophosphate, perchlorate, tetrafluoroborate) are the best choice due to the tunability of the chain length (less polar is the solvent, longer should be the alkyl chain) [63,64].

Proper control of ohmic drop and uncompensated resistance is necessary, especially when working with high currents, in low-conductivity media, or at low temperatures. To ensure accurate and stable measurements, electrochemical experiments are typically performed using a three-electrode cell configuration (working-, reference- and counter-electrode) which allows independent control and monitoring of the applied potential and the current flow [62,65].

In this setup, the working electrode (WE) is where the redox process of interest occurs [4,61,66]. It is usually made of inert conductive materials such as Pt, Au, or glassy carbon (GC), the latter being particularly valued for its wide potential window and low background current. In voltammetric experiments, the WEs have usually a flat surface and it is helpful to know their surface area; if the electrode is well polished, so there are no jagged edges or grooves, the geometric area of the electrode is close to the true surface area.

The reference electrode (RE) serves as a stable, known potential against which the WE potential is measured [61,67,68]. This electrode should pass minimal current to maintain its potential stability throughout the experiment, the potentiostat limits the amount of current that can pass between the two electrodes to nearly zero**.** In non-aqueous media, saturated calomel (SCE) or silver/silver chloride (Ag/AgCl) electrodes are in common use, provided that their tips are isolated from the cell solution to prevent the leakage of water and chloride. For this purpose, the tip should be dipped in a salt bridge separated with a porous frit and filled with the organic electrolyte solution. In organic media, Ag/Ag^+ electrodes can use as solvent the same of the electrolytic

Table 1
Information obtained and limitations of electrochemical techniques commonly used for the characterization of MMCCs.

Technique	Information obtained	Limitations
Cyclic Voltammetry (CV)	Number of redox events; formal redox potentials; electron transfer stoichiometry; electrochemical/ chemical reversibility; kinetics of electron transfer and coupled chemical reactions.	Overlapping redox waves; adsorption on electrode surface; low diffusion coefficients of large clusters; solvent discharge hides processes at extreme potentials; electrode material strongly affects kinetics.
Differential Pulse Voltammetry (DPV)	Higher sensitivity and resolution than CV; accurate determination of formal potentials; deconvolution of overlapping redox events.	Operates at very low scan rates ($\leq$0.02 V s^{-1}); unsuitable for unstable intermediates or fast follow-up reactions; signal depends on electrode surface; long timescale may allow side reactions.
Square Wave Voltammetry (SWV)	Fast and sensitive detection of redox processes; suitable for systems with rapid chemical complications; deconvolution of closely spaced events.	Data interpretation complex (differential current); challenging in quasi-reversible systems; strong dependence on pulse parameters; residual capacitive contributions affect accuracy.
Electrochemical Impedance Spectroscopy (EIS)	Charge transfer resistance; kinetics of electron transfer; ion diffusion; interfacial phenomena via equivalent circuit models.	Requires steady-state and linearity; model fitting can give ambiguous results; time-consuming and noise-sensitive at low frequencies.
Infrared Spectroelectrochemistry (IR-SEC)	Direct monitoring of structural and electronic changes; ν_{CO} shifts indicate electron density variation; number of electrons exchanged per step; correlation with CV for oxidation state assignment.	Requires specialized OTTLE cells and optically transparent electrodes; OTTLE cells require thorough washing and refilling for each experiment, even when using the same solution; sensitive to gas evolution, product precipitation, or electrode fouling; pseudo-reference potential not fixed.
UV–Vis–NIR Spectroelectrochemistry	Real-time monitoring of electronic transitions; HOMO–LUMO gap estimation; tracking of transient species and charge delocalization.	Poorly resolved spectra for high-nuclearity clusters; broad absorption bands; experimental setup requires transparent electrodes and suitable windows; limited by TD-DFT accuracy for excited states.
EPR Spectroelectrochemistry	Site of redox activity; orbital contributions; spin multiplicity; useful for unstable paramagnetic intermediates.	Requires paramagnetic species; radicals often short-lived; *ex situ* measurements need stringent inert conditions; *in situ* applications still limited.

solution where the experiment is carried out (often consisting of a silver wire immersed in a solution of $AgNO_3$ or $AgPF_6$ in CH_3CN), however, the equilibrium potential of these electrodes is not well-defined and stable as required for a good RE. For the use in organic solvents, we found the leakless Ag/AgCl, reference electrodes robust, highly conductive but not porous, with the equilibrium potential stable for long times.

The counter electrode (CE), often a Pt wire, completes the circuit by allowing current to flow between itself and the WE. It must have a sufficiently large surface area to prevent kinetic issues. CE is placed directly in the solution under study in voltammetric experiments, while is far away from the WE, in a separate compartment, *e.g.* isolated by a porous frit, in controlled potential electrolysis to prevent redox by-products generated by the reaction that occurs on it from diffusing at the WE, where they could interfere with the analyte or affect the measurement.

Before the use, the electrochemical cell must be thoroughly dried, typically by heating in an oven (e.g., 120 °C) to remove any adsorbed moisture, especially when working in organic solvents or with air-sensitive compounds such as anionic MMCCs. In these cases, the cell can be equipped for use under an inert atmosphere using standard Schlenk techniques. This includes fitting the cell with ground-glass joints, septa, and gas inlets/outlets to allow for evacuation and back-filling with inert gas (Ar or N_2), ensuring complete exclusion of moisture and oxygen during the electrochemical measurements. As stated above, inert atmosphere is essential to prevent undesired electrochemical events, but also to exclude oxidation or hydrolysis of sensitive cluster species.

In the experimental set up assembly it must be kept in mind that working with MMCCs can cause gas evolution (e.g., CO release) upon reduction or oxidation.

2.2. Techniques and their diagnostic power

Cyclic voltammetry (CV) is a widely used electroanalytical technique that involves applying a linearly varying potential to a WE while measuring the resulting current under diffusion-controlled mass transfer [69,70]. The potential is swept between two set limits at a defined scan rate, and then reversed back to the initial value, resulting in a cyclic potential waveform. The resulting current–potential plot (voltammogram) reflects the redox behavior of electroactive species near the WE surface. Key features of the voltammogram include peak currents, peak potentials, and peak shapes. These parameters can be used to provide rich information on electron transfer processes, including their thermodynamic (formal redox potentials) and kinetic (rate of electron transfer) data, stoichiometry (number of exchanged electrons), chemical reversibility (stability of electrogenerated species), and kinetic and mechanistic information of the chemical reactions coupled to electron transfers.

CV remains the most accessible and informative technique for probing the redox properties of MMCCs. It provides immediate information on the number of redox processes, the formal potentials, and the electrochemical and chemical reversibility of electron transfers. However, interpreting CV profiles of MMCCs can be challenging. Overlapping redox events, formation of unstable intermediates, and adsorption on the electrode surface often complicate the analysis. Moreover, solubility issues or low diffusion coefficients of high nuclearity MMCCs can result in low intensity peak currents and ill-defined CV profiles. In several cases, however, the low currents did not depend on insufficient cluster solubility in the experimental conditions, as solutions with concentrations higher than 1 mM could be prepared for the compounds, or on the material of WE (Pt or GC), but rather by slow kinetic of electrode reactions [71].

A clear example can be found comparing voltammograms of $[Pt_{40}(CO)_{40}]^{6-}$ and $[Pt_{33}(CO)_{38}]^{2-}$ clusters, which exhibit a rich electrochemistry (Fig. 1) [72]. Both these clusters display a series of redox events involving up to seven oxidation states, however voltammetric

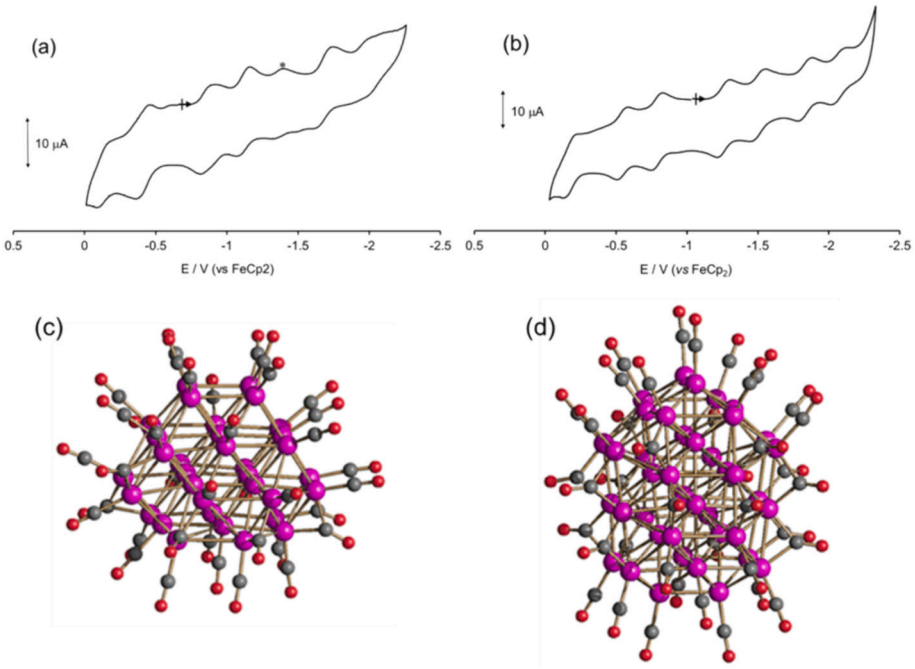

Fig. 1. CV at a Pt electrode in CH_3CN solution ($[N^nBu_4][PF_6]$ (0.1 mol dm^{-3}) as supporting electrolyte; scan rate: 0.1 V s^{-1}) of (a) $[Pt_{33}(CO)_{38}]^{2-}$ and (b) $[Pt_{40}(CO)_{40}]^{6-}$; molecular structure of (c) $Pt_{33}(CO)_{38}]^{2-}$ and (d) $[Pt_{40}(CO)_{40}]^{6-}$ (purple, Pt; red, O; grey, C). Adapted with permission from Ref. [72]. Copyright 2016 American Chemical Society.

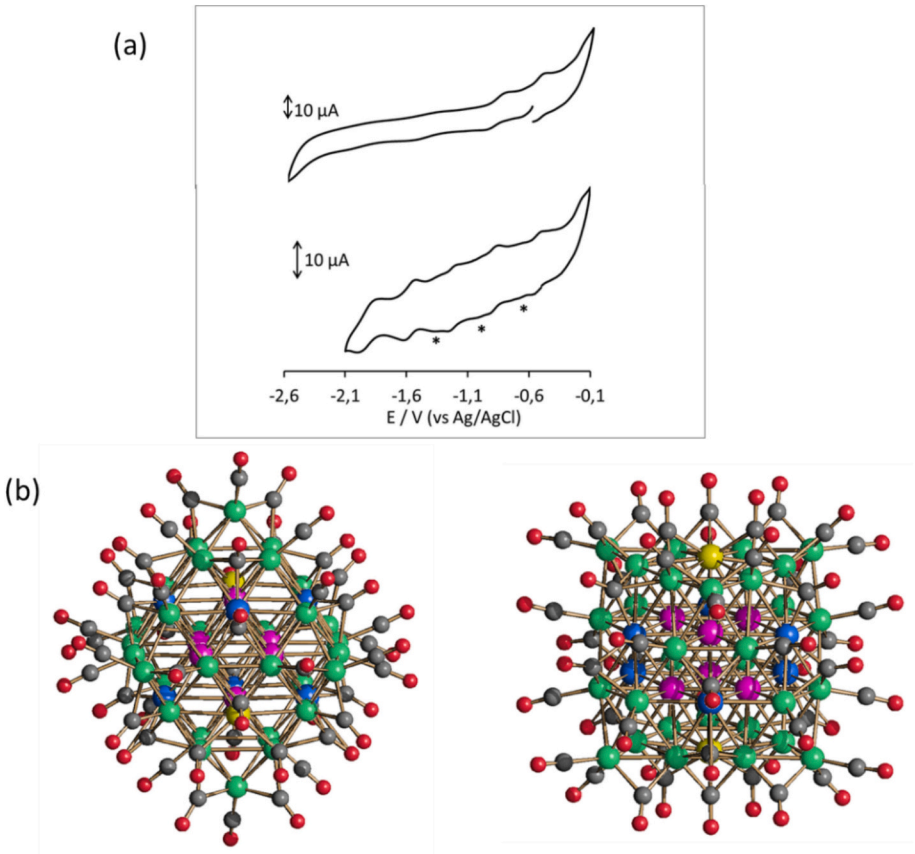

Fig. 2. (a) Comparison of CV profiles of $[HNi_{37-x}Pd_{7+x}(CO)_{48}]^{5-}$ (x = 0.53) recorded at Pt (top) and GC (bottom) WE in CH_3CN solution. $[N^nBu_4][PF_6]$ (0.1 mol dm^{-3}) supporting electrolyte. Scan rate: 0.1 V s^{-1}. Starred peaks are attributable to unknown impurities. (b) The molecular structure of the first independent molecule of $[HNi_{37-x}Pd_{7+x}(CO)_{48}]^{5-}$ (x = 0.53). Two views are reported (green, Ni; purple, Pt, yellow, Ni/Pd≈ 42:58; blue, Ni/Pd≈ 88–92:12–8; grey, C; red, O). Adapted with permission from Ref. [71]. Copyright 2021 American Chemical Society.

profile has been found to be more complicated in the case of $[Pt_{33}(CO)_{38}]^{2-}$ respect to $[Pt_{40}(CO)_{40}]^{6-}$. Redox changes show features of chemical reversibility and electrochemical quasi-reversibility for the former cluster, whereas almost all the redox processes exhibited by the more regular $[Pt_{40}(CO)_{40}]^{6-}$ are chemically and electrochemically reversible. This behavior was linked to the defective close-packed (*ccp*) structure of $[Pt_{33}(CO)_{38}]^{2-}$, which influences the electronic delocalization and stabilization of the redox states. This study exemplifies how CV can uncover intricate electron-transfer patterns in high-nuclearity MMCCs. However, it also highlights limitations such as the observation of quasi-reversible or irreversible steps because of structural reorganization or decomposition, and the impossibility to detect redox events at high or low potentials, hidden under the solvent discharge.

Another parameter that must be kept in mind setting up these measurements, is the nature of the electrode material that can influence the voltammetric response. For example, studies on hydride Ni–Pd carbonyl clusters [71] have shown that switching between Pt and GC electrodes can result in different current–potential behaviors due to changes in adsorption and electron-transfer kinetics. When a Pt electrode was used, a slower kinetic rate, respect to the GC electrode, was observed. This decrement in kinetic rate led to a decrease in the current intensity and, thus, to ill-defined peaks (Fig. 2).

Under diffusion-controlled conditions, the Randles–Ševčík equation relates the peak current to the scan rate, the number of electrons transferred and diffusion coefficient of the analyte [4,69]. Therefore, CV can be employed to determine the number *n* of electrons exchanged in each redox event or the diffusion coefficient when one of the two quantities is known. In several cases, the peak current of the investigated process is compared, under the same experimental conditions, with that of a compound, having similar diffusion coefficient, for which *n* in known. However, the application of this equation is subjected to several limitations. It assumes that the electrochemical process is reversible, diffusion-controlled, and that no coupled chemical reactions or adsorption phenomena are involved.

In the case of MMCCs, these assumptions are not always met. In fact, many clusters undergo follow-up chemical reactions after electron transfer, such as CO loss or rearrangement, which lead to deviations from ideal voltammetric behavior. Irreversibility, peak broadening, and distorted voltammograms are common in such systems, making the direct application of the Randles–Ševčík equation potentially misleading. Moreover, adsorption of the cluster or its reduced/oxidized forms on the electrode surface, especially on Pt, can invalidate the assumption of diffusion control, leading to over- or underestimation of the number of electrons transferred.

Thus, while the Randles–Ševčík equation provides a valuable first approximation, its results must be interpreted cautiously and ideally corroborated with complementary techniques or simulation of voltammetric profiles. Careful evaluation of scan-rate dependence and peak separation can help assess whether the conditions for valid application of the equation are satisfied.

Hydrodynamic voltammetry uses convection to enhance the rate of mass transport of species towards the electrode surface [73,74] Some hydrodynamic methods are based on electrodes that move with respect to the electrolytic solution, as with rotating electrodes, whereas in other hydrodynamic systems the electrolytic solution flows over a static electrode. A typical voltammetric measurement used with the rotating disc and other hydrodynamic systems is linear sweep voltammetry at low scan rates. When the electrode rotates in a stable speed during the measurement, the total current flowing depends upon the rotation speed used and the system reaches a steady state and so the current reaches a plateau; in clusters featured by multiple redox processes a stepped current-voltage curve is obtained, with the same height of each step pointing the same number of transferred electrons.

Differential pulse voltammetry (DPV) and *square wave voltammetry* (SWV) are pulse-based electroanalytical techniques that apply periodic perturbations to the potential during a voltammetric scan, enhancing signal-to-noise ratios and enabling the detection of redox processes with greater precision than conventional CV. In DPV, a series of small potential pulses is superimposed on a slowly varying base potential, while in SWV, symmetrical forward and reverse pulses are applied around a staircase potential, allowing for fast and sensitive measurements [4,61,75]

These techniques offer greater sensitivity and resolution compared to conventional CV, enabling the deconvolution of overlapping redox waves and, therefore, are particularly valuable for high-nuclearity MMCCs, which often exhibit dense series of redox events with closely spaced formal potentials. By minimizing capacitive current contributions and enhancing faradaic signals, DPV and SWV can resolve individual electron transfer steps that would otherwise appear as merged or broadened peaks in cyclic voltammograms (Fig. 3) [76–80].

However, both techniques have some specific limitations. DPV, while excellent for determining accurate formal potentials of closely spaced redox couples, typically operates at very low scan rates (e.g., $\leq$0.02 V s^{-1}). This slow potential ramp makes it unsuitable for studying unstable intermediates or processes involving rapid chemical follow-up reactions, as the long timescales can allow decomposition or side reactions to occur during measurement. Additionally, the signal shape and intensity may vary depending on electrode material and cleanliness.

SWV, particularly in its Osteryoung variant (OSWV) [81], allows for higher scan rates (typically 0.2–1 V s^{-1}) and is thus more suitable for systems where chemical complications could interfere at longer timescales. Nevertheless, the interpretation of SWV data can be more complex, as it involves a differential current response obtained from forward and reverse pulses. This can make distinguishing electrochemical and chemical contributions challenging, especially in the case of non-ideal or quasi-reversible systems.

In both methods, the precise control of parameters such as pulse height, duration, and step size is critical for obtaining reproducible and interpretable data. Moreover, the accuracy of current measurements may be affected by residual capacitive contributions, especially when working with very low current signals typical of dilute solutions of MMCCs.

Controlled potential electrolysis provides the best method to measure the number *n* of electrons involved in a redox process. The charge passed in an electrolytic cell in correspondence of a redox process, up to complete depletion of the starting compound, is related to the number *n* of exchanged electrons *per* mole of compound by Faraday law [4,64]. The electrolysis experiments are carried out at applied potentials, which are 0.1-0.2 mV more negative (or positive) with respect to the peak potential of the reduction (or oxidation) process in the CV of the redox active species, and must be performed in cells with anodic and cathodic compartments separated by a porous frit to prevent products formed at CE from contaminating or falsifying the process at WE. A WE with a high surface area is employed to ensure that electrolysis times are not too long. When the product of electrolysis is stable, the CV on the exhaustively electrolyzed solution gives a voltammogram quite complementary to that of the starting compound, and, as far as the hydrodynamic voltammetry is concerned, the wave has the same height, but results shifted on the current axis. In cases where the electrogenerated species are of limited stability and decompose during the long times of electrolysis, the electron stoichiometry can be verified by the fast addition of equimolar amounts of an oxidizing or reducing agent meanwhile controlling, by hydrodynamic voltammetry, the anodic or cathodic shift of the current axis [82], according to the quantitative product formation.

Electrochemical impedance spectroscopy (EIS), is a powerful technique that analyses the frequency-dependent response of an electrochemical system to a small alternating current [61]. It provides detailed information on charge transfer kinetics, ion diffusion, and interfacial phenomena by modelling the system with equivalent electrical circuits. Despite its strengths, EIS requires steady-state conditions and assumes linearity and time-invariance, assumptions not always valid for unstable or reactive species. The analysis often depends on model fitting, which

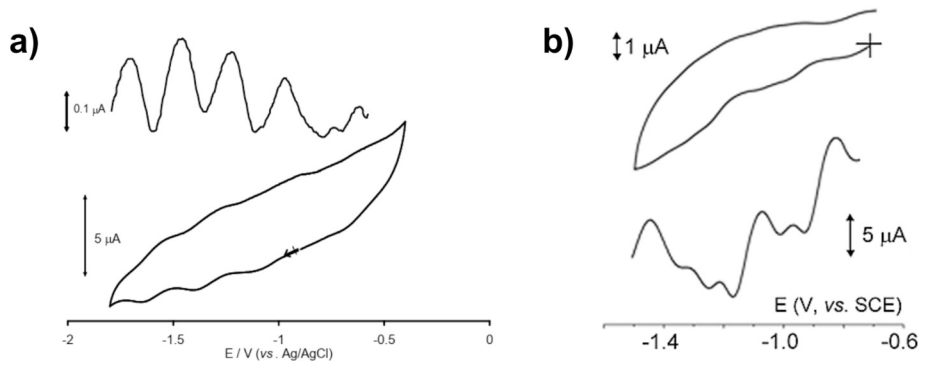

Fig. 3. (a) CV (bottom) and DPV (top) profiles recorded at Pt electrode in CH_3CN solution of $[Ni_{29-x}Pd_{6+x}(CO)_{42}]^{6-}$ (x = 0.09). Adapted from Ref. [80], with permission from The Royal Society of Chemistry. (b) CV (top) and SWV (Osteryoung variant, bottom) profiles recorded at a GC electrode in CH_3CN solution of $[HNi_{36}C_8(CO)_{36}(Cd_2Cl_3)]^{4-}$. Adapted from Ref. [79] with permission from Wiley.

can lead to ambiguous interpretations, and measurements at low frequencies can be lengthy and noise-sensitive. The first examples of EIS analysis employed in MMCC field were reported in 2021 and 2022 on three different Ni-Pd clusters [71], $[Pt_{19}(CO)_{22}]^{4-}$ and $[Pt_{27}(CO)_{31}]^{4-}$ [83].

The charge transfer resistance R_{ct} at the potential of the redox process is directly related to the kinetics of the electrochemical reaction and can be obtained by fitting the experimental data with the Randles circuit (Fig. 4A). In particular, EIS measurements of clusters were performed both at a GC and at a Pt WEs to investigate the different kinetic on each electrode type. When the same resolved CV profile was obtained on both WEs [71], R_{ct} values for the same redox peak were similar (about 1 kΩ) indicating relatively fast electron transfers for $[Ni_{36-x}Pd_{5+x}(CO)_{46}]^{6-}$ (x = 0.41) at both the electrodes (Fig. 4). On the contrary, in the case of $[HNi_{37-x}Pd_{7+x}(CO)_{48}]^{5-}$ (x = 0.53) lower and broader current peaks in CV were observed for Pt with respect to GC electrode (Fig. 2); correspondingly a higher impedance value for the first one (R_{ct} about 5-42 kΩ) suggested a slower kinetic towards that electrode material (Fig. 5). Moreover, we found that EIS measurements at the potentials of the five consecutive reductions lead to a slower kinetic behavior for $[HNi_{37-x}Pd_{7+x}(CO)_{48}]^{n-}$ (x = 0.53; n = 5-10) also on GC WE [71], for the redox processes at the two more negative potentials. This can be explained by supposing important structural modification of the cluster as the number of added electrons increases, as confirmed by the variation of the relative intensity of the terminal and bridging ν_{CO} bands in favor of the bridging ones during the IR SEC experiments in the same range of potentials. Also, an increase in the metal-metal bond distances as the cluster negative charge increases is expected for multivalent carbonyl compounds [84]. This topic is further discussed in Section 4.1.

Simulation of electrochemical processes is a powerful approach to test a theoretical model of electrochemical behavior, particularly in systems involving complex electron transfer mechanisms and coupled chemical reactions [4,75,85,86]. The modelling of voltammetric experiments requires the definition of the system under study in terms of mass

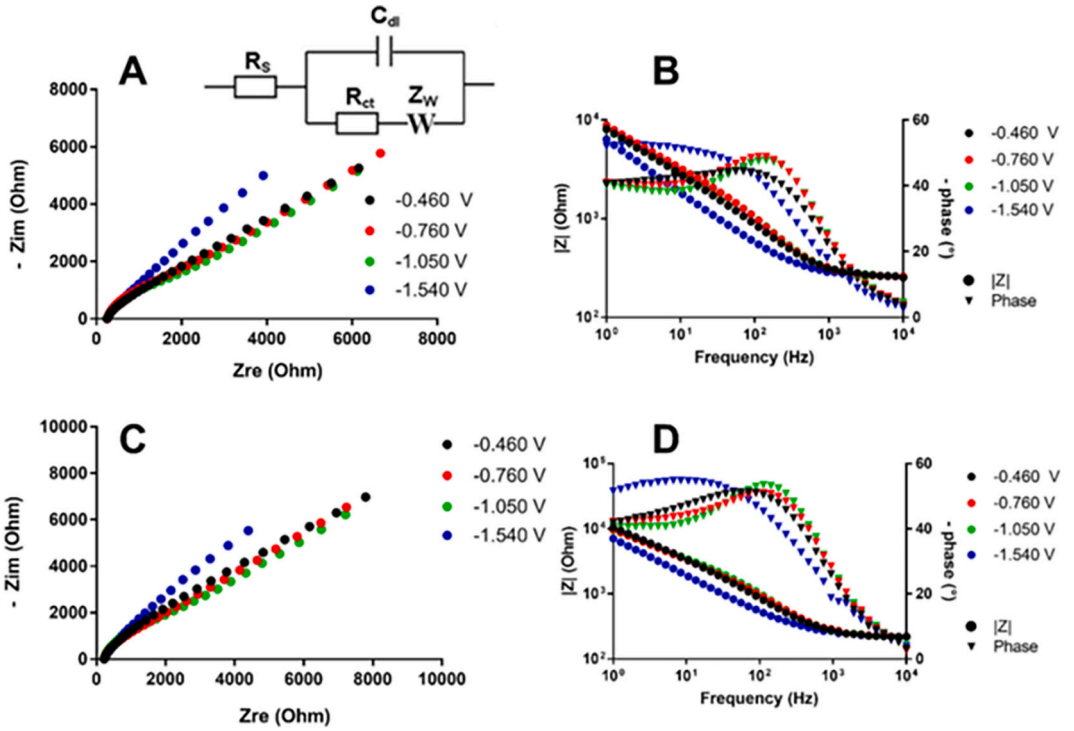

Fig. 4. A) Nyquist plot for $[Ni_{36-x}Pd_{5+x}(CO)_{46}]^{6-}$ (x = 0.41) using Pt electrode. B) Bode plot using Pt electrode. C) Nyquist plot for $[Ni_{36-x}Pd_{5+x}(CO)_{46}]^{6-}$ (x = 0.41) using GC electrode. D) Bode plot using GC electrode. The working potentials for each curve were –0.460 V (black dots), –0.760 V (red dots), –1.050 V (green dots), and –1.540 V (blue dots). Adapted with permission from Ref. [71]. Copyright 2021 American Chemical Society.

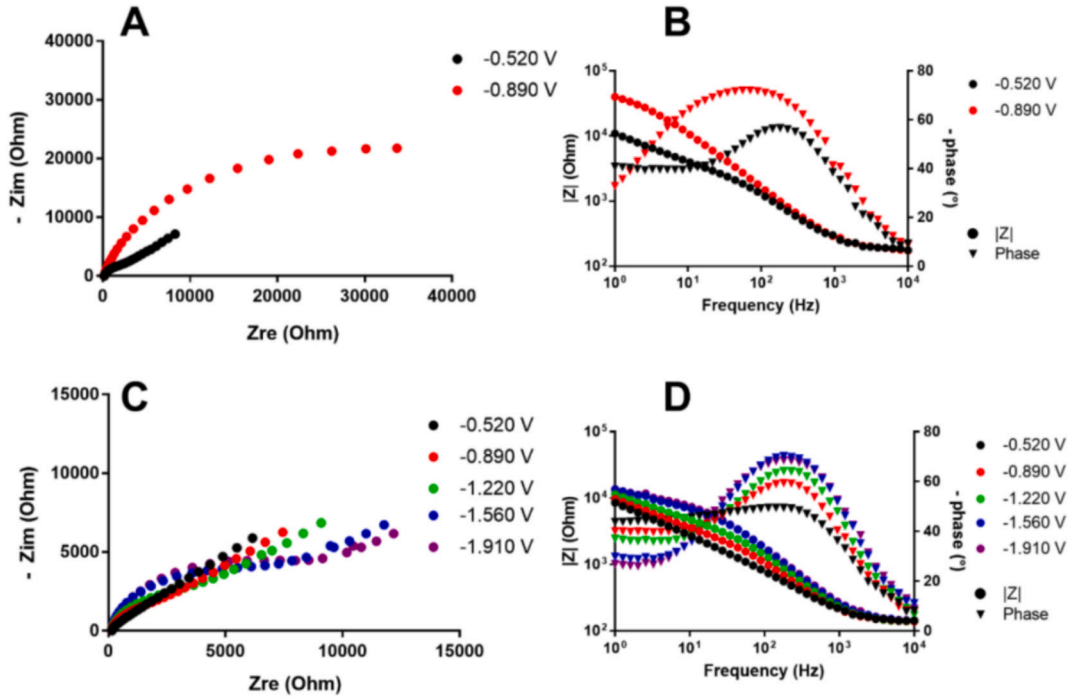

Fig. 5. A) Nyquist plot for $[HNi_{37-x}Pd_{7+x}(CO)_{48}]^{5-}$ (x = 0.53) using Pt electrode. B) Bode plot using Pt electrode. C) Nyquist plot for $[HNi_{37-x}Pd_{7+x}(CO)_{48}]^{5-}$ (x = 0.53) using GC electrode. D) Bode plot using GC electrode. The working potentials for each curve were –0.520 V (black dots), – 0.890 V (red dots), –1.220 V (green dots), –1.560 V (blue dots), and –1.910 V (purple dots). Adapted with permission from Ref. [71]. Copyright 2021 American Chemical Society.

transport, adsorption on the electrode surface, homogeneous and/or heterogeneous chemical reactions, as well as of the electrical perturbation applied. Generally, simulations focus on homogenous processes and therefore, although all these phenomena can in principle be simulated, not all of them are usually included in the simulation. Numerical approaches typically solve Fick's laws of diffusion in combination with appropriate kinetic models such as Butler–Volmer or Marcus–Hush theory, enabling time-resolved computation of current responses to dynamic potential waveforms. These simulations can accommodate a wide variety of mechanistic pathways, including electron transfer (E), chemical steps (EC, CE), and catalytic cycles. A robust and broadly applicable simulator constitutes a valuable resource for capturing variations in kinetic and/or thermodynamic responses as a function of selected experimental parameters (e.g., scan rate). The ability to rapidly reproduce experimental conditions without physically assembling an electrochemical cell can provide significant advantages in research practice and facilitates the presentation of results in educational contexts. Such simulations enable the verification or exclusion of specific electrochemical mechanisms, thereby streamlining the interpretation of experimental data and supporting the development of mechanistic insights. Notably, the simulation of electrochemical processes can greatly assist in elucidating the mechanistic pathways of metal clusters that undergo multiple electron-transfer events [4,87–90], where experimental interpretation alone may be challenging. For instance, in the case of $[Co_4(CO)_3(\mu_3\text{-}CO)_3(\mu_3\text{-}C_7H_7)(\eta^5\text{-}C_7H_9)]$, the CV simulation allowed to confirm the electrochemical mechanism supposed on the experimental CV (Fig. 6) [88].

In recent years, several open-source tools have made CV simulation more accessible, allowing researchers to perform mechanistic studies, test hypotheses, and fit experimental data with increasing efficiency [85,91–93].

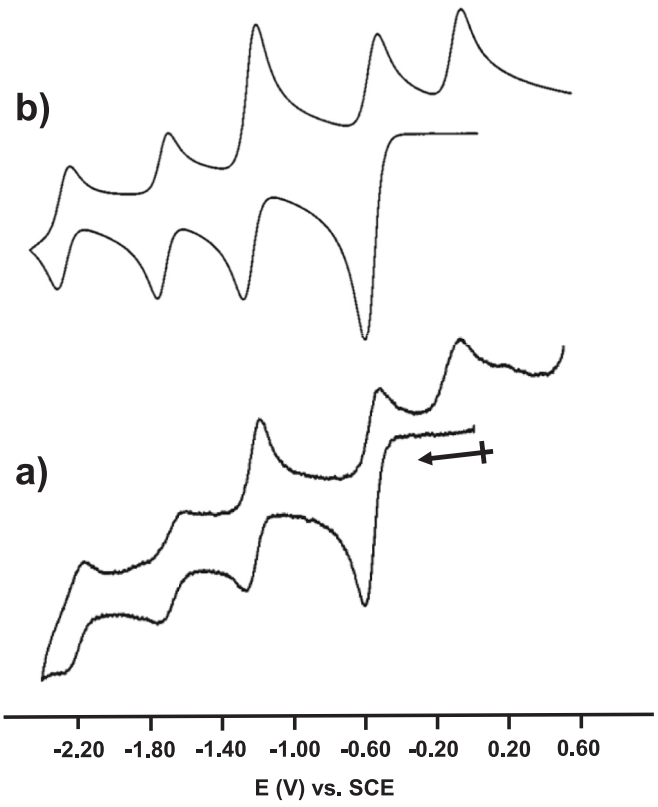

Fig. 6. Comparison of experimental (a) and simulated (b) CV of $[Co_4(CO)_3(\mu_3\text{-}CO)_3(\mu_3\text{-}C_7H_7)(\eta^5\text{-}C_7H_9)]$. Fig. adapted from [88] with permission from Wiley.

2.3. Spectroelectrochemical (SEC) approaches

Spectroelectrochemistry (SEC), thus the *in situ* simultaneous electrochemical and spectroscopic analysis of a redox reaction, allows to

combine important aspects as thermodynamic and kinetic of the electron transfer with techniques suitable for the identification of unknown reaction intermediates or products. Several absorption (ultraviolet, UV; visible, VIS; near-infrared, NIR; infrared, IR), emission (luminescence in UV or VIS regions), scattering (Raman) and resonance (electron paramagnetic resonance, EPR; nuclear magnetic resonance, NMR) spectroscopies are typical methods in SEC [4,94–96].

Since in a reversible one-electron electrode process either the starting species or the product must be paramagnetic, *in situ* EPR SEC is an ideal technique to gain information about the site of redox activity in the molecule, the contribution of specific nuclei to the molecular orbital hosting the unpaired electron, and the half-wave potentials of systems in which CV experiments provide ill-defined peaks due to slow electron-transfer kinetics [95]. While EPR spectra are often recorded *ex situ* on electrogenerated species, radicals frequently exhibit short lifetimes and/or high thermal reactivity; therefore, the transfer of radical solutions after external generation may require complex manipulations to exclude oxygen or moisture, or to maintain low temperatures [97]. A more widespread use of the *in situ* approach is highly desirable in future studies, especially for MMCCs that are very reactive species for which also the magnetic behavior of even-electron compounds is controversial [98]. Combined electrochemical EPR measurements can unambiguously determine the spin multiplicity of both redox partners, even in the case of unstable intermediates, while complementary UV-Vis or IR SEC can help assess the reversibility of the redox process and/or identify any subsequent chemical transformations. While some examples of combined EPR/UV-Vis SEC studies are reported [99,100], no examples were found in the literature for the EPR/IR version.

In situ scattering and resonance SEC techniques are considerably less employed compared to UV–Vis and IR SEC. For this reason, in this review we will focus our discussion in more detail on the latter spectroscopic methods.

Infrared spectroelectrochemistry (IR-SEC) is the most effective *in situ* technique that enables the monitoring of structural and electronic changes in MMCCs during electrochemical oxidation or reduction [95]. The ν_{CO} stretching vibrations are highly sensitive to changes in the electronic structure of the cluster: as electrons are added or removed, the electron density around the metal centers changes, altering the back-donation to the CO ligands and, thus, shifting the carbonyl stretching frequencies. Typically, a cathodic (reductive) process leads to a shift of the ν_{CO} bands to lower wavenumbers, due to increased back-donation from the more electron-rich metal center, whereas oxidation leads to a shift to higher wavenumbers, consistent with decreased electron density and reduced back-donation.

The number of electrons exchanged in each redox step can often be inferred from the magnitude of the ν_{CO} shift, particularly when supported by DFT calculations or comparison with chemically generated analogues. Indeed, one-electron redox processes of MMCCs cause an approximately constant shift of ν_{CO} after each addition or removal of one electron, while an almost double value is observed for two-electron transfers. Moreover, when combined with CV, IR-SEC allows for a direct correlation between the observed potential-dependent spectral changes and the redox processes identified voltammetrically. This enables accurate assignment of formal oxidation states and insights into the distribution of electron density within the metal core.

Despite its power and resolution, IR-SEC presents significant experimental challenges. A key requirement is the use of optically transparent electrodes (OTEs) which allow simultaneous IR transmission and electrochemical control. These electrodes are typically integrated into a specialized SEC cell, the optically transparent thin-layer electrode (OTTLE) cell [101], which has become one of the most widely used configurations for IR-SEC. In a typical OTTLE setup, the WE, such as a Pt or Au minigrid, is mounted within a polyethylene or Teflon spacer, sandwiched between two IR-transparent windows (*e.g.,* KBr, CaF_2, or ZnSe). The total cell pathlength is typically between 0.2 and 0.5 mm, enabling a thin-layer geometry that ensures rapid and complete electrolysis with high signal-to-noise ratios in the ν_{CO} region. Counter and pseudo-reference electrodes, often Pt mesh and Ag wire respectively, are embedded alongside the WE in the same narrow volume allowing fast, simultaneous electrochemical and spectroscopic monitoring. Furthermore, the thin-layer geometry prevents significant diffusion of redox by-products from the CE in the measuring space and towards the Ag pseudo-reference electrode so that the reference potential remains constant, although, being a pseudo-reference, the potential of this electrode is not defined and can change from experiment to experiment.

This configuration is particularly suited for the study of air-sensitive or unstable species, thanks to its sealed, anaerobic environment. However, some technical challenges must be carefully addressed, including gas evolution (*e.g.*, CO release) that may scatter IR radiation, electrical interference, product precipitation on electrode or window surfaces.

Proper electrode sealing and handling under inert conditions, along with careful cell assembly and cleaning, are essential to maintain reproducibility. When well optimized, the OTTLE cell remains a key tool in IR-SEC, offering precise, real-time insight into redox-induced vibrational changes in MMCCs. To summarize, specific advantages of IR SEC experiments on MMCCs are:

- with respect to CV, allows to verify the stability of the electrogenerated species on longer timescale, and, in the case of their subsequent reactions, identify the products from their vibrational spectra [102,103];
- recognize quasi-reversible electrochemical processes in cases where in the CV the back-scan peak is far from the forward peak [104];
- associate the electrochemical quasi-reversibility with structural changes, especially regarding the stereochemistry of the CO ligands, as pointed out by a change in shape and intensity of ν_{CO} bands by changing the charge of the cluster. In particular, the relative intensity of terminal (ν^t_{CO}) and bridging (ν^b_{CO}) bands varies with the redox state of the cluster, the ν^b_{CO} bands becoming more and more intense as the negative charge increases, according to the general observation that an increase of the negative charge of a cluster leads to an increased tendency for CO ligands to display a bridging coordination mode (Topic discussed in Section 4.1);
- processes masked by solvent discharge in CV, can become evident in IR SEC experiments [72,102];
- When the WE potential is swept between two values in the range of an electrodic process, the ν_{CO} bands of the initial cluster shift towards higher or lower wavenumbers and, for reversible one-electron processes, the sequences of IR spectra are featured by well-defined isosbestic points (Fig. 7a). If this doesn't happen, it may indicate the presence of more than two compounds (Fig. 7b) [103] and we can hypothesize that the additional species is a transient, intermediate oxidation state. This hypothesis was confirmed in several cases by spectral deconvolutions performed on some selected IR spectra collected during the redox process. For example, in the case of the oxidation of $[Rh_{21}Sb_2(CO)_{38}]^{5-}$, as shown in Fig. 7c-e, the peak fitting analysis of three consecutive IR spectra allowed us to determine the single absorbance contributions of each of the three redox states of the cluster to the overall spectra in different ratios, according to the potential scan direction.
- for impure samples, the low intensity peaks evident in CV profiles can be related to IR changes due to trace amounts of impurities, while the absorptions of the cluster under investigation remain unchanged. On the other hand, we were able to demonstrate the multivalence and electron sink behavior of $[Ni_{37-x}Pd_{7+x}(CO)_{48}]^{6-}$ (x = 0.69) [71] even in presence of $[Ni_6(CO)_{12}]^{2-}$. The latter does not interfere in the CV (its reversible reduction at −2.31 V and an irreversible oxidation at −0.31 V being, respectively, at lower and higher potential with respect to those of $[Ni_{37-x}Pd_{7+x}(CO)_{48}]^{6-}$). Instead, its presence is evident in the IR spectra, where the superimposition of ν^t_{CO} bands of the two clusters makes difficult to detect

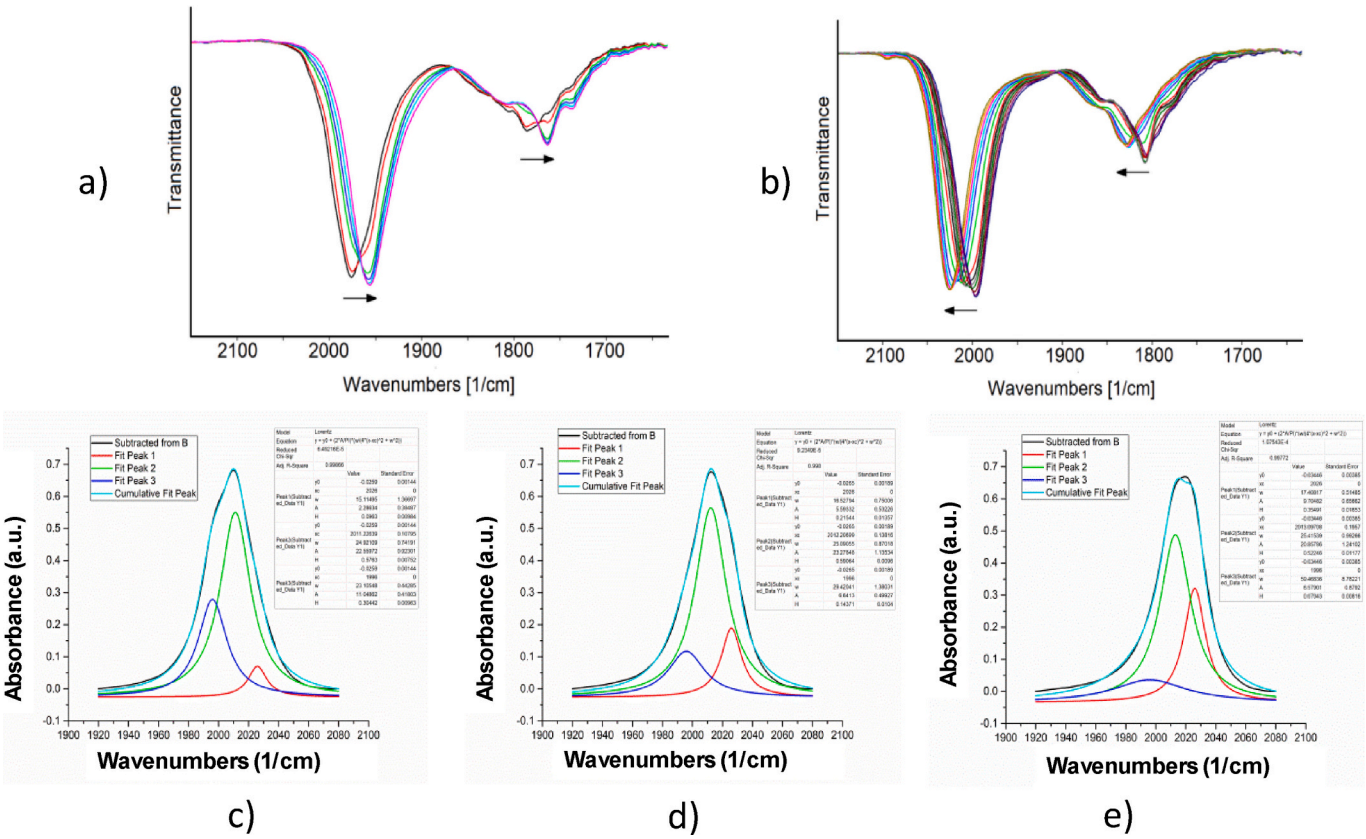

Fig. 7. IR spectral changes of a CH_3CN solution of $[Rh_{21}Sb_2(CO)_{38}]^{5-}$ recorded in an OTTLE cell during a) the progressive decrease of the potential from –0.96 to –1.32 V; b) the progressive increase of the potential from –0.6 to +0.6 V (*vs.* Ag pseudo-reference electrode; scan rate 1 mV s^{-1}, $[N^nBu_4][PF_6]$ (0.1 mol dm^{-3}) as supporting electrolyte. The absorptions of the solvent and the supporting electrolyte have been subtracted. c) — e) peak fitting analysis of three consecutive IR spectra acquired during the oxidation of $[Rh_{21}Sb_2(CO)_{38}]^{5-}$. Adapted with permission from Ref. [103]. Copyright 2020 American Chemical Society.

in this IR region the real shift induced by the redox processes of $[Ni_{37-x}Pd_{7+x}(CO)_{48}]^{6-}$ during the WE potential swept. The $[Ni_6(CO)_{12}]^{2-}$ interfering IR bands, which remained unchanged in the applied potential window, were eliminated calculating the differential absorbance spectra. In this way, one oxidation and three consecutive reduction steps of $[Ni_{37-x}Pd_{7+x}(CO)_{48}]^{6-}$, all completely chemically reversible, were ascertained (Fig. 8);

- recognize the products of fast chemical reactions that follow the electron transfer and uncover the mechanism of their formation. As an example, carbonylation/decarbonylation reactions of $[M_6C(CO)_{16}]^{2-}$/$[M_6C(CO)_{15}]^{4-}$ clusters (M = Ru, Fe) [105,106] follow electron transfers, due to the stability of the 86 CVE (cluster valence electrons) species, that make the processes chemically irreversible in the CV time scale under an Ar atmosphere. *In situ* IR SEC studies, supported by computational investigations, point out that the interconversion between $[Fe_6C(CO)_{16}]^{2-}$ and $[Fe_6C(CO)_{15}]^{4-}$ proceeds via two sequential one-electron steps followed by a chemical process, *i.e.* CO release/uptake. The intermediate, a –3 charge cluster that has been spectroscopically identified, can accumulate to varying extents during the IR-SEC experiments, depending on the experimental conditions such as scan rate, dissolved CO, and the presence of impurities. It is worth noting that DFT calculations support an EEC mechanism (Scheme 1) for both the oxidation and reduction processes, with the OTTLE cell playing a crucial role (due to the absence of free volume) in trapping the CO released upon quantitative reduction of $[Fe_6C(CO)_{16}]^{2-}$ and making it available for its near complete recovery in the back-oxidation step. On the other hand, under Ar atmosphere, the reduction of $[Ru_6C(CO)_{16}]^{2-}$ to $[Ru_6C(CO)_{15}]^{4-}$ in the OTTLE cell was accompanied by the formation of unidentified products, probably originating from side reactions with evolved CO. Moreover, the complete two-electrons oxidation of $[Ru_6C(CO)_{15}]^{4-}$, under Ar atmosphere, was achieved only using CH_3CN as solvent, affording $[Ru_6C(CO)_{15}(CH_3CN)]^{2-}$ as 86 CVE stable species.

UV-Vis-NIR spectroelectrochemistry (UV-Vis-NIR -SEC) represents a powerful *in situ* technique that couples the electronic control of redox processes with optical monitoring in the ultraviolet, visible, and near-infrared spectral regions [61]. As detailed in recent comprehensive reviews [94,96], this hybrid approach allows real-time tracking of electronic transitions and structural changes associated with redox transformations, making it especially valuable for investigating transient species, charge delocalization phenomena, and the redox behavior of conjugated or metal-containing systems. Typically performed in optically transparent thin-layer electrode (OTTLE) cells similar to the one already described in the paragraph above. In this case, the technique requires careful selection of window materials (*e.g.,* quartz or CaF_2) and transparent WEs (e.g., ITO, Pt minigrids) to ensure compatibility with the spectral range of interest. Moreover, the geometry of light propagation (normal or parallel to the electrode surface) significantly affects spectral resolution and path length, influencing both sensitivity and time response [61,107].

UV-Vis-NIR spectra of metal clusters can be relatively simple for low-nuclearity compounds with well-spaced electronic energy levels, the onset wavelength of the lower energy band being used for calculating the HOMO-LUMO gap. As cluster nuclearity increases, the overall density of states of electronic energy levels increases and electronic spectra of their very dark solutions are characterized by poorly resolved bands; rather, a broad and continuous absorption spans the visible region into the NIR. Correspondingly, the HOMO-LUMO gap for large MMCCs drops

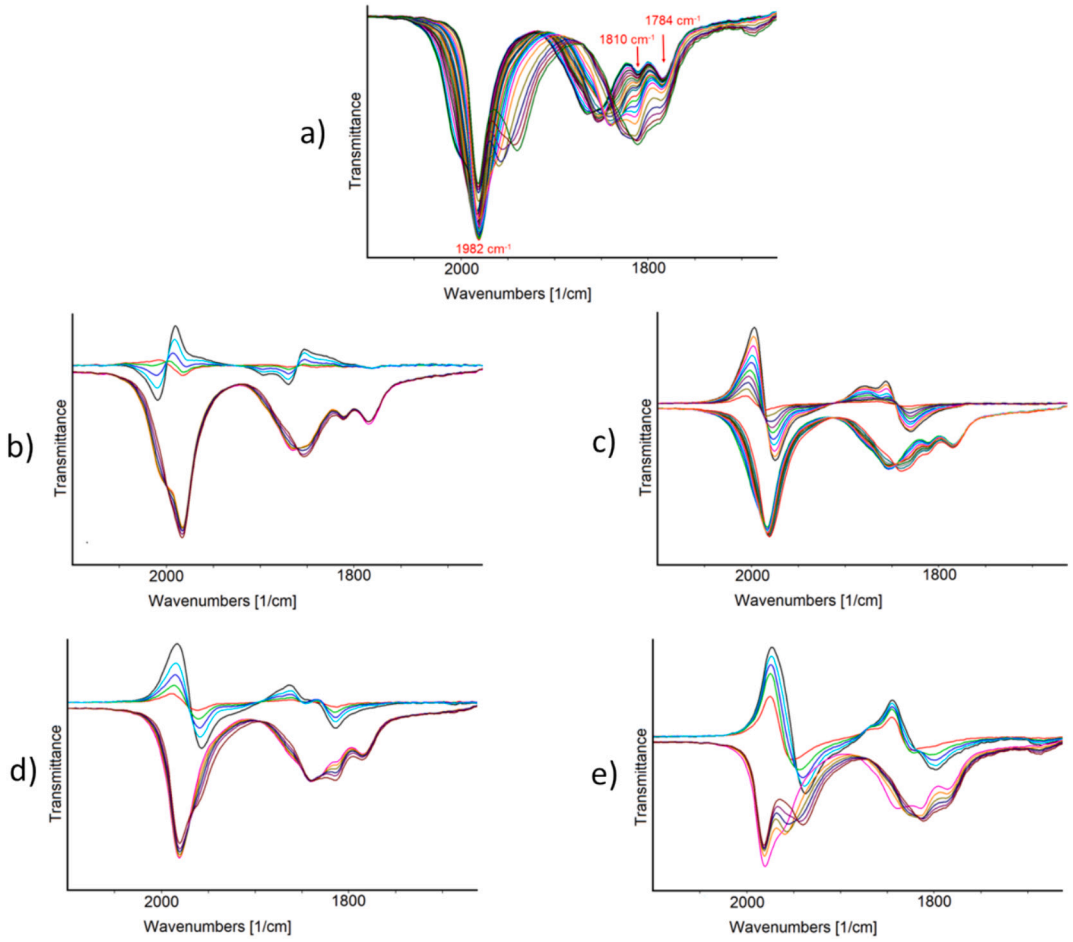

Fig. 8. IR spectral changes of a CH_3CN solution $[Ni_{37-x}Pd_{7+x}(CO)_{48}]^{6-}$ (x = 0.69) recorded in an OTTLE cell during the progressive swept of the potential a) between –0.3 to –1.8 V (*vs*. Ag pseudo-reference electrode; scan rate 1 mV s^{-1}. $[N^nBu_4][PF_6]$ (0.1 mol dm^{-3}) as the supporting electrolyte). The absorptions of the solvent and the supporting electrolyte have been subtracted. In red the ν_{CO} of $[Ni_6(CO)_{12}]^{2-}$; b) from −0.6 to −0.3 V (a reference spectrum, collected before the application of an oxidant potential, is used to calculate the differential absorbance spectra reported in the top of the figure); c) from −0.6 to −1.2 V (a reference spectrum, collected before the application of a reducing potential, is used to calculate the differential absorbance spectra reported in the top of the figure); d) from −1.2 to −1.5 V (to calculate the differential absorbance spectra reported in the top of the figure, as reference spectrum, was used the first one of the series, collected at the potential of −1.2 V); e) from −1.5 to −1.8 V (to calculate the differential absorbance spectra reported in the top of the figure, as reference spectrum, was used the first one of the series, collected at the potential of −1.5 V). Adapted with permission from Ref. [71]. Copyright 2021 American Chemical Society.

$$\underset{\text{86 CVE}}{[Fe_6C(CO)_{15}]^{4-}} \xrightarrow[\text{E}]{-e^-} \underset{\text{85 CVE}}{[Fe_6C(CO)_{15}]^{3-}} \xrightarrow[\text{E}]{-e^-} \underset{\text{84 CVE}}{[Fe_6C(CO)_{15}]^{2-}} \xrightarrow[\text{C}]{+CO} \underset{\text{86 CVE}}{[Fe_6C(CO)_{16}]^{2-}}$$

Scheme 1. Proposed mechanism for the electrochemical oxidation of $[Fe_6C(CO)_{15}]^{4-}$.

to values under 1 eV and high spin, paramagnetic ground states become possible [108]. Here's why *in situ* UV-Vis-NIR SEC studies of high nuclearity MMCCs are relatively rare [98,109].

From a computational point of view, the accurate description of electronically excited states of metal clusters is challenging [110]. Time-dependent density functional theory (TD-DFT) is the sole first principles approach applicable for large systems thanks to its acceptable computational cost. When the closed-shell ground state can be described by a single determinant, TD-DFT usually provides reliable vertical excitation energies for the singlet and triplet excited states, with errors being typically in the 0.2–0.4 eV interval. Anyway, TD-DFT is unable to handle all kinds of excited states. For instance, such an approach fails when the ground state is degenerate or nearly degenerate. TD-DFT is also inappropriate to investigate open-shell systems with unpaired electrons, since spin-contaminated excited states are produced and errors can be as large as 1–3 eV even for relatively simple compounds.

3. Investigation of the electronic properties of MMCCs by electrochemistry

Electrochemical measurements give important insights into the electronic properties of MMCCs. A first information on the frontier molecular orbitals is obtained just based on the absence or the presence (and the number) of reversible electrochemical redox processes. The complete absence of any reversible redox process, in the accessible electrochemical window, is usually indicative of a closed-shell MMCC with a large HOMO-LUMO gap. The added electron for the reduction process would enter a high energy antibonding orbital, whereas the electron should be removed upon oxidation from a low energy bonding orbital. Both cases would result in destabilization of the MMCC. Many low nuclearity MMCCs are non-redox active and display an almost perfect correspondence between number of cluster valence electrons (CVE) and geometry of the metal frame [42]. For this purpose, different

rules for electron bookkeeping in MMCCs have been developed, including the effective atomic number (EAN) rule, cluster-borane analogy and Wade's rules, the polyhedral skeletal electron pair theory (PSEPT), and topological electron counting (TEC) [111–114]. Recently, also the superatom model has been successfully applied to some MMCCs [115–118].

As the number and size of structurally characterized MMCCs increased, exceptions to the above-mentioned electron counting rules appeared, and significant examples of redox active MMCCs were disclosed by electrochemical and SEC measurements. Interestingly, deviations from predicted electron count and redox aptitude were both encountered more frequently as the nuclearity of MMCCs increased.

A MMCC can be described as redox active, if it displays at least one redox process with features of reversibility by electrochemistry. In some cases, also quasi-reversible redox processes are considered for this purpose, if their deviation from reversibility is not too large. Often oxidized or reduced MMCCs are just observed in the timescale of electrochemical or SEC measurements. Sometimes, they are sufficiently stable to be observed also during chemical oxidation and reduction reactions, or even to be isolated after work-up of the reaction mixture. In some cases, a given cluster has been isolated and structurally characterized by SC-XRD in different oxidation states.

Redox active MMCCs may be classified based on the number of their reversible redox processes. A rough, but effective, classification may be done based on the fact that a redox active MMCC displays (a) a single reversible redox process (Table 2), (b) two reversible redox processes (Table 3), or (c) three or more reversible redox processes (Table 4). The limit of three redox processes has been selected, because it indicates that more than one molecular orbital is involved in the electrochemical processes.

If a single reversible redox event is present (a), and this is an oxidation, it means that one electron may be removed from the HOMO without significantly altering the MMCC stability. This is indicative of a weakly bonding, weakly anti-bonding or non-bonding HOMO. Similar considerations may be applied to the LUMO, if the single reversible redox event is a reduction.

In case (b), the two reversible redox processes may be both oxidations or reductions, or one is an oxidation and the other a reduction. If the two events are of the same type, two electrons are added or removed in sequence to/from the same orbital (or from degenerate orbitals). In contrast, if one reversible oxidation and one reduction are present, it means that it is possible both to remove one electron from the HOMO and to add one electron to the LUMO. Moreover, the difference ($\Delta E^{\circ\prime}$) between the oxidation and reduction potentials is related to the energy HOMO-LUMO gap. It is worth noting that the outcomes of electrochemical measurements cannot be directly compared with other techniques, as summarized by Holze [167]. For instance, the influence of the solvation shell is not present in photoelectron spectroscopy measurements carried out on solid samples. Further problems arise when electrochemical and optical HOMO-LUMO gaps are compared, since electrochemical transformations of a neutral compound result in the formation of charged species, while absorption of electromagnetic radiation produces an excited but still neutral compound.

A MMCC showing three or more reversible redox processes (c) is said to behave as an electron sponge (or electron reservoir, or electron sink), and is often referred as a multivalent MMCC, in the sense that it can exist in four or more different oxidation states. The redox processes of multivalent MMCCs involve two or more molecular orbitals and, thus, their study lends more extensive information of the frontier orbitals of the cluster, compared to cases (a) and (b). Moreover, the spacing between consecutive redox processes ($\Delta E^{\circ\prime}$) may give additional information on the relative energies of frontier molecular orbitals, also in comparison with the pairing energy of electrons on the same orbital.

3.1. *Ad hoc* conditions for redox activity of MMCCs

Redox properties of MMCCs may originate from *ad hoc* conditions or incipient metallization of their metal core. *Ad hoc* conditions are usually found in lower nuclearity redox active MMCCs, whereas incipient metallization occurs as the nuclearity of the cluster increases. Some overlap may be present at mid nuclearities.

Ad hoc conditions consist of a synergy between electronic, steric and bonding features, which lead to the presence of one or more weakly bonding/antibonding or non-bonding orbitals in a well-defined energy gap (a potential HOMO–LUMO gap). In some cases, fragmentation or condensation upon redox reactions is prevented by the efficient shielding of the CO shell and the strength of M-M bonds, as for instance in $[Fe_4Au(CO)_{16}]^-$ [129], $[Fe_3Pt_3(CO)_{15}]^{2-}$ [127,128], and $[HFe_6Pd_6(CO)_{24}]^{3-}$ [143]. In particular, $[Fe_3Pt_3(CO)_{15}]^{2-}$ displays two reversible one-electron oxidations, leading to paramagnetic $[Fe_3Pt_3(CO)_{15}]^-$ and neutral $[Fe_3Pt_3(CO)_{15}]$ (Fig. 9). All the three species $[Fe_3Pt_3(CO)_{15}]^{n-}$ (n = 0-2) have been isolated and characterized by SC-XRD. The HOMO of the dianion is weakly antibonding and, thus, the Pt-Pt bond distances progressively shorten by ca. 0.08 Å upon each oxidation step. Dimerization of the mono-anion $[Fe_3Pt_3(CO)_{15}]^-$ is hampered by the apical CO ligands bonded to the three μ-$Fe(CO)_4$ units. Indeed, in the absence of such steric protection, the planar Chini cluster $[Pt_3(CO)_6]^{2-}$ dimerizes upon oxidation to $[Pt_6(CO)_{12}]^{2-}$ [168]. This point has been further corroborated by Figueroa *et al.*, who isolated and structurally characterized the monomeric Chini-type clusters $[Pt_3(\mu\text{-}CO)_3(CNAr^{Dipp2})_3]^{n-}$ (n = 0–2; Ar^{Dipp2} = 2,6-(2,6-(*i*-Pr)$_2C_6H_3$)$_2C_6H_3$) [169]. The dianion may be viewed as the heteroleptic analogue of $[Pt_3(CO)_6]^{2-}$, whereas neutral $[Pt_3(\mu\text{-}CO)_3(CNAr^{Dipp2})_3]$ is closely related to the well-known $[Pt_3(\mu\text{-}CO)_3(PR_3)_3]$ (R = alky or aryl). Both $[Pt_3(CO)_6]^{2-}$ and $[Pt_3(\mu\text{-}CO)_3(PPh_3)_3]$ display only irreversible electrochemical processes, whereas $[Pt_3(\mu\text{-}CO)_3(CNAr^{Dipp2})_3]$ shows two reversible one-electron reductions at –1.39 and –2.04 V (*vs* SCE) (Fig. 10). The observed redox behavior of $[Pt_3(\mu\text{-}CO)_3(CNAr^{Dipp2})_3]^{n-}$ (n = 0–2) results from a synergy between the steric and electronic properties of the $CNAr^{Dipp2}$ isocyanide ligand. Its bulkiness prevents dimerization of the $[Pt_3(\mu\text{-}CO)_3(CNAr^{Dipp2})_3]^-$ monoanion and lends support to the fact that $[Pt_3(CO)_6]^-$ radicals are involved in the oxidation of

Table 2
Selected examples of MMCCs with one reversible redox change ($E^{\circ\prime}$ in V, relative to SCE).

Compound	Solvent	+1/0	0/–1	–1/–2	–2/–3	Ref
$[Fe_3(CO)_{11}]^{2-}$	THF			–0.76		[118]
$[Fe_3S(CO)_9]^{2-}$	DCE			–0.40		[43]
$[Fe_3S_2(CO)_9]$	PhCN		–0.48			[43]
$[Fe_5N(CO)_{14}]^-$	CH_3CN			–0.90		[119]
$[FeCo_2S(CO)_9]$	DCE	+0.44				[120]
$[FeIr_5(CO)_{15}]^{3-}$	CH_3CN				–0.57	[121]
$[H_2Os_3(CO)_{10}]$	acetone		–0.66			[122]
$[Os_6(CO)_{19}(CH_3CN)_2]$	CH_3CN		–0.87			[123]
$[Co_4Sb_2(CO)_{11}]^-$	CH_2Cl_2			–0.58		[124]
$[Co_4Bi_2(CO)_{11}]^-$	CH_2Cl_2			–0.65		[124]
$[Co_9Si(CO)_{21}]^{2-}$	CH_2Cl_2				–0.47	[48]
$[HCo_{10}P_2(CO)_{23}]^{2-}$	CH_3CN				–0.73	[125]

Table 3
Selected examples of MMCCs with two reversible redox changes ($E^{\circ\prime}$ in V, relative to SCE).

Compound	Solvent	+1/0	0/-1	–1/–2	–2/–3	–3/–4	–4/–5	–5/–6	Ref
$[Fe_4N(CO)_{12}]^-$	CH_3CN			–1.23	–1.58				[49]
$[Fe_5S_2(CO)_{14}]^{2-}$	CH_2Cl_2		+0.26	–0.18					[126]
$[Fe_3Pt_3(CO)_{15}]^{2-}$	CH_3CN		+0.19	–0.40					[127,128]
$[Fe_4Au(CO)_{16}]^-$	CH_3CN			–0.73	–0.93				[129]
$[Os_6(CO)_{20}(CH_3CN)]$	CH_3CN		–0.65	–0.89					[123]
$[H_4Os_{10}(CO)_{24}]^{2-}$	CH_2Cl_2		+0.57	+0.35					[130]
$[Os_{10}C(CO)_{24}]^{2-}$	CH_2Cl_2			+0.74	–1.39				[131]
$[Os_4Pt_2(CO)_{17}]$	CH_2Cl_2		–0.57	–0.84					[132]
$[Os_4Pt_2(CO)_{15}(COD)]$	CH_2Cl_2		–0.67	–0.93					[132]
$[Co_{11}C_2(CO)_{23}]^{2-}$	THF			+0.01	–0.63				[133]
$[Co_{13}N_2(CO)_{24}]^{3-}$	CH_3CN					–0.74	–1.29		[134]
$[Co_6AuC(CO)_{16}]^-$	CH_2Cl_2 *			–0.77	–1.31				[82]
$[H_2Co_{15}Pd_9C_3(CO)_{38}]^-$	CH_2Cl_2	+0.60	+0.10						[135]
$[Co_{15}Pd_9C_3(CO)_{38}]^{3-}$	CH_2Cl_2			+0.35	+0.00				[135]
$[Ir_6(CO)_{15}]^{2-}$	acetone		+0.50	+0.12					[136]
$[Ir_{14}(CO)_{27}]^-$	CH_2Cl_2		+0.35	–0.04					[137]
$[Ni_{22}(C_2)_4(CO)_{28}(CdBr)_2]^{4-}$	DMF						–0.71	–0.85	[79]
$[Ni_{11}Sb_2(CO)_{18}]^{3-}$	CH_3CN				–0.65	–1.42			[138]
$[Ni_{11}Bi_2(CO)_{18}]^{3-}$	CH_3CN				–0.67	–1.42			[139]
$[Ni_{13}Sb_2(CO)_{24}]^{3-}$	CH_3CN				–0.56	–1.28			[140]
$[Ag_{13}Fe_8(CO)_{32}]^{3-}$	CH_3CN					–0.37	–0.65		[141]

* Three redox processes have been observed in THF (see Table 4).

$[Pt_3(CO)_6]^{2-}$ to $[Pt_6(CO)_{12}]^{2-}$. Moreover, the larger π-acidic character of isocyanides compared to phosphines stabilizes the $[Pt_3(\mu\text{-}CO)_3(CNAr^{Dipp2})_3]^{2-}$ dianion. Indeed, $[Pt_3(\mu\text{-}CO)_3(PPh_3)_3]^{2-}$ has been isolated in the solid state only very recently, from the reaction of $K_6Rb_6Ge_{17}$, $[Pt(CO)_2(PPh_3)_2]$ and [2.2.2]-crypt in liquid ammonia after three months' storage at 233 K [170].

In other cases, stabilization of the species electro-generated by redox processes is guaranteed by the presence of peripheral or interstitial main group elements that reinforce the metal core of MMCCs. Indeed, several MMCCs containing C, Si, N, P, As, Sb, Bi, S, and Te atoms are present in Tables 2–4. Stabilization may be also obtained thanks to robust M-M bonds, as for second and third row transition metals, or synergetic M-M' bonds in heterometallic clusters. For instance, $[Ir_6(CO)_{15}]^{2-}$ displays one reversible and one quasi-reversible oxidation [136], and the paramagnetic mono-anion $[Ir_6(CO)_{15}]^-$ has been spectroscopically characterized. In contrast, the lighter congeners $[M_6(CO)_{15}]^{2-}$ (M = Co, Rh) show only irreversible electrochemical processes. Also $[Ir_{14}(CO)_{27}]^-$ [137] and $[H_4Os_{10}(CO)_{24}]^{2-}$ [130] shows two reversible redox processes, whereas their structurally related $[H_{4-n}Ni_{12}(CO)_{21}]^{n-}$ (n = 2–4) and $[H_{4-n}Ni_9Pt_3(CO)_{21}]^{n-}$ (n = 2–4) are non-redox active.

Even if rarer, in some cases the higher strength of M-M bonds may be detrimental for the reversibility of electrochemical processes. Indeed, $[Fe_3(CO)_{11}]^{2-}$ may be reversibly oxidized to $[Fe_3(CO)_{11}]^-$ [118], whereas the heavier congeners $[M_3(CO)_{11}]^{2-}$ (M = Ru, Os) undergo only irreversible one-electron oxidations. It is likely that, because of the higher Ru-Ru and Os-Os bond energies compared to Fe-Fe, dimerization occurs upon oxidation of $[M_3(CO)_{11}]^{2-}$ (M = Ru, Os).

An *ad hoc* condition is also at the heart of the redox behavior of the $[Ag_{13}Fe_8(CO)_{32}]^{n-}$ (n = 3–5) species [171]. All three congeners have been chemically isolated and structurally characterized by SC-XRD, showing very similar structures. The eight μ_3-$Fe(CO)_4$ groups provide steric protection to the Ag_{13} core. The LUMO of $[Ag_{13}Fe_8(CO)_{32}]^{3-}$ lies *ca.* 0.48 eV above its HOMO and 1.59 eV below the LUMO+1. Since the LUMO is essentially non-bonding and delocalized over the whole Ag_{13} core, it can progressively accept two additional electrons without altering significantly the cluster stability. The metal core of the cluster consists of an Ag-centered Ag_{12} cube-octahedron, which is a piece of a *hcp* metal arrangement. The interstitial Ag 5s orbital contributes *ca.* 25% to the SOMO of paramagnetic $[Ag_{13}Fe_8(CO)_{32}]^{4-}$, as indicated also by the strong coupling observed in its EPR spectrum (Fig. 11).

The presence of fully interstitial late transition metal atoms (Ag in the case of $[Ag_{13}Fe_8(CO)_{32}]^{n-}$; Ni or Co in the following examples) seems to be a feature common also to other redox active MMCCs, such as, $[Ni_{11}Sb_2(CO)_{18}]^{3-}$ [138], $[Ni_{11}Bi_2(CO)_{18}]^{3-}$ [139], $[Ni_{13}Sb_2(CO)_{24}]^{3-}$ [140], $[Co_{11}Te_7(CO)_{10}]^-$, and $[Co_{11}Te_7(CO)_5(PMe_2Ph)_5]$ [150] (Fig. 12). It seems that the atomic d orbitals of the interstitial late transition metal atoms have suitable symmetry and energy to weakly interact with the metal cage, resulting in a set of a few weakly bonding and anti-bonding molecular orbitals. At the same time, the presence of fully interstitial metal atoms with high coordination numbers suggests some structural and topological resemblances to bulk metals. Indeed, it may be viewed as a hint of the incipient metallization of larger MMCCs.

3.2. Metallization of the metal core of MMCCs

As a matter of fact, as MMCC nuclearity increases, the CO/M ratio decreases and the M-M bonds become more relevant and, eventually, predominant over M-CO interactions, approaching the coordination of bulk metals. Therefore, the number of interstitial and highly coordinated metal atoms increases with cluster nuclearity. It is not surprising that multivalence and electron sponge behavior are often found in larger MMCCs. Indeed, as the number of metallic M–M interactions increase, metallization of the metal core of the cluster should occur, independently of the actual structure adopted. This corresponds to a decrease of the HOMO-LUMO gap and, eventually, to the appearance of a continuum of energy levels (Fig. 13) [98,108]. Metallization of the metal core of MMCCs is a gradual process, which should involve an insulator-to-metal-transition, passing through a semiconductor regime.

Theoretical calculations indicate that ligand coordination to the surface of bare metal clusters partially quenches the metallization process [172]. Moreover, in the attempt to relate the metallization process with cluster size, the real nuclearity of the metal core must be considered, and not the nominal one, which is sometimes affected by staple motives and conjuncto structures.

Important information on the metallization process may be obtained from electrochemical data. The number of reversible redox processes is related to the number of available orbitals in the frontier region, which can be populated or depleted without significantly altering the MMCC stability. Most entries in Table 4 show three or four reversible redox processes, but there are also some larger MMCCs, with nuclearities in the range 19-44, that display five, six or even seven reversible redox processes (Fig. 14).

Further information may be obtained by analyzing the differences of

Table 4
Selected examples of MMCCs with three or more reversible redox changes (electron sponge behavior) ($E^{\circ\prime}$ in V, relative to SCE).

Compound	Solvent	+1/0	0/–1	–1/–2	–2/–3	–3/–4	–4/–5	–5/–6	–6/–7	–7/–8	–8/–9	–9/–10	–10/–11	Ref
$[Fe_6Ni_6N_2(CO)_{24}]^{2-}$	CH_3CN			+0.17	–0.40	–0.90								[142]
$[HFe_6Pd_6(CO)_{24}]^{3-}$	acetone				+0.39	–0.64	–1.18							[143]
$[Os_{20}(CO)_{44}]^{2-}$	THF		+0.74	+0.32	–0.15									[144]
$[Os_9Rh_3(CO)_{28}]^{-}$	CH_2Cl_2			+0.77	+0.39	–0.01	–0.31							[145]
$[Os_{18}Pd_3C_2(CO)_{42}]^{2-}$	acetone				+0.83	+0.45	–0.11	–0.54	–1.05					[146]
$[Co_8C(CO)_{18}]^{2-}$	DCE			–0.01	–0.81	–1.35								[147]
$[Co_{13}C_2(CO)_{24}]^{4-}$	CH_3CN					–0.54	–1.06	–1.68						[134]
$[Co_{10}N_2(CO)_{19}]^{4-}$	CH_3CN			–0.14	–0.52	–0.85	–1.72	–2.16						[148]
$[Co_{11}N_2(CO)_{21}]^{3-}$	CH_3CN			–0.23[a]	–0.23[a]	–1.05	–1.47	–2.07						[148]
$[Co_{10}P(CO)_{22}]^{3-}$	CH_3CN				–0.10	–1.32	–1.47							[149]
$[Co_{11}Te_7(CO)_{10}]^{-}$	THF		+0.33	–0.32	–1.04									[150]
$[Co_{11}Te_7(CO)_9(PMe_2Ph)]$	THF		+0.09	–0.53	–1.16									[150]
$[Co_{11}Te_7(CO)_8(PMe_2Ph)_2]$	THF		–0.12	–0.76	–1.37									[150]
$[Co_{11}Te_7(CO)_7(PMe_2Ph)_3]$	THF		–0.36	–0.98	–1.54									[150]
$[Co_{11}Te_7(CO)_6(PMe_2Ph)_4]$	THF	+0.10	–0.54	–1.16	–1.71	–2.05								[150]
$[Co_{11}Te_7(CO)_5(PMe_2Ph)_5]$	THF	–0.08	–0.74	–1.36	–1.90									[150]
$[Co_{38}As_{12}(CO)_{50}]^{4-}$	CH_3CN			+0.14	–0.14	–0.42	–0.70	–0.98	–1.26	–1.54				[151]
$[Co_5MoN(CO)_{14}]^{2-}$	CH_3CN				–1.28	–1.70	–2.31							[152]
$[HCo_{15}Pd_9C_3(CO)_{38}]^{2-}$	CH_2Cl_2	+0.90	+0.40	+0.07										[135]
$[Co_8Pt_4C_2(CO)_{24}]^{2-}$	THF			+0.18	–0.91	–1.38								[153]
$[Co_6AuC(CO)_{16}]^{-}$	THF[b]			–0.69	–1.38	–2.07								[82]
$[Co_{10}AuC_2(CO)_{24}]^{-}$	CH_2Cl_2		+0.71	–0.63	–0.91	–1.42	–1.72							[82]
$[HRh_{14}(CO)_{25}]^{3-}$	CH_3CN			–0.02	–0.25	–1.25	–1.58							[78]
$[H_3Rh_{22}(CO)_{35}]^{5-}$	DMF					+0.18	–0.24	–0.65	–1.10	–1.41	–1.59			[154]
$[H_3Rh_{22}(CO)_{35}]^{5-}$	CH_3CN						–0.24	–0.60	–1.05	–1.38	–1.60			[154]
$[H_4Rh_{22}(CO)_{35}]^{4-}$	CH_3CN					+0.01	–0.73	–0.82	–1.20					[154]
$[Rh_{16}Au_6(CO)_{36}]^{6-}$	CH_3CN				+0.05	–0.17	–0.44	–0.66	–1.24	–1.48	–1.75	–1.91		[155]
$[Rh_{12}In(CO)_{28}]^{3-}$	CH_3CN			–0.14	–0.34	–1.82[a]	–1.82[a]							[104]
$[Rh_{21}Sb_2(CO)_{38}]^{5-}$	CH_3CN					–0.26[a]	–0.26[a]	–0.90	–1.16	–1.41[a]	–1.41[a]	–1.85		[103]
$[Ni_{12}C(CO)_{18}]^{4-}$	CH_3CN				–0.50	–0.76	–1.15							[156]
$[Ni_{16}(C_2)_2(CO)_{23}]^{4-}$	DMF					–0.60	–1.63	–1.80						[157]
$[Ni_{25}(C_2)_4(CO)_{32}]^{4-}$	DMF					–0.34	–1.33	–1.64	–1.95					[157]
$[Ni_{25}(C_2)_4(CO)_{32}]^{4-}$	CH_3CN					–0.65	–1.25	–1.50	–1.83	–2.05				[157]
$[HNi_{25}(C_2)_4(CO)_{32}]^{3-}$	CH_3CN					–0.97	–1.13	–1.45						[157]
$[Ni_{22}(C_2)_4(CO)_{28}Cl]^{3-}$	DMF					–1.37	–1.50	–1.68						[157]
$[Ni_{32}C_6(CO)_{36}]^{6-}$	CH_3CN							–0.45	–0.77	–1.06	–1.33	–1.60		[158]
$[HNi_{38}C_6(CO)_{42}]^{5-}$	CH_3CN							–0.60	–1.11	–1.42	–1.77			[158]
$[Ni_{38}C_6(CO)_{42}]^{6-}$	CH_3CN							–0.49	–0.98	–1.33	–1.73			[158]
$[Ni_{38}C_6(CO)_{42}]^{6-}$	DMF						–0.24	–0.60	–1.10	–1.47				[158]
$[HNi_{31}P_4(CO)_{39}]^{5-}$	CH_3CN					–0.53	–0.78	–1.19	–1.50	–2.10				[102]
$[H_2Ni_{31}P_4(CO)_{39}]^{4-}$	CH_3CN						–0.59	–0.82	–1.74					[102]
$[Ni_5Rh_9(CO)_{25}]^{3-}$	CH_3CN			–0.18	–0.35	–1.25								[159]
$[Ni_{29-x}Pd_{6+x}(CO)_{42}]^{6-}$ (x = 0.09)	CH_3CN							–0.68	–1.10	–1.36	–1.62			[80]
$[Ni_{22-x}Pd_{20+x}(CO)_{48}]^{6-}$ (x = 0.62)	CH_3CN													[80]
$[Ni_{36-x}Pd_{5+x}(CO)_{46}]^{6-}$ (x = 0.41)	CH_3CN							–0.50	–0.80	–1.09	–1.58	–1.83		[71]
$[Ni_{37-x}Pd_{7+x}(CO)_{48}]^{6-}$ (x = 0.69)	CH_3CN							–0.61	–0.79	–1.12	–1.30	–1.65	–1.91	[71]
$[HNi_{37-x}Pd_{7+x}(CO)_{48}]^{5-}$ (x = 0.53)	CH_3CN						–0.23	–0.56	–0.93	–1.26	–1.60	–1.95		[71]
$[HNi_{24}Pt_{14}(CO)_{44}]^{5-}$	CH_3CN						–0.30	–0.63	–1.11	–1.49				[42]
$[HNi_{36}Pt_4(CO)_{45}]^{5-}$	CH_3CN						–0.70	–1.08	–1.38	–1.76				[160]
$[Ni_{36}Pt_4(CO)_{45}]^{6-}$	CH_3CN							–0.80	–1.15	–1.46	–1.82			[160]
$[HNi_{35}Pt_9(CO)_{48}]^{5-}$	DMF					–0.30	–0.73	–1.17	–1.38					[161]
$[Ni_{35}Pt_9(CO)_{48}]^{6-}$	DMF						–0.23	–0.63	–1.03	–1.43				[161]
$[HNi_{38}Pt_6(CO)_{48}]^{5-}$	DMF					–0.25	–0.62	–0.96	–1.28	–1.62				[162]
$[Ni_{38}Pt_6(CO)_{48}]^{6-}$	DMF							–0.62	–0.97	–1.29	–1.54	–1.75		[162]
$[H_2Ni_{29}C_4(CO)_{34}\{Cu(CH_3CN)\}_2]^{2-}$	Acetone				–0.32	–0.68	–1.06	–1.34						[163]
$[H_2Ni_{29}C_4(CO)_{32}(CH_3CN)_2\{Cu(CH_3CN)\}_2]^{2-}$	CH_3CN				–0.32	–0.60	–1.03	–1.67						[163]
$[H_2Ni_{30}C_4(CO)_{34}\{Cu(CH_3CN)\}_2]^{4-}$	Acetone					–0.29	–0.55	–0.79	–0.98					[163]
$[HNi_{30}C_4(CO)_{34}\{Cu(CH_3CN)\}_2]^{5-}$	CH_3CN							–0.62	–1.04	–1.40				[163]
$[Ni_{30}C_4(CO)_{34}\{Cu(CH_3CN)\}_2]^{6-}$	DMF							–0.45	–0.83	–1.03	–1.44			[163]
$[Ni_{30}C_4(CO)_{34}(CdCl)_2]^{6-}$	DMF							–0.49	–0.88	–1.28				[79]
$[Ni_{36}C_8(CO)_{36}(Cd_2Cl_3)]^{5-}$	DMF						–0.61	–0.97	–1.15					[79]
$[HNi_{42+x}C_8(CO)_{44+x}(CdCl)]^{6-}$	DMF							–0.45	–0.70	–0.91	–1.18			[79]
$[Pt_{19}(CO)_{22}]^{4-}$	CH_3CN		+0.48	+0.40	+0.07	–0.24	–1.14	–1.31	–2.16	–2.33				[164]
$[Pt_{19}(CO)_{22}]^{4-}$	CH_3CN				+0.01	–0.23	–1.15	–1.30	–2.02	–2.16				[165]

(continued on next page)

Table 4 (*continued*)

Compound	Solvent	+1/0	0/–1	–1/–2	–2/–3	–3/–4	–4/–5	–5/–6	–6/–7	–7/–8	–8/–9	–9/–10	–10/–11	Ref
$[Pt_{19-x}Ni_x(CO)_{22}]^{4-}$ (x = 3.11)	CH_3CN						–1.17	–1.37	–2.08[c]	–2.08[c]	–2.08[c]			[165]
$[Pt_{24}(CO)_{30}]^{2-}$	CH_2Cl_2		+0.60	+0.30	–0.51	–0.76	–1.26	–1.52						[164]
$[Pt_{26}(CO)_{32}]^{2-}$	CH_3CN				–0.20	–0.20	–0.80	–0.80	–1.30	–1.30	–1.90	–1.90		[166]
$[Pt_{27}(CO)_{31}]^{4-}$					–0.06	–0.66	–0.96	–1.58	–1.70					[83]
$[Pt_{33}(CO)_{38}]^{2-}$	CH_3CN		+0.24	–0.04	–0.48	–0.75	–1.33[a]	–1.33[a]	–1.68					[72]
$[Pt_{38}(CO)_{44}]^{2-}$	CH_2Cl_2		+0.53	+0.34	–0.36	–0.58	–0.97	–1.24						[164]
$[Pt_{40}(CO)_{40}]^{6-}$	CH_3CN				+0.50	+0.21	–0.15	–0.40	–0.87	–1.11	–1.44	–1.68		[72]

[a] Two-electrons process.
[b] Two redox processes have been observed in CH_2Cl_2 (see Table 3).
[c] Three-electrons process.

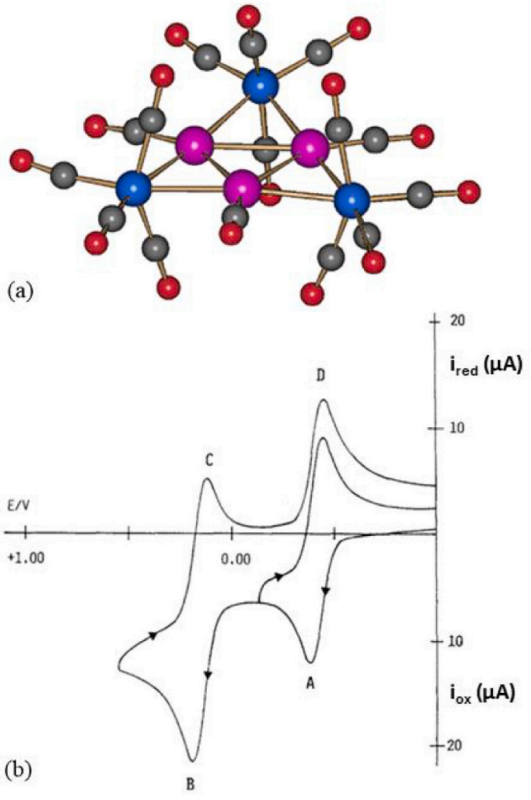

Complex	Pt-Pt	Pt-Fe
$[Fe_3Pt_3(CO)_{15}]^{2-}$	2.75	2.60
$[Fe_3Pt_3(CO)_{15}]^{-}$	2.66	2.59
$[Fe_3Pt_3(CO)_{15}]$	2.59	2.58

Fig. 9. (a) Molecular structure (purple, Pt; blue, Fe; red, O; grey, C) and (b) CV of $[Fe_3Pt_3(CO)_{15}]^{2-}$ recorded at a Pt electrode on CH_2Cl_2 solution with $[N^nBu_4][ClO_4]$ at 0.2 V s^{-1}. The table reports the average bond lengths (Å) of $[Fe_3Pt_3(CO)_{15}]^{n-}$ (n = 0–2). Adapted from Ref. [127] with permission from Springer.

the formal electrode potentials ($\Delta E^{\circ\prime}$) for consecutive redox processes of the same MMCC. Their trend can be visualized using a Z-plot, that is, a plot of the formal electrode potential ($E^{\circ\prime}$) *vs.* the charge (Z) of the most oxidized species of the Z–/(Z+1)– redox couples of a multivalent MMCC. In most cases, the Z-plots adopt a staircase-like (Fig. 15) or a linear trend (Fig. 16), even though sometimes an intermediate behavior is observed (Fig. 17). Representative CV profiles are provided in Fig. 18.

Staircase-like Z-plots display an alternation of smaller and larger $\Delta E^{\circ\prime}$ (Fig. 15). It might be assumed that in such MMCCs, electrons enter in pairs by first semi-occupying and then filling one-by-one the frontier orbitals, due to the fact that the energy separation between these orbitals is greater than pairing energy. Staircase-like Z-plots are usually found in mid-nuclearity MMCCs such as $[Co_{10}AuC_2(CO)_{24}]^-$ [82], $[HRh_{14}(CO)_{25}]^{3-}$ [78], $[H_4Rh_{22}(CO)_{35}]^{4-}$ [154], $[Pt_{19}(CO)_{22}]^{4-}$ [164], and $[Pt_{24}(CO)_{30}]^{2-}$ [164].

In contrast, the voltammetric profiles of larger MMCCs display almost equally spaced redox waves, as in the case of $[Co_{38}As_{12}(CO)_{50}]^{4-}$ [151], $[Ni_{32}C_6(CO)_{36}]^{6-}$ [158], $[Ni_{37-x}Pd_{7+x}(CO)_{48}]^{6-}$ [71], $[HNi_{37-x}Pd_{7+x}(CO)_{48}]^{5-}$ [71], and $[Pt_{40}(CO)_{40}]^{6-}$ [72]. This corresponds to almost linear Z-plots (Fig. 16), and very similar $\Delta E^{\circ\prime}$ between all consecutive redox couples. It may be concluded that for these larger multivalent MMCCs, the pairing energy within a single molecular orbital is very similar to the energy gap between two consecutive orbitals.

An intermediate behavior between staircase-like and linear of the Z-plot has been observed for some MMCCs (Fig. 17), such as $[Co_{10}N_2(CO)_{19}]^{4-}$ [148], $[Rh_{16}Au_6(CO)_{36}]^{6-}$ [155], $[Ni_{25}(C_2)_4(CO)_{32}]^{4-}$ [157], and $[Pt_{38}(CO)_{44}]^{2-}$ [164]. In these cases, the Z-plots are almost linear, except for a single larger $\Delta E^{\circ\prime}$ corresponding to the difference between the first oxidation and first reduction, and, thus, somehow related to the HOMO-LUMO gap.

The plot of the average separations between the formal electrode potentials of consecutive redox couples of MMCC displaying multiple reversible redox changes ($\Delta E^{\circ\prime}_{av}$) *vs.* nuclearity is rather scattered (Fig. 19). This is somehow due to the fact that, at this length-scale, the structure of the cluster, the nature of the transition metal atoms involved, and the presence of additional main group atoms, affect significantly the electronic state of the clusters. Moreover, the data have been recorded under different experimental conditions, some of them very recently, others long time ago. Nonetheless, the general trend is a decrease of $\Delta E^{\circ\prime}_{av}$ as the MMCC nuclearity increases.

The largest MMCCs, which have been electrochemically investigated, have nuclearities 38–44 and display $\Delta E^{\circ\prime}_{av}$ = 0.2–0.3 V. This indicates that their metal cores still possess a semi-conductor nature, but metallization should occur by further increasing their nuclearity. A linear extrapolation of the $\Delta E^{\circ\prime}_{av}$ *vs.* nuclearity plot suggests that $\Delta E^{\circ\prime}_{av}$ might be close to zero at nuclearity *ca.* 70–90. To reach this nuclearity for homoleptic MCCs is a big challenge, also due to solubility issues. Moreover, as $\Delta E^{\circ\prime}_{av}$ gets closer to zero, spontaneous auto-disproportionation equilibria might occur in solution (Eq. (1)), making very difficult the isolation of a single species. Even though such limit has not been reached yet, in the case of some larger multivalent MMCCs, it has been observed by CV and IR-SEC that some oxidation states are considerably less stable than others. The limited stability of such oxidation states might be due to their disproportionation, suggesting some incipient metallization of such large MMCCs. Some examples will be presented in Section 3.3.

$$2\left[M_x(CO)_y\right]^{n-} \rightleftharpoons \left[M_x(CO)_y\right]^{(n+1)-} + \left[M_x(CO)_y\right]^{(n-1)-} \quad (1)$$

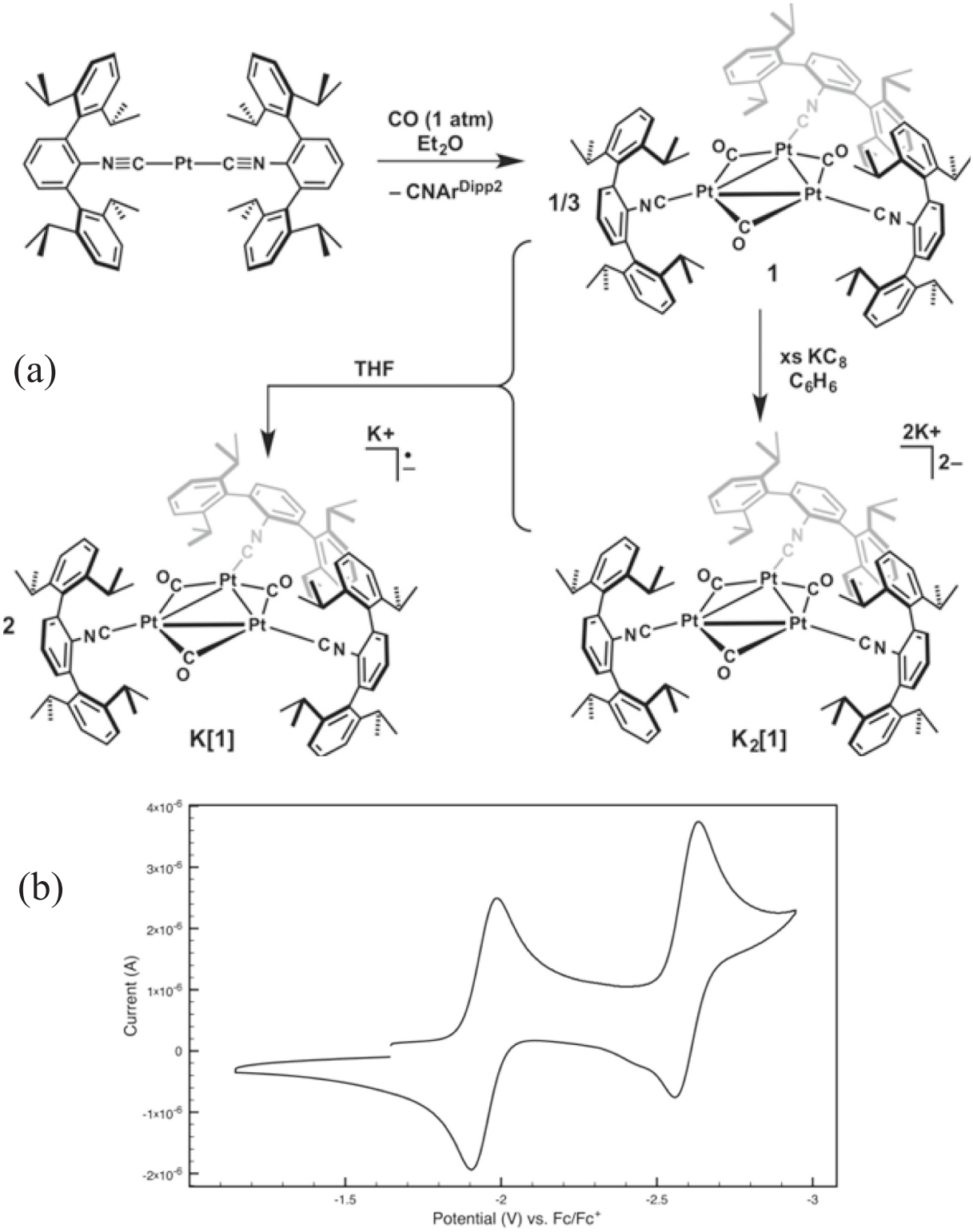

Fig. 10. (a) Synthesis of $[Pt_3(\mu\text{-}CO)_3(CNAr^{Dipp2})_3]^{n-}$ (n = 0–2) and (b) CV of $[Pt_3(\mu\text{-}CO)_3(CNAr^{Dipp2})_3]$. Adapted from Ref. [169] with permission from Wiley.

3.3. Homometallic Pt carbonyl clusters

The concepts presented in the previous Sections are well exemplified by the electrochemical study of homometallic homoleptic Pt carbonyl clusters. These can be grouped into two main categories, which display completely different electrochemical behaviors: (a) Chini clusters of general formula $[Pt_{3n}(CO)_{6n}]^{2-}$ (n = 1–10), displaying CO/Pt = 2; (b) globular Pt carbonyl nanoclusters, called also Pt browns in view of their color, with CO/Pt < 2 [173–175].

CV analyses of Chini clusters show only the presence of irreversible processes, in keeping with their known chemical reactivity. Indeed, the chemical oxidation of a selected Chini cluster $[Pt_{3n}(CO)_{6n}]^{2-}$ (n = 1–10) affords a larger cluster $[Pt_{3(n+1)}(CO)_{6(n+1)}]^{2-}$, whereas its chemical

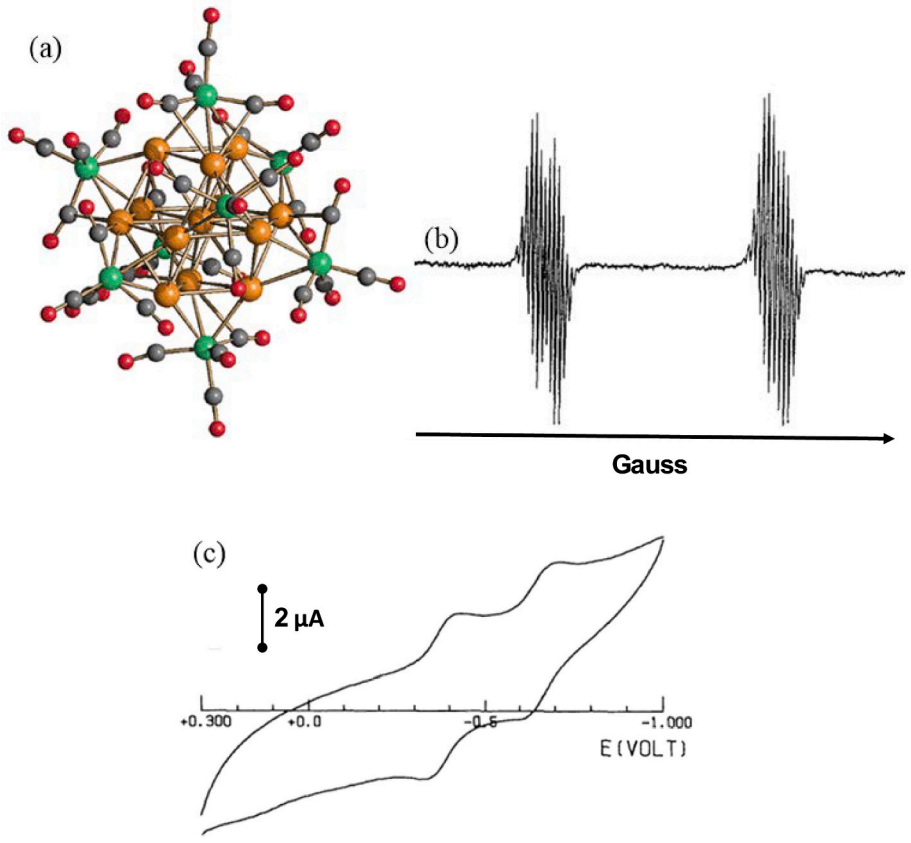

Complex	Ag-Ag	Ag-Fe
$[Ag_{13}Fe_8(CO)_{32}]^{3-}$	2.93	2.71
$[Ag_{13}Fe_8(CO)_{32}]^{4-}$	2.92	2.74
$[Ag_{13}Fe_8(CO)_{32}]^{5-}$	2.90	2.75

Fig. 11. (a) Molecular structure of $[Ag_{13}Fe_8(CO)_{32}]^{n-}$ (n = 3–5) (orange, Ag; green, Fe; red, O; grey, C), (b) EPR spectrum of $[Ag_{13}Fe_8(CO)_{32}]^{4-}$ recorded at 300 K on CH_3CN solution, and (c) CV of $[Ag_{13}Fe_8(CO)_{32}]^{3-}$ recorded at a Pt electrode on CH_3CN solution with $[N^nBu_4][ClO_4]$ at 0.2 V s^{-1}. The table reports the average bond lengths (Å) of $[Ag_{13}Fe_8(CO)_{32}]^{n-}$ (n = 3–5). Adapted with permission from Ref. [171]. Copyright 1992 American Chemical Society.

reduction results into a smaller cluster $[Pt_{3(n-1)}(CO)_{6(n-1)}]^{2-}$ [176]. As an example, the CV of $[Pt_9(CO)_{18}]^{2-}$ in DMF is reported in Fig. 20. It displays three irreversible oxidation processes at E_{pa} = –0.42, –0.30 and –0.08 V, that correspond to the oxidation of $[Pt_9(CO)_{18}]^{2-}$ to $[Pt_{12}(CO)_{24}]^{2-}$, $[Pt_{15}(CO)_{30}]^{2-}$, and $[Pt_{18}(CO)_{36}]^{2-}$, respectively [177].

Due to their compact structures and the predominance of Pt-Pt over Pt-CO bonds, several Pt browns are redox active and behave as electron-sinks [33,178,179]. The compounds so far electrochemically investigated are (the structure of their metal core is reported in brackets): $[Pt_{19}(CO)_{22}]^{4-}$ (centered pentagonal prismatic) [164,165], $[Pt_{24}(CO)_{30}]^{2-}$ (*ccp*, regular) [164], $[Pt_{26}(CO)_{32}]^{2-}$ (*hcp*, regular) [166], $[Pt_{27}(CO)_{31}]^{4-}$ (*ccp*, defective) [83], $[Pt_{33}(CO)_{38}]^{2-}$ (*ccp*, defective) [72], $[Pt_{38}(CO)_{44}]^{2-}$ (*ccp*, regular) [164], $[Pt_{40}(CO)_{40}]^{6-}$ (*bcc*, regular) [72]. Up to 6-9 redox states have been identified for these MCCs by combined CV and IR-SEC studies. The multivalence of Pt browns is an indication of the incipient metallization of their metal cores and is favored by the presence of strong Pt-Pt bonds, which hamper fragmentation upon oxidation/reduction.

Most of the redox processes of Pt browns involve one electron, and all the species $[Pt_{19}(CO)_{22}]^{n-}$ (n = 2–9) [164,165], $[Pt_{24}(CO)_{30}]^{n-}$ (n = 0–6) [164], $[Pt_{38}(CO)_{44}]^{n-}$ (n = 0–6) [164], and $[Pt_{40}(CO)_{40}]^{n-}$ (n = 4–11) [72] (Fig. 21 and Table 5) have been electrochemically and/or spectroelectrochemically detected. In some cases, the number of electrons involved has been directly determined by controlled potential coulometric tests. One-electron redox processes of Pt brows usually cause a shift of ±12–18 cm^{-1} of ν_{CO} after each addition (–) or removal (+) of one electron. Thus, IR-SEC may be used as an alternative method to determine the number of electrons involved.

IR-SEC of the redox processes of $[Pt_{38}(CO)_{44}]^{2-}$ shows that electrogenerated odd-electron species are less stable than even-electron ones. This is likely to be due to disproportionation of odd-electron species in the timescale of IR-SEC, as depicted in Eq. (1). Similarly, in the case of $[Pt_{27}(CO)_{31}]^{4-}$ [83] and $[Pt_{33}(CO)_{38}]^{2-}$ [72] all the electrogenerated species $[Pt_{27}(CO)_{31}]^{n-}$ (n = 3–6, 8) and $[Pt_{33}(CO)_{38}]^{n-}$ (n = 0–4, 6–9) have been characterized by IR-SEC, whereas $[Pt_{27}(CO)_{31}]^{7-}$ and $[Pt_{33}(CO)_{38}]^{5-}$ resulted to be very elusive. In the case of $[Pt_{27}(CO)_{31}]^{n-}$, the turquoise spectrum of Fig. 22 represents the highest concentration obtained in our conditions of a species with charge −7, as was demonstrated by deconvolution analysis on two selected intermediate spectra of the reduction sequence [83].

As a limiting case, almost all the redox processes analyzed by CV and IR-SEC for $[Pt_{26}(CO)_{32}]^{2-}$ involve two electrons (Table 6) [166], leading

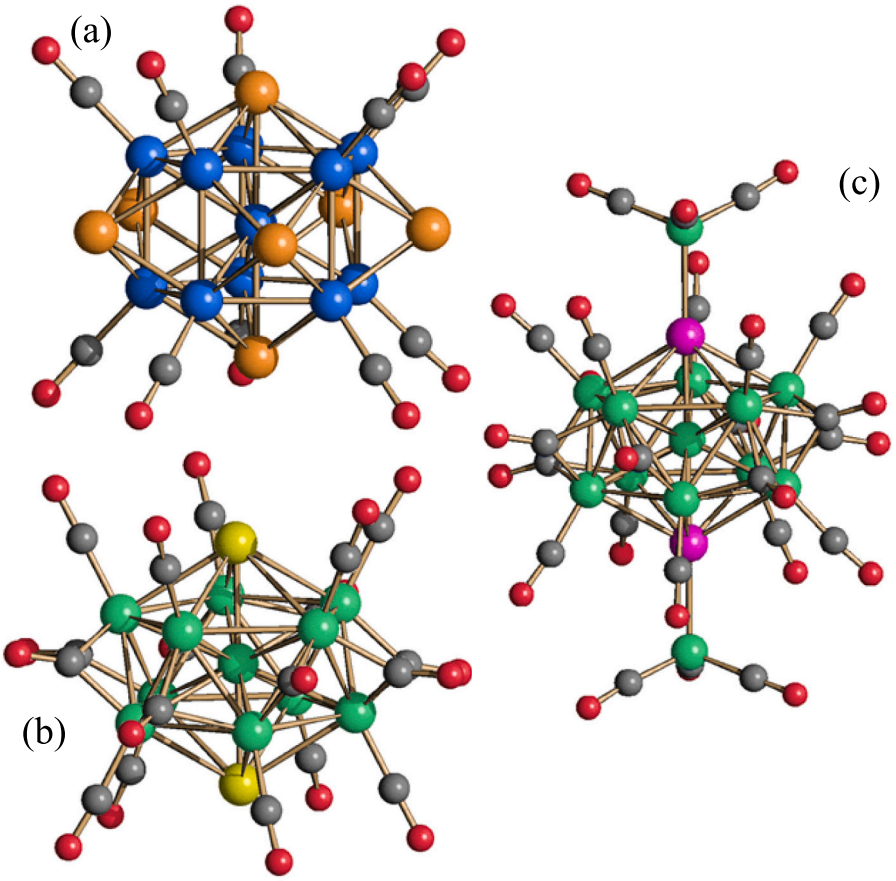

Fig. 12. Some examples of MMCCs with one fully interstitial late transition metal atom displaying two or more electrochemical redox reversible processes: (a) $[Co_{11}Te_7(CO)_{10}]^-$, (b) $[Ni_{11}Bi_2(CO)_{18}]^{3-}$, and (c) $[Ni_{13}Sb_2(CO)_{24}]^{3-}$ (blue, Co; orange, Te; green, Ni; yellow, Bi; purple, Sb; red, O; grey, C).

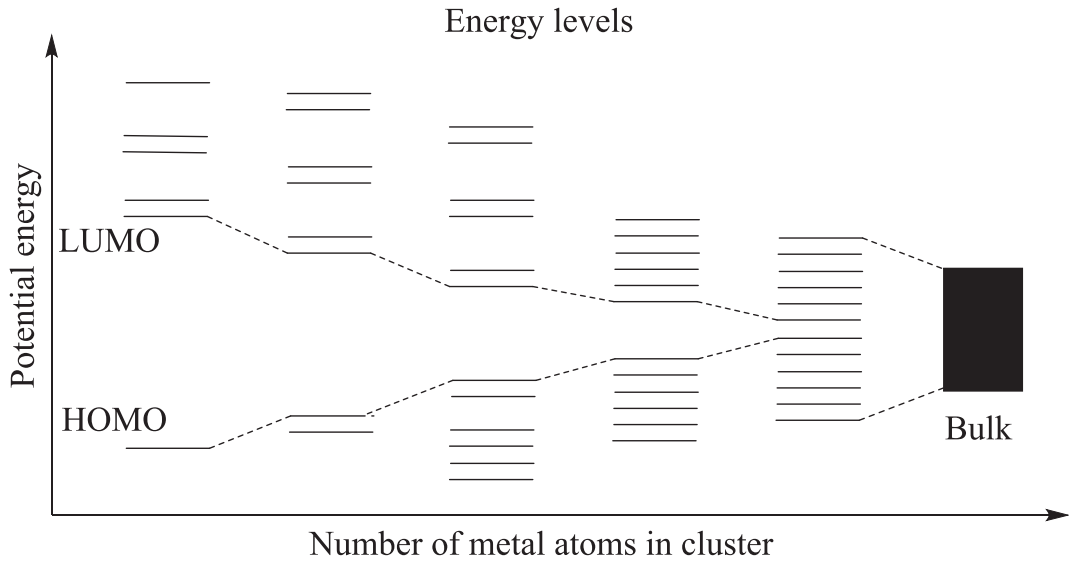

Fig. 13. Schematic representation of the decrease of the HOMO-LUMO gap with increasing cluster nuclearity.

to the characterization of the species $[Pt_{26}(CO)_{32}]^{n-}$ (n = 2, 4, 6, 8, 10). The species $[Pt_{26}(CO)_{32}]^-$ and $[Pt_{26}(CO)_{32}]^{7-}$ have been observed only in some solvents. The two-electron nature of the redox processes is confirmed by a variation of ±30–35 cm^{-1} of ν_{CO}, almost the double than observed for one-electron processes.

Even if all Pt browns analyzed display both oxidation and reduction electrochemical processes, the number of reductions is usually greater than oxidations. Oxidation processes are somehow limited by stability issues as well as adsorption on the electrode of neutral or less charged species. Generally speaking, MMCCs seem to be more prone to reduction and charges down to 8– or 11– have been observed during IR-SEC. This is in keeping with the π-acid character of CO ligands.

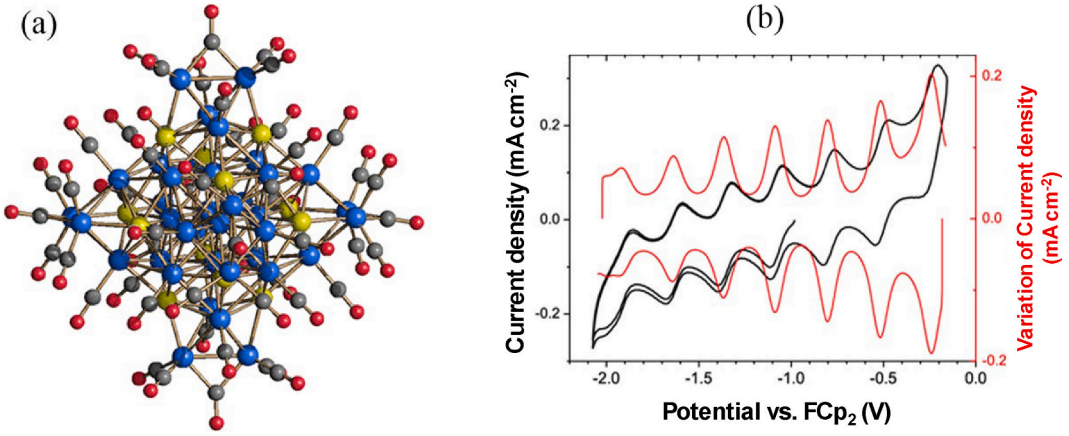

Fig. 14. (a) Molecular structure (blue, Co; yellow, As; red, O; grey, C), and (b) CV (black) and DPV (red) responses in CH_3CN solution of $[Co_{38}As_{12}(CO)_{50}]^{4-}$ displaying seven reversible redox processes. Adapted with permission from Ref. [151]. Copyright 2022 American Chemical Society.

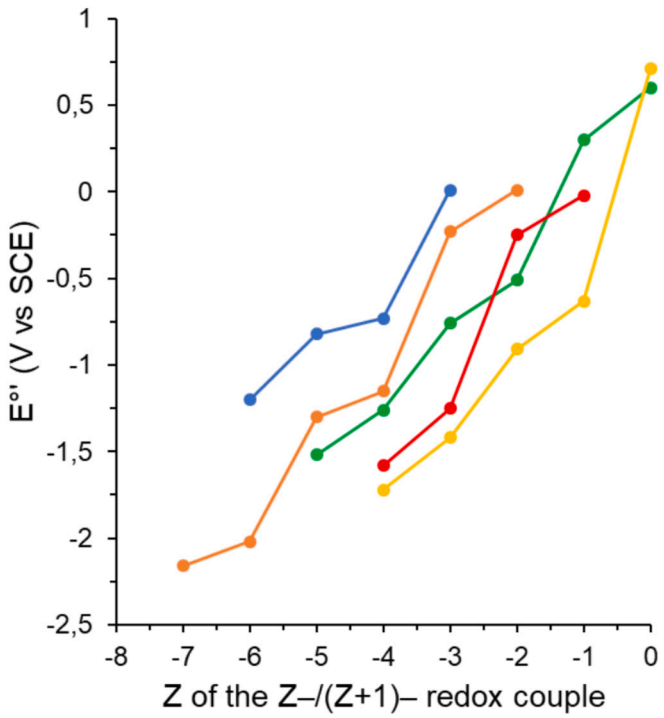

Fig. 15. Staircase-like Z-plots of the formal redox potentials ($E^{\circ\prime}$ *vs.* SCE) of $[Co_{10}AuC_2(CO)_{24}]^-$ (yellow), $[HRh_{14}(CO)_{25}]^{3-}$ (red), $[H_4Rh_{22}(CO)_{35}]^{4-}$ (blue), $[Pt_{19}(CO)_{22}]^{4-}$ (orange), and $[Pt_{24}(CO)_{30}]^{2-}$ (green).

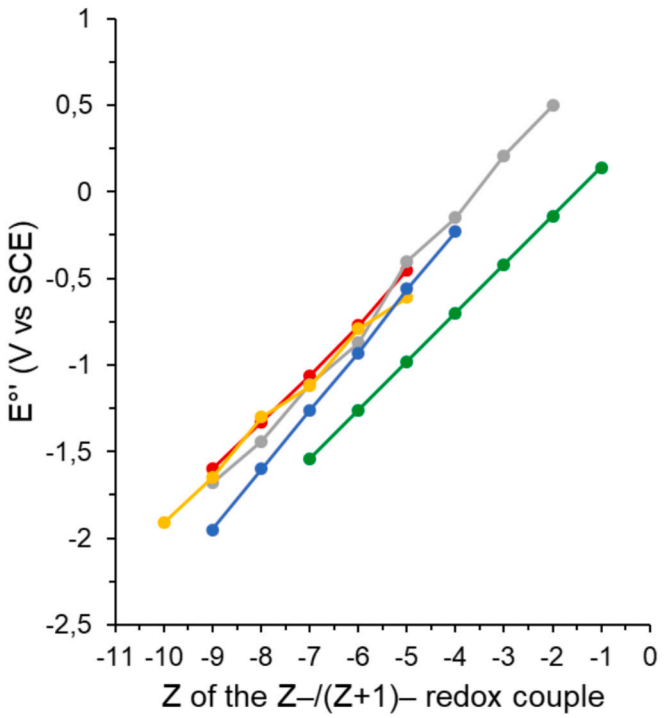

Fig. 16. Linear trend of Z-plots of the formal redox potentials ($E^{\circ\prime}$ *vs.* SCE) of $[Co_{38}As_{12}(CO)_{50}]^{4-}$ (green), $[Ni_{32}C_6(CO)_{36}]^{6-}$ (red), $[Ni_{37-x}Pd_{7+x}(CO)_{48}]^{6-}$ (yellow), $[HNi_{37-x}Pd_{7+x}(CO)_{48}]^{5-}$ (blue), and $[Pt_{40}(CO)_{40}]^{6-}$ (grey).

In some cases, electrogenerated odd electron species have been trapped at low temperature and characterized by EPR spectroscopy, as in the case of $[Pt_{24}(CO)_{30}]^-$ [166,178]. Sometimes, it has been possible to chemically generate some oxidized or reduced species observed by CV or IR-SEC. Nonetheless, isolation and structural characterization by SC-XRD have been possible only in the case of $[Pt_{26}(CO)_{32}]^-$, which resulted to be isostructural with parent $[Pt_{26}(CO)_{32}]^{2-}$ [174]. More often, chemically generated species evolve during work-up or crystallization, resulting in new clusters. For instance, stepwise chemical oxidation of $[Pt_{19}(CO)_{22}]^{4-}$ affords $[Pt_{19}(CO)_{22}]^{3-}$, $[Pt_{19}(CO)_{22}]^{2-}$ and $[Pt_{19}(CO)_{22}]^-$, which are transformed upon crystallization into $[Pt_{40}(CO)_{40}]^{6-}$, $[Pt_{36}(CO)_{44}]^{2-}$, and $[Pt_{38}(CO)_{44}]^{2-}$, respectively [174].

3.4. *Heterometallic Ni-Pt and Ni-Pd carbonyl clusters*

Heterometallic Ni-Pt MMCCs may reach high nuclearities and often display electron-sponge behavior. Their electrochemical study offers the possibility to investigate two interesting features:

1) Modulation of the redox behavior of MMCCs by protonation/deprotonation;
2) Modulation of the redox behavior by Ni/Pt substitution of isostructural MMCCs.

The first feature may be evidenced by analyzing the couples of protonated/deprotonated clusters $[HNi_{36}Pt_4(CO)_{45}]^{5-}$ and $[Ni_{36}Pt_4(CO)_{45}]^{6-}$ [160], $[HNi_{35}Pt_9(CO)_{48}]^{5-}$ and $[Ni_{35}Pt_9(CO)_{48}]^{6-}$ [161], $[HNi_{38}Pt_6(CO)_{48}]^{5-}$ and $[Ni_{38}Pt_6(CO)_{48}]^{6-}$ [162] (Table 4).

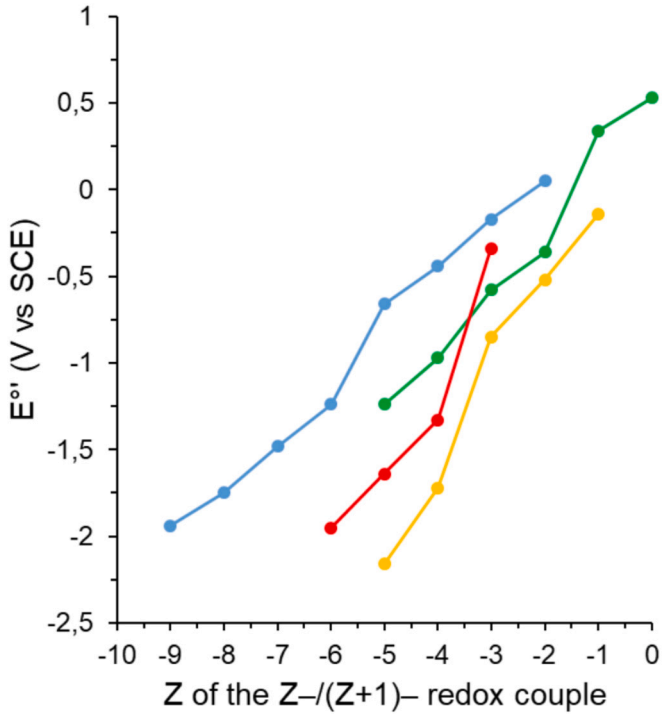

Fig. 17. Z-plots with intermediate behavior between staircase and linear of the formal redox potentials ($E^{\circ\prime}$ *vs.* SCE) of $[Co_{10}N_2(CO)_{19}]^{4-}$ (yellow), $[Rh_{16}Au_6(CO)_{36}]^{6-}$ (blue), $[Ni_{25}(C_2)_4(CO)_{32}]^{4-}$ (red), and $[Pt_{38}(CO)_{44}]^{2-}$ (green).

These may be easily interconverted by protonation/deprotonation reactions using acids and bases. Within each couple, the same redox change occurs at more negative potentials in the case of the hydride species compared to the non-hydride one (Fig. 23). This is probably because, considering clusters with the same negative charge, the hydride species has one additional electron compared to the non-hydride one. As a further consequence, often hydrides derivatives display fewer reductions and an increased number of oxidation steps compared to the related non-hydride cluster. The possibility to modulate the redox behavior of MCCs by protonation/deprotonation is not limited to Ni-Pt clusters, but it is often found also in other high nuclearity MCCs, see for instance the entries $[HNi_{38}C_6(CO)_{42}]^{5-}$ and $[Ni_{38}C_6(CO)_{42}]^{6-}$ [158], $[HNi_{37-x}Pd_{7+x}(CO)_{48}]^{5-}$ and $[Ni_{37-x}Pd_{7+x}(CO)_{48}]^{6-}$ [71] of Table 4. This topic will be further discussed in Section 4.2.

The second feature is not so straightforward as protonation/deprotonation, since Ni/Pt replacement requires dedicated and not trivial syntheses. For instance, $[Ni_{38}Pt_6(CO)_{48}]^{6-}$ contains an inner Pt_6 octahedron and 38 surface Ni atoms [162]. The formal replacement by Pt of three Ni atoms on the surface leads to the closely related $[Ni_{35}Pt_9(CO)_{48}]^{6-}$ (Fig. 24) [161]. Both clusters are multivalent, but the redox potentials are shifted toward more negative potential in the case of the Pt-richer species (Fig. 25). Moreover, the presence of more Pt in $[Ni_{35}Pt_9(CO)_{48}]^{6-}$ seems to favor oxidation and disfavor reduction processes compared to $[Ni_{38}Pt_6(CO)_{48}]^{6-}$. Similar considerations apply to the closely related $[HNi_{38}Pt_6(CO)_{48}]^{5-}$ and $[HNi_{35}Pt_9(CO)_{48}]^{5-}$. These phenomena might be explained based on the smaller propensity to back-donation of Pt compared to Ni, which leads to a minor stabilization of the more reduced species. This point is further supported by IR spectroscopy, which shows identical ν_{CO} patterns for $[Ni_{38}Pt_6(CO)_{48}]^{6-}$/$[Ni_{35}Pt_9(CO)_{48}]^{6-}$ and $[HNi_{38}Pt_6(CO)_{48}]^{5-}$/$[HNi_{35}Pt_9(CO)_{48}]^{5-}$, but shifted to higher wavenumbers (5-10 cm^{-1}) for the Pt-richer species. A less pronounced tendency toward oxidation upon replacement of Pt with Ni has been observed also in the case of $[Pt_{19}(CO)_{22}]^{4-}$ and $[Pt_{19-x}Ni_x(CO)_{22}]^{4-}$ (x = 3.11) [165].

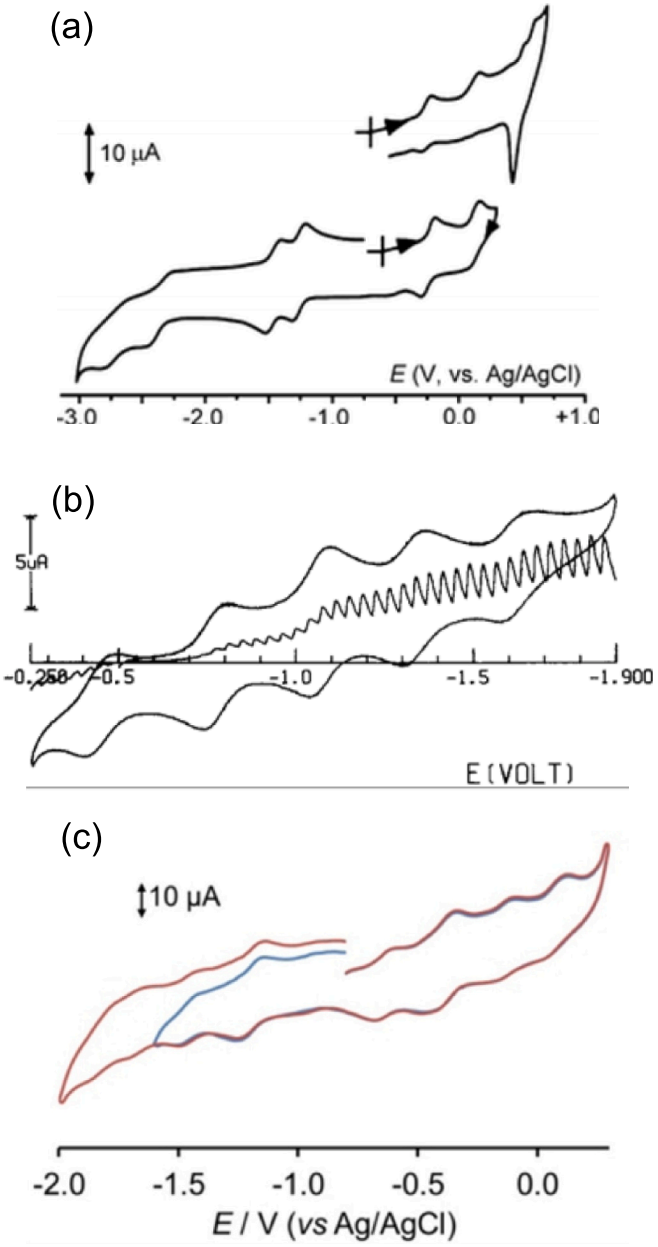

Fig. 18. Representative examples of CV profiles of MMCCs displaying (a) staircase-like, (b) linear and (c) intermediate Z-plots. (a) $[Pt_{19}(CO)_{22}]^{4-}$ in DMF solution, $[NEt_4][PF_6]$ supporting electrolyte, scan rate 0.2 V s^{-1}. Adapted from [164] with permission from Springer (2009). (b) $[Ni_{32}C_6(CO)_{36}]^{6-}$ in CH_3CN solution, $[NEt_4][ClO_4]$ supporting electrolyte, scan rates: CV 0.2 V s^{-1}, d.c. voltammogram 0.02 V s^{-1}. Adapted from [158] with permission from Wiley (1999). (c) $[Rh_{16}Au_6(CO)_{36}]^{6-}$ in CH_3CN solution, $[N^nBu_4][PF_6]$ supporting electrolyte, scan rate 0.2 V s^{-1}. Adapted from [155] with permission from Wiley (2024).

It was believed for longtime that, due to weaker Pd-Pd, Pd-CO and Ni-Pd bonds, heterometallic Ni-Pd MMCCs were not sufficiently stable to undergo reversible redox processes. Nonetheless, it has been recently demonstrated by combined CV and IR-SEC studies that $[Ni_{29-x}Pd_{6+x}(CO)_{42}]^{6-}$ (x = 0.09), $[Ni_{22-x}Pd_{20+x}(CO)_{48}]^{6-}$ (x = 0.62), $[Ni_{36-x}Pd_{5+x}(CO)_{46}]^{6-}$ (x = 0.41), $[Ni_{37-x}Pd_{7+x}(CO)_{48}]^{6-}$ (x = 0.69), and $[HNi_{37-x}Pd_{7+x}(CO)_{48}]^{5-}$ (x = 0.53) are multivalent [71,80]. In the case of $[Ni_{37-x}Pd_{7+x}(CO)_{48}]^{6-}$ (x = 0.69), and $[HNi_{37-x}Pd_{7+x}(CO)_{48}]^{5-}$ (x = 0.53), which are isostructural to $[Ni_{38}Pt_6(CO)_{48}]^{6-}$/$[Ni_{35}Pt_9(CO)_{48}]^{6-}$ and $[HNi_{38}Pt_6(CO)_{48}]^{5-}$/$[HNi_{35}Pt_9(CO)_{48}]^{5-}$, it seems that introducing Pd atoms shifts the redox potentials to less

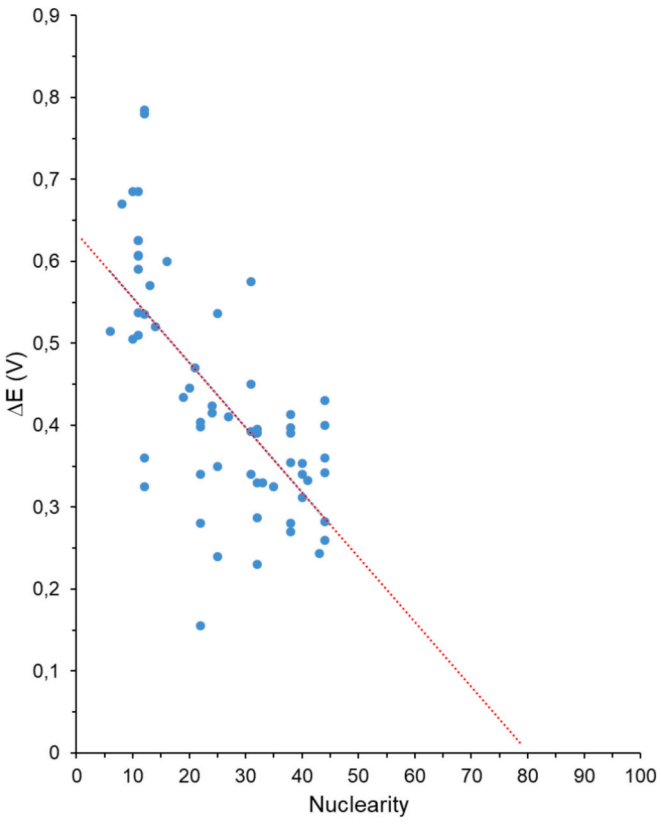

Fig. 19. Experimental average separation of consecutive redox couples ($\Delta E^{\circ\prime}_{av}$ in V) as a function of the nuclearity of the cluster. Data from Table 4.

negative values and favors more reduced species (Figs. 26 and 27).

3.5. MMCCs containing main group elements

The presence of one or more interstitial main group elements such as C, Si, N, P, As, Sb, Bi, S, and Te, has been shown to support the multivalence and electron sink behavior of MMCCs, as these inner atoms strengthen the metal core by enhancing metal–metal interactions. Moreover, doping of a metal cluster by inserting a different element can favorably modify the molecular orbital diagram, thereby facilitating electron addition or removal in MMCCs. Several examples of multivalent MMCCs containing main group elements are present in Table 4 and presented in other Sections. Herein, we will focus on the $[Rh_{12}E(CO)_{27/28}]^{n-}$ (E = In, Ge, Sn, Sb, Bi) species as case study [104,180,181].

The multivalence is shared between all five members of the $[Rh_{12}E(CO)_{27/28}]^{n-}$ family of clusters and has been unraveled by electrochemical studies through *in situ* IR SEC [104,180,181]. These clusters exemplify cases where CV yields low currents and poorly defined peaks, or where redox features are barely discernible on conventional WEs, such as Pt or GC. Under such conditions, conventional electrochemical methods, including CV and controlled potential coulometry, often fail to provide reliable information on the reversibility of redox processes or on the number of electrons exchanged. In contrast, IR SEC experiments performed in an OTTLE cell allow the gradual variation of the WE potential within a defined window, while collecting time-resolved vibrational spectra in the carbonyl region. With an appropriate potential range, it becomes possible to observe fully reversible shifts of ν_{CO} bands to higher or lower wavenumbers upon oxidation or reduction, respectively. These spectral changes involve both terminal (ν^{t}_{CO}) and bridging (ν^{b}_{CO}) carbonyl ligands, providing direct molecular insight into the redox behavior of the cluster.

When the WE potential is gradually swept across a defined range in solutions of high-nuclearity MCCs, multiple redox events can be observed. The resulting series of IR spectra can typically be grouped according to the different redox states accessed during the experiment, allowing the identification of long-lived electrogenerated species with distinct charge states. The appearance or absence of clear isosbestic points within each spectral group serves as an indicator of the relative stability of intermediates, or alternatively, of competing processes that may complicate the electron transfer steps. In high-nuclearity clusters, a relatively uniform shift of terminal CO bands in the range of 14–20 cm^{-1} is generally associated with single-electron transfers, whereas shifts of approximately 28–40 cm^{-1} are indicative of two-electron processes.

Beyond tracking redox states, IR SEC also provides valuable insight into: (a) the kinetic persistence of oxidized or reduced species beyond the timescale accessible by CV, suggesting potential for their chemical isolation, and (b) structural reorganizations following redox events, often reflected in significant changes in the vibrational profile. For instance, changes in the charge state of a cluster can lead to variations in the intensity ratio between terminal and bridging carbonyl bands, highlighting modifications in the coordination geometry of CO ligands. This trend aligns with the tendency of carbonyl ligands to adopt bridging positions more readily as the overall cluster charge becomes increasingly negative [182–184].

Within the heterometallic icosahedral, isostructural, and

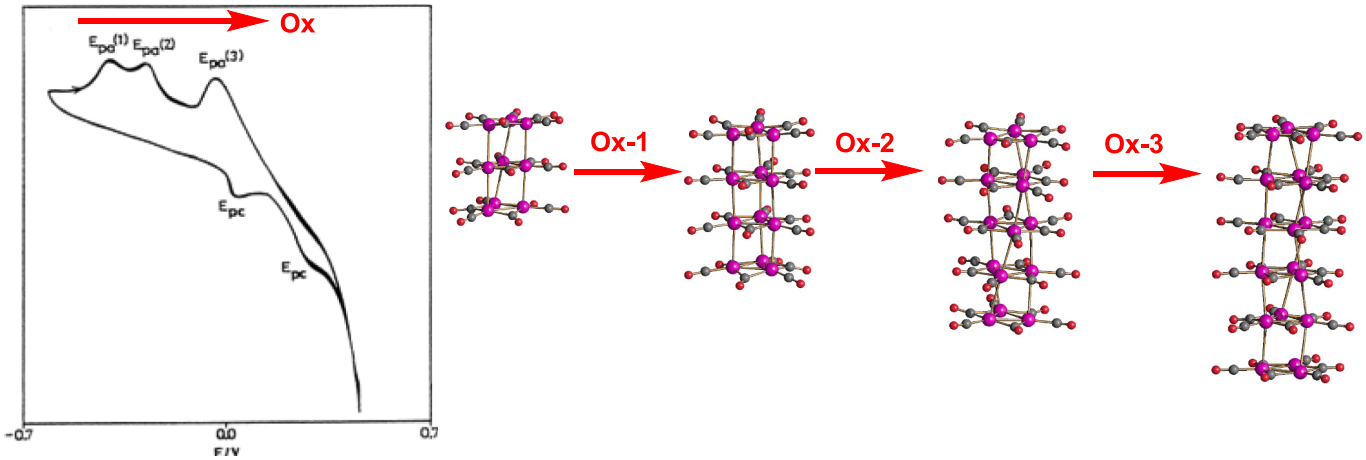

Fig. 20. CV of $[Pt_9(CO)_{18}]^{2-}$ in DMF, scan rate 50 mV s^{-1}. $[N^nBu_4][BF_4]$ as supporting electrolyte. Three consecutive irreversible oxidation processes lead to $[Pt_{12}(CO)_{24}]^{2-}$, $[Pt_{15}(CO)_{30}]^{2-}$, and $[Pt_{18}(CO)_{36}]^{2-}$ (purple, Pt; red, O; grey, C). Adapted with permission from Ref. [177]. Copyright 2001 American Chemical Society.

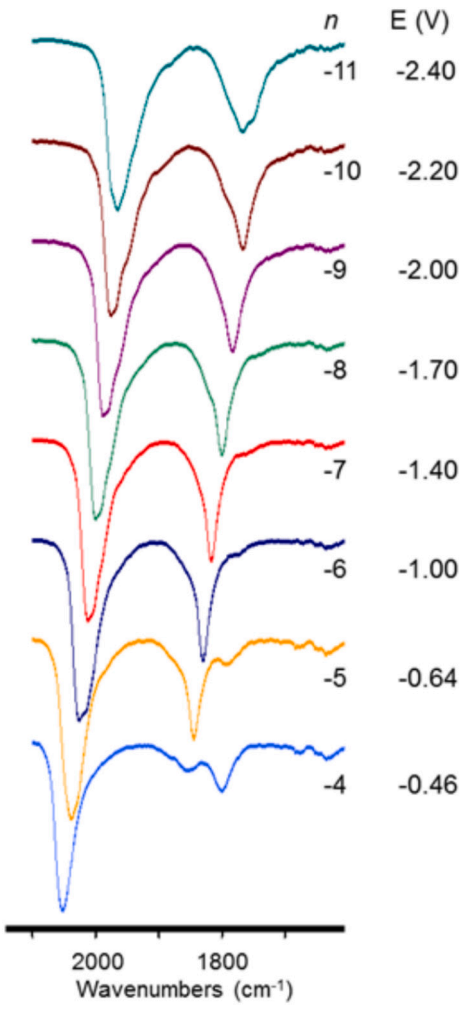

Fig. 21. IR-SEC selected spectra of $[Pt_{40}(CO)_{40}]^{n-}$ (n = 4-11). Adapted with permission from Ref. [72]. Copyright 2016 American Chemical Society.

Table 5
Infrared stretching frequencies (cm^{-1}) of terminal (ν^t_{CO}) and bridging (ν^b_{CO}) carbonyl groups for $[Pt_{40}(CO)_{40}]^n$ in CH_3CN as a function of the cluster charge *n*.

Cluster charge *n*	ν^t_{CO}	ν^b_{CO}
−4	2051	1856, 1799
−5	2039	1845
−6	2027	1831
−7	2012	1817
−8	2000	1800
−9	1988	1783
−10	1976	1767
−11	1966	1767, 1752(sh)

isoelectronic $[Rh_{12}E(CO)_{27/28}]^{n-}$ clusters (E = In, Ge, Sn, Sb, Bi), only the indium derivative, $[Rh_{12}In(CO)_{28}]^{3-}$, displays a well-defined CV profile. Nevertheless, the electrochemical quasi-reversibility of its redox processes (particularly the reduction) was primarily established through in situ IR SEC. For the remaining congeners, whose voltammetric responses are poorly resolved or featureless, IR SEC proved essential for detecting distinct and stable redox states revealing their multivalent behavior. Among them, the Sb-containing cluster, $[Rh_{12}Sb(CO)_{27}]^{3-}$, exhibited the most regular and fully reversible electrochemical profile, characterized by five consecutive one-electron redox events spanning formal charge states from −2 to −6, each associated with a well-defined IR spectrum.

By contrast, $[Rh_{12}Sn(CO)_{27}]^{4-}$ showed a markedly lower redox flexibility, with only a single stable oxidation step being observed, and no clearly resolved reduction events. Similarly, the Ge and Bi derivatives demonstrated intermediate behavior: $[Rh_{12}Ge(CO)_{27}]^{4-}$ underwent two successive one-electron oxidations, while $[Rh_{12}Bi(CO)_{27}]^{3-}$ displayed only one. In both cases, reduction led exclusively to even-electron species (*i.e.* $[Rh_{12}Ge(CO)_{27}]^{6-}$ and $[Rh_{12}Bi(CO)_{27}]^{5-/7-}$) while the intermediate odd-electron states could not be directly isolated but were inferred through spectral deconvolution. A similar situation was encountered for $[Rh_{12}In(CO)_{28}]^{3-}$, where the pentaanion $[Rh_{12}In(CO)_{28}]^{5-}$ was clearly identified, but no spectroscopic evidence for the intermediate $[Rh_{12}In(CO)_{28}]^{4-}$ species could be obtained. According to Continuous Shape Measures on the DFT-optimized structures, the reduction of $[Rh_{12}In(CO)_{28}]^{3-}$ to $[Rh_{12}In(CO)_{28}]^{5-}$ should also cause a distortion of the icosahedral arrangement of the Rh centers. Fig. 28 summarizes the redox behavior of the full series as established by IR SEC experiments [185].

4. Interplay between electrochemical properties and structural features of MMCCs

Electrochemical properties and structural features of MMCCs are strictly related and reciprocally interconnected. From one side, addition/removal of electrons may cause structural changes of MMCCs. Minor changes may involve modification of the carbonyl stereochemistry, small variations in bond lengths, or small distortions of the original symmetry. Larger structural changes may lead to the variation of the geometry of the cluster core, elimination of some CO ligands, cluster condensation or fragmentation, up to complete cluster decomposition. Usually, the extent of the structural change is somehow related to the electrochemical reversibility of the redox process. Ideally, complete electrochemical reversibility should require the absence of any structural rearrangement upon addition/removal of electrons. Indeed, departure from canonical electrochemical reversibility often arises from minor structural changes, leading to quasi-reversible electrochemical processes [48]. If larger structural changes are involved, the electrochemical processes gradually lose reversibility and become irreversible. Structural changes induced by redox reactions will be discussed and exemplified in Section 4.1.

On the other side, the introduction of some small structural variations in otherwise isostructural MMCCs may cause changes of their redox properties. As shown in Section 3.4, the most straightforward method to tune the redox properties of MMCCs is the addition/removal of a hydride ligand *via* acid/base reactions. Alternatively, one or more CO ligands may be replaced by other ligands, or M/M' substitution may be performed in heterometallic clusters. The effects of structural changes on the redox properties of MMCCs will be further discussed in Section 4.2.

4.1. Structural changes induced by redox reactions on MMCCs

Because of the strong π-acidic character of CO, π-back-donation from the cluster core to the CO ligands is largely affected by the MMCC charge. Thus, π-back-donation should increase upon MMCC reduction and decrease upon oxidation. Consequently, the ν_{CO} bands should move to lower wavenumbers upon MMCC reduction and, vice versa, to higher wavenumbers upon oxidation (see also Sections 2.3, 3.3, and 3.5). At the same time, an increased π-back-donation should also favor to some extent bridging coordination of the carbonyl ligands compared to terminal mode. Indeed, in several instances, IR-SEC experiments demonstrated an increase of the relative intensity of bridging ν_{CO} bands versus terminal ones, upon cluster reduction [102,182–184]. This point is well exemplified by IR-SEC studies of $[Pt_{40}(CO)_{40}]^{6-}$ (Fig. 21) and $[Ni_{36-x}Pd_{5+x}(CO)_{46}]^{6-}$ (x = 0.41) (Fig. 29).

Alternatively, the addition of two moles of electrons per cluster may lead to the elimination of one CO ligand with concomitant increase of the anionic charge of the cluster of two units. This point will be further

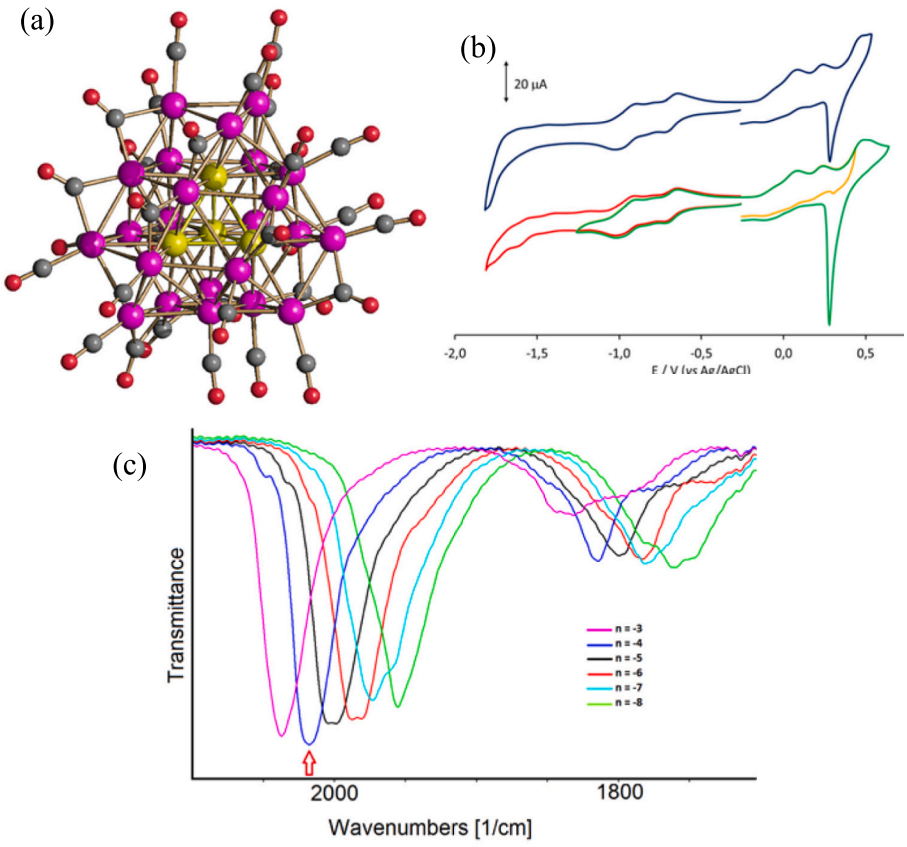

Fig. 22. (a) Molecular structure (purple, superficial Pt; yellow, interstitial Pt; red, O; grey, C), (b) CV at Pt (top) and GC (bottom) electrode, CH_3CN solution, $[N^nBu_4][PF_6]$ (0.1 mol dm^{-3}) as supporting electrolyte; scan rate: 0.1 V s^{-1}, and (c) IR-SEC selected spectra of $[Pt_{27}(CO)_{31}]^{4-}$. Adapted with permission from Ref. [83]. Copyright 2022 American Chemical Society.

Table 6
Infrared stretching frequencies (cm^{-1}) of terminal (ν^t_{CO}) and bridging (ν^b_{CO}) carbonyl groups for $[Pt_{26}(CO)_{32}]^n$ in CH_3CN as a function of the cluster charge *n*.

Cluster charge *n*	ν^t_{CO}	ν^b_{CO}
−2	2048	1803
−4	2020	1768
−6	1983	1769
−8	1955	1769
−10	1920	1741

discussed in Section 5.

Instead of influencing the CO ligands, redox reactions may affect the metal core of the cluster. Roughly speaking, this depends on the nature of the molecular orbitals involved in the redox processes. If electrons are added/removed to/from MOs with mainly M-CO bonding or antibonding character, the redox event will mainly affect the CO ligands, as mentioned above. In contrast, if the redox process add/remove electrons to/from MOs mainly involving M-M interactions, it will affect somehow the metal cage of the MMCCs. Unfortunately, the generally delocalized nature of occupied and empty molecular orbitals in MMCCs makes a qualitative interpretation of the experimental outcomes sometimes difficult. Orbital composition analyses based on partitioning approaches such as the Hirshfeld one can be helpful to shed more light on the localization of the molecular orbitals [186]. An example concerning the frontier orbitals of $[Rh_{16}Au_6(CO)_{36}]^{6-}$ is provided in Fig. 30 [155].

It is worth noting that the number of molecular orbitals doubles when electronic structures with unpaired electrons are simulated using an unrestricted computational approach. Moreover, a clear distinction between M-M and M-E-M bonds (E = bridging atom) is sometimes complicated, in particular in the presence of interstitial atoms or μ-CO

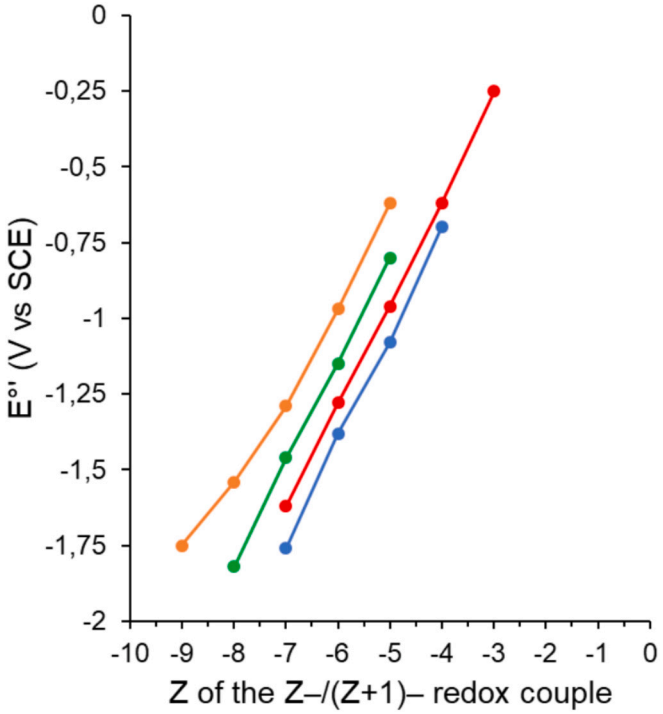

Fig. 23. Linear trend of Z-plots of the formal redox potentials ($E^{\circ\prime}$ *vs.* SCE) of the couples of protonated/deprotonated clusters $[HNi_{36}Pt_4(CO)_{45}]^{5-}$ (blue) and $[Ni_{36}Pt_4(CO)_{45}]^{6-}$ (green), $[HNi_{38}Pt_6(CO)_{48}]^{5-}$ (red) and $[Ni_{38}Pt_6(CO)_{48}]^{6-}$ (orange).

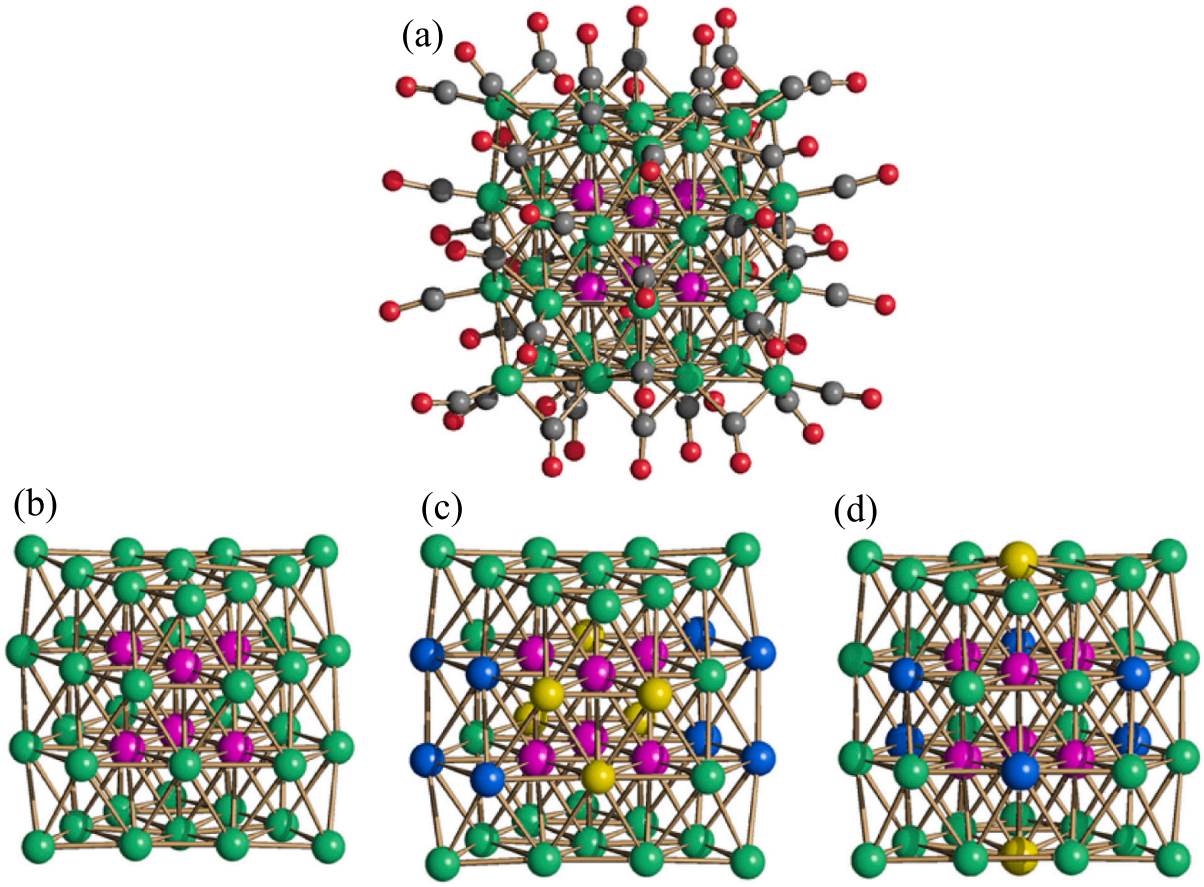

Fig. 24. (a) Molecular structure of $[Ni_{38}Pt_6(CO)_{48}]^{6-}$ and (b) its metal core (purple, Pt; green, Ni; red, O; grey, C). Metal cores of (c) $[Ni_{35}Pt_9(CO)_{48}]^{6-}$ (purple, Pt; green, Ni, yellow, Ni/Pt ≈ 57:43; blue, Ni/Pt ≈ 93:7) and (d) $[Ni_{37-x}Pd_{7+x}(CO)_{48}]^{6-}$ (x = 0.69) (green, Ni; purple, Pt, yellow, Ni/Pd ≈ 33:67; blue, Ni/Pd ≈ 91:9; grey, C; red, O). Adapted with permission from Ref. [71]. Copyright 2021 American Chemical Society.

ligands. In situations of this type, there can be the lack of (3,−1) bond critical points (BCPs) between two adjacent transition metals, as observable for instance for the $[M_6C(CO)_{15}]^{4-}$ clusters (M = Fe, Ru) in Fig. 31 [105,106]. The number of localized critical points in the two examples provided satisfies the Poincaré-Hopf relationship [187].

In such a scenario, three possible major events involving the metal core are possible because of a redox process, in addition to influencing the CO ligands as mentioned above: (1) polyhedral rearrangement, (2) variation of some M-M distances, (3) breaking of a M-M bond.

Reversible polyhedral rearrangement upon an electrochemical process of MMCCs is rather rare. The most noticeable example is the transformation of the bicapped tetrahedral cluster $[Os_6(CO)_{18}]$ (84 CVE) into the octahedral $[Os_6(CO)_{18}]^{2-}$ (86 CVE) upon the addition of two electrons (Fig. 32). The process is reversible and may be achieved both chemically and electrochemically. It has been established by SEC that this reduction is a *pseudo*-first order process and the structural rearrangement takes place during the first electron-transfer step [188].

Polyhedral rearrangement is driven by the need of maintaining a correspondence between electron count and geometry of the metal framework. It allows a (quasi)reversible redox process in electron precise clusters, that otherwise would undergo irreversible redox events. It must be remarked that, more often, redox active MMCCs display variations of some M-M distances upon reduction or oxidation. From one side, this allows a less strict correlation between electron count and cluster geometry, since the same cluster may exist with the same structure of the metal core and a different number of CVE. On the other side, population/depopulation of bonding/anti-bonding MOs results in the weakening or strengthening of some M-M bonds. Depending on the fact that the MOs involved in the redox process are localized or delocalized, the variations may occur on a few specific M-M bonds or may involve more M-M bonds. Delocalization should be favored with increasing MMCC nuclearity and, at some point, the effect on M-M distances should be negligible. On the opposite side, if the MO involved in the redox process is more localized on a single M-M bond, the redox process could lead to a considerable loosening or even breaking of such bond.

4.1.1. Computational studies on structural changes induced by redox reactions on MMCCs

The key point is how to prove experimentally the occurrence of such structural variations. Indeed, in most cases, the SC-XRD structure of a single MMCC is available and then, its redox activity proved by electrochemistry and SEC. In these cases, a theoretical approach is possible [189], based on the computational simulation of the structures of the MMCCs obtained by adding/removing electrons to/from the SC-XRD structure of the starting MMCC. This approach may be applied to all redox active MMCCs but of course is a theoretical and not an experimental proof. Low root-mean-square deviations (RMSD) between DFT-optimized structures of MMCCs having different global charges could suggest reversible or quasi-reversible electrochemical behavior, but this outcome should be supported by other computed values, such as the Gibbs energy variations related to the dissociation/association of a carbonyl ligand, or to the formation of new bond with a solvent molecule. For instance, the RMSD between the structures of $[Ru_6C(CO)_{15}]^{4-}$ and its oxidation product $[Ru_6C(CO)_{15}]^{2-}$ computed at CPCM/PBEh-3c level resulted quite low (0.453 Å) [105], but the meaningfully negative Gibbs energy variation for the reaction between $[Ru_6C(CO)_{15}]^{2-}$ and acetonitrile (-25.3 kcal mol^{-1}) was in line with the experimental

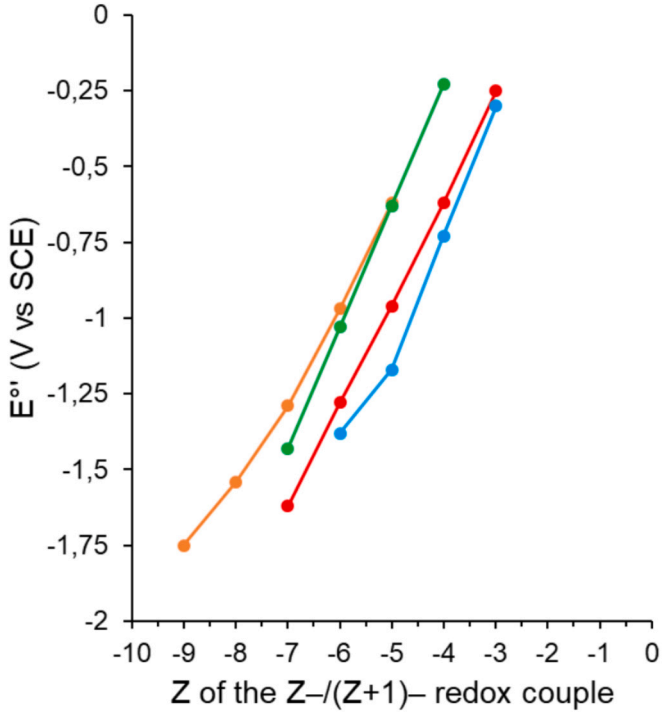

Fig. 25. Linear trend of Z-plots of the formal redox potentials ($E^{\circ\prime}$ *vs.* SCE) of the couples of clusters $[HNi_{38}Pt_6(CO)_{48}]^{5-}$ (red) and $[HNi_{35}Pt_9(CO)_{48}]^{5-}$ (blue), $[Ni_{38}Pt_6(CO)_{48}]^{6-}$ (orange) and $[Ni_{35}Pt_9(CO)_{48}]^{6-}$ (green), formally related by partial Ni/Pt replacement.

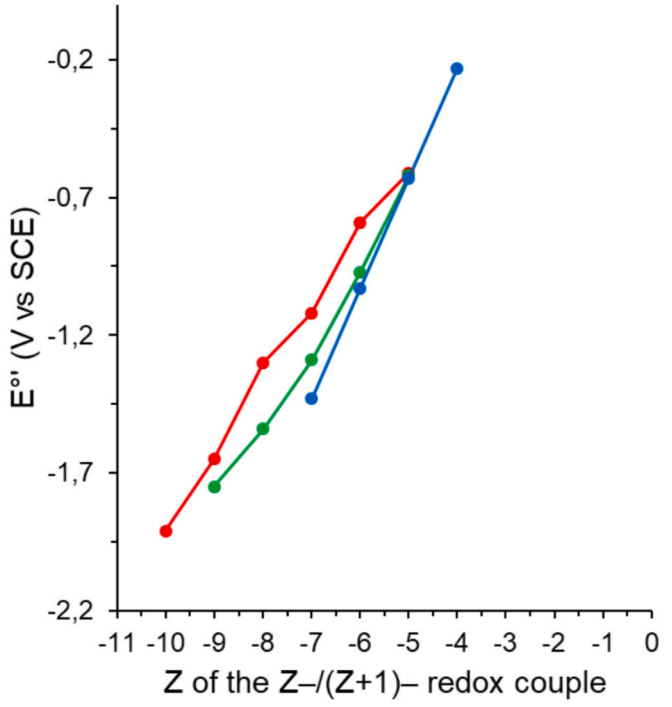

Fig. 26. Linear trend of Z-plots of the formal redox potentials ($E^{\circ\prime}$ *vs.* SCE) of the clusters $[Ni_{38}Pt_6(CO)_{48}]^{6-}$ (green), $[Ni_{35}Pt_9(CO)_{48}]^{6-}$ (blue) and $[Ni_{37-x}Pd_{7+x}(CO)_{48}]^{6-}$ (x = 0.69) (red) formally related by partial Ni/Pt/Pd replacement.

observation of $[Ru_6C(CO)_{15}(CH_3CN)]^{2-}$. A similar result was obtained considering the analogous iron derivatives simulated with the CPCM/r^{2}SCAN-3c method [106], and the formal displacement of the

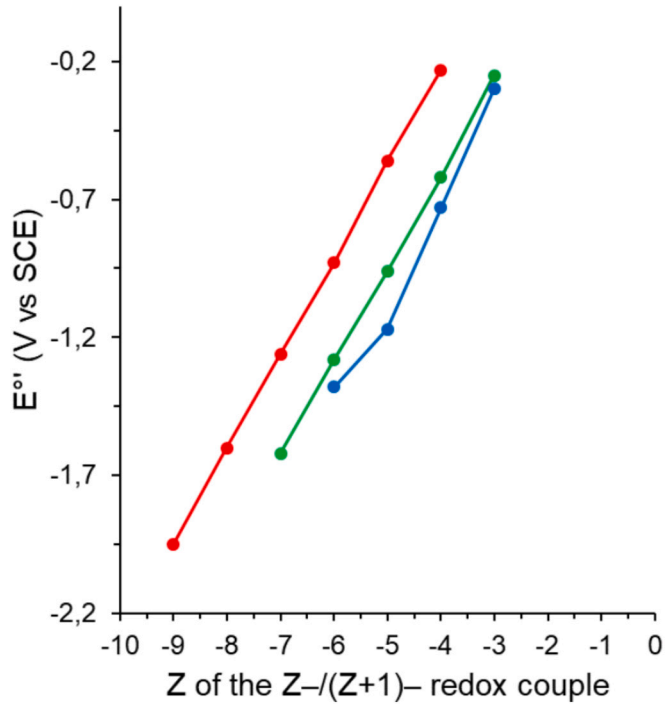

Fig. 27. Linear trend of Z-plots of the formal redox potentials ($E^{\circ\prime}$ *vs.* SCE) of the clusters $[HNi_{38}Pt_6(CO)_{48}]^{5-}$ (green), $[HNi_{35}Pt_9(CO)_{48}]^{5-}$ (blue) and $[HNi_{37-x}Pd_{7+x}(CO)_{48}]^{5-}$ (x = 0.53) (red) formally related by partial Ni/Pt/Pd replacement.

coordinated CH_3CN molecule by CO was justified from a thermodynamic point of view.

The simulated IR spectra can provide a correlation between experimental and computed data. When high nuclearity clusters are investigated, common DFT-based methods in combination with double- or triple-ζ quality basis sets can be computationally expensive. An acceptable modelling of the structure of these species can be obtained using recent semi-empirical approaches, such as the GFN2-xTB method [190,191]. For instance, the RMSD between experimental and computed structures of $[Pt_{27}(CO)_{31}]^{4-}$ was 0.485 Å using GFN2-xTB and 0.520 Å with PBEh-3c [83].

The variations of electron density, potential energy density and other related quantities at (3,−1) BCPs indicate which bonds enforce or weaken on varying the number of electrons in MMCCs [192]. As an example, the comparison of the $\{Ru_6C\}$ cores of $[Ru_6C(CO)_{15}]^{4-}$ and $[Ru_6C(CO)_{15}]^{2-}$ indicated a slight weakening of the Ru-carbide bonds for the less reduced species. In some cases, the extension of the analysis to ring and cage critical points can provide further useful data [193]. When unpaired electrons are present, information about the changes in the electronic structure of the cluster caused by redox processes can be also obtained from the spin density plots. For instance, $[Rh_{16}Au_6(CO)_{36}]^{5-}$ and $[Rh_{16}Au_6(CO)_{36}]^{7-}$, derived from the one-electron oxidation and reduction of $[Rh_{16}Au_6(CO)_{36}]^{6-}$, maintained the approximate D_{4h} symmetry of the $\{Au_6Rh_{16}\}$ core, but the spin density resulted less symmetric, mainly localized on the central $\{Au_6\}$ fragment and on two mutually *trans* $\{Rh_4Au_2\}$ octahedra in the oxidized species and on two mutually *cis* $\{Rh_4Au_2\}$ octahedra in the reduced cluster (Fig. 33) [155]. Before studying the electronic features of paramagnetic species, the preliminary comparison of the energy values among electronic structures with different multiplicity is highly suggested. For instance, the doublet electronic configuration of $[Rh_{12}In(CO)_{28}]^{2-}$ resulted more stable than the quartet and sextet configurations by about 42.3 and 93.2 kcal mol^{-1} [104].

Among the most important limits of DFT calculations, it must be stressed that the commonly used exchange-correlation DFT functionals

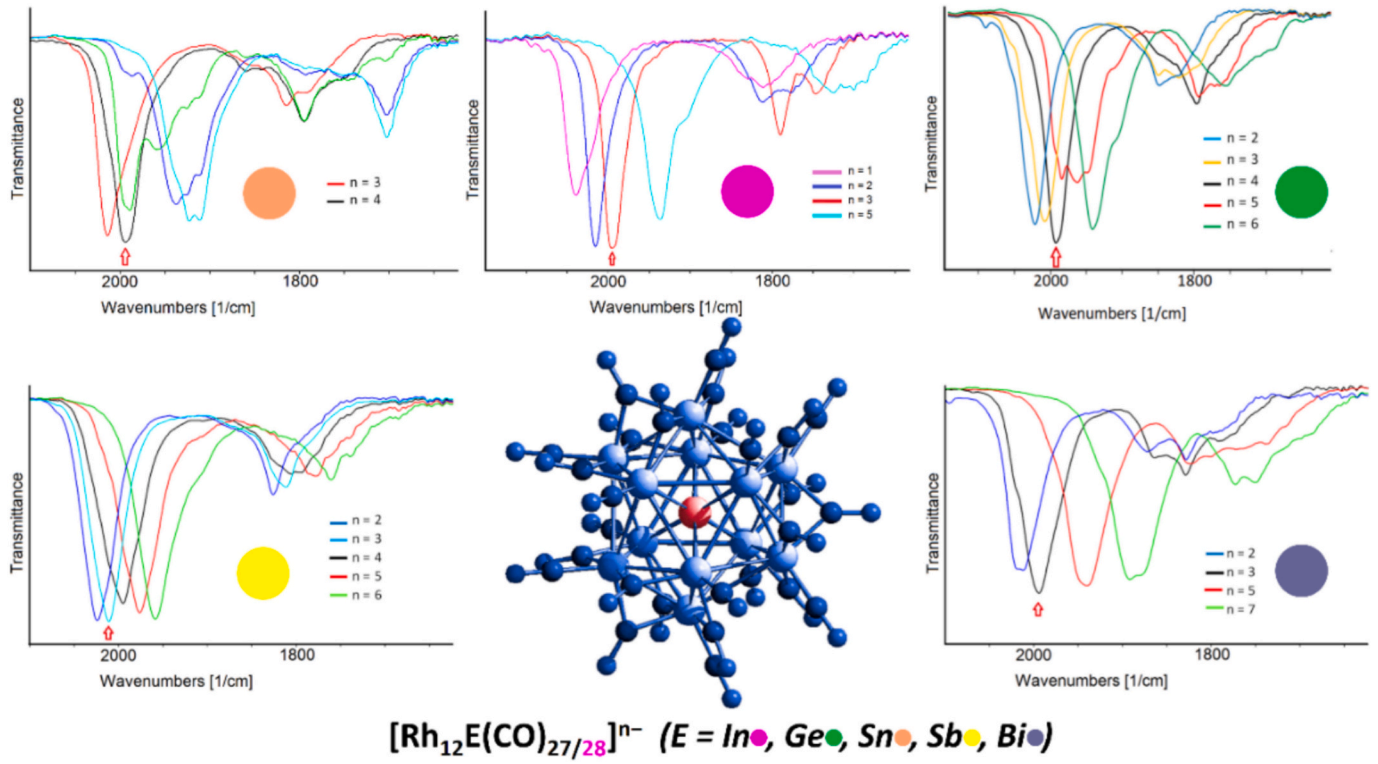

Fig. 28. Multivalence behavior of the $[Rh_{12}E(CO)_{27/28}]^{n-}$ family of clusters (n = 3 when E = In, Sb, Bi; n = 4 when E = Ge, Sn) as obtained by spectroelectrochemical experiments. Adapted from Ref. [104], with permission from The Royal Society of Chemistry.

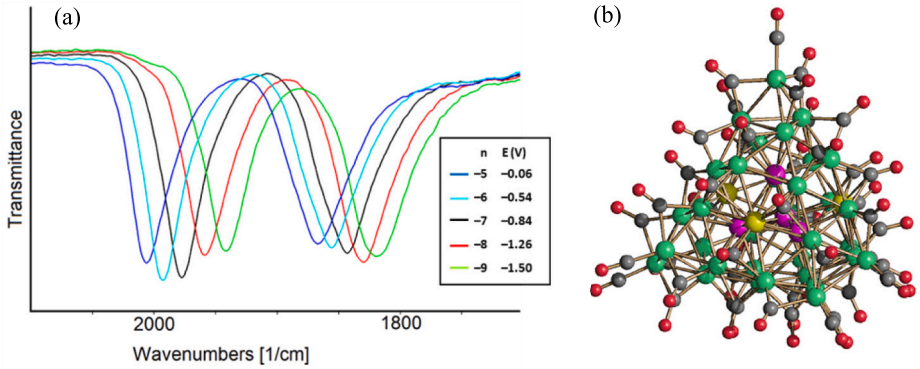

Fig. 29. (a) Selected IR spectra of $[Ni_{36-x}Pd_{5+x}(CO)_{46}]^{6-}$ (x = 0.41) as a function of the cluster charge n and potential E (V, *vs* Ag pseudo reference electrode) in CH_3CN containing 0.1 mol dm^{-3} $[N^nBu_4][PF_6]$. The absorptions of the solvent and supporting electrolyte have been subtracted. (b) Molecular structure of $[Ni_{36-x}Pd_{5+x}(CO)_{46}]^{6-}$ (x = 0.41) (green, Ni; purple, Pt, yellow, Ni/Pd ≈ 53:47; grey, C; red, O). Adapted with permission from Ref. [71]. Copyright 2021 American Chemical Society.

do not respect the Koopmans' theorem, thus there is no straightforward correlation between the Kohn-Sham frontier orbitals and the ionization potential and electron affinity of a MMCC [194]. Such a point must be considered when attempts of comparison between electrochemical outcomes and DFT-computed quantities are carried out. It is worth noting that the redox potential derives from the small difference between two very large quantities, the total energies of two oxidation states, with a strong contribution from the solvation of the species. Changes in the solvation sphere related to the oxidation or reduction of the species are of difficult prediction and can strongly affect the final redox potential [195–197] Finally, the energy comparison between closed- and open-shell systems, typical of one-electron transfers, deserves particular attention. The closed-shell compounds are usually simulated with a restricted DFT approach, while the open-shell molecules with unrestricted DFT calculations. Among the possible sources of error, the spin contamination in the unrestricted calculations influences the final energy of the species and can lead to wrong predictions of the redox potentials [198,199].

4.1.2. Experimental evidence of structural changes induced by redox reactions on MMCCs

To experimentally prove that some M-M bond distances change upon a redox process, two or more differently charged MMCCs obtained by redox reactions must be isolated and structurally characterized by SC-XRD. This poses serious limitations, since often oxidized or reduced MMCCs are stable in the timescale of electrochemistry and SEC, but not sufficiently stable for chemical isolation and crystallization. As shown above, the experimental evidence of the t-CO/μ-CO rearrangement is more straightforward, since it is based on IR spectroscopy, often obtained directly in an electrochemical OTTLE cell. Nonetheless, there are

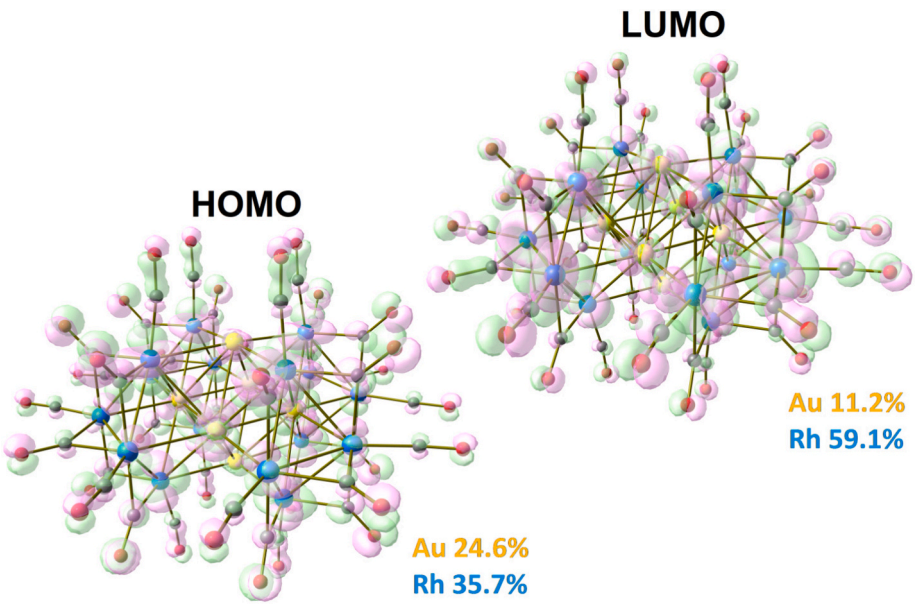

Fig. 30. DFT-optimized structure of $[Rh_{16}Au_6(CO)_{36}]^{6-}$ with HOMO and LUMO plotted (green and pink tones, surface isovalue = 0.03 a.u.) and selected Hirshfeld percentages. Color map: Rh, blue; Au, yellow; C, grey; O, red. Adapted from Ref. [155] with permission from Wiley.

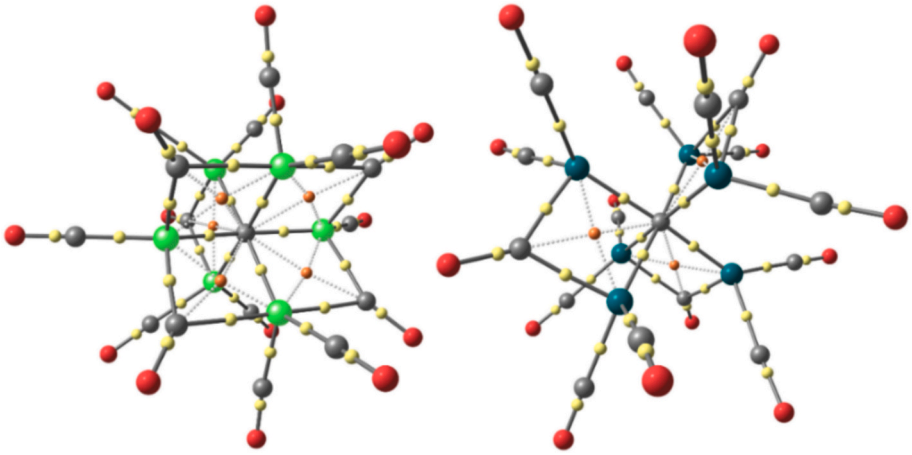

Fig. 31. DFT-optimized structures of $[M_6C(CO)_{15}]^{4-}$ clusters (M = Fe, Ru) with (3,−1) BCPs and (3,+1) RCPs (ring critical points) represented with small yellow and orange spheres, respectively. Color map: Fe, light green; Ru, dark green; C, grey; O, red.

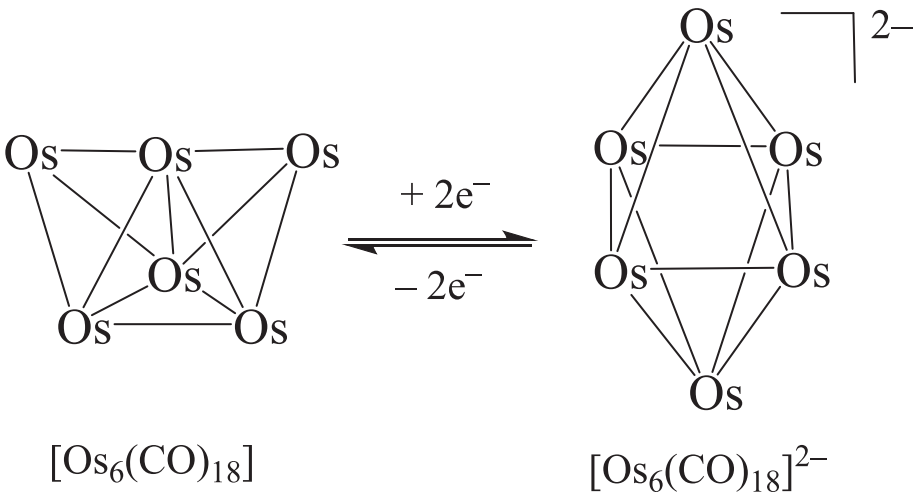

Fig. 32. Reversible polyhedral rearrangement upon reduction of $[Os_6(CO)_{18}]$ to $[Os_6(CO)_{18}]^{2-}$ (CO ligands have been omitted for clarity).

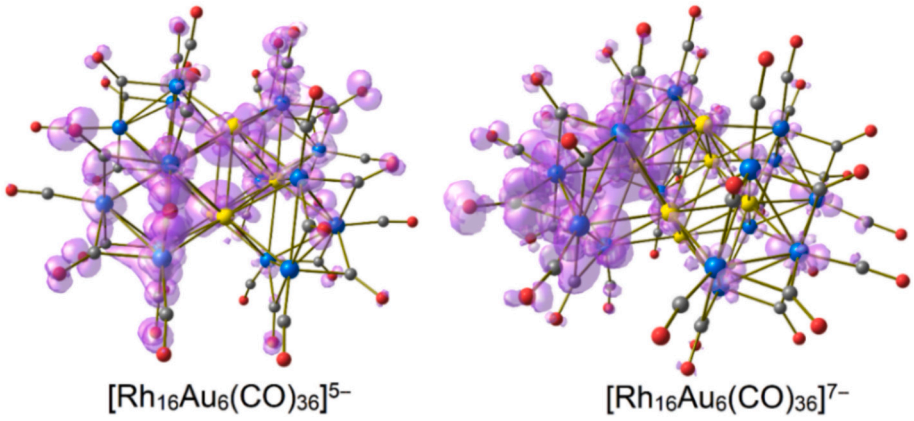

Fig. 33. DFT-optimized structures of $[Rh_{16}Au_6(CO)_{36}]^{5-}$ and $[Rh_{16}Au_6(CO)_{36}]^{7-}$ with spin density plots (violet tones, surface isovalue = 0.001 a.u.). Color map: Rh, blue; Au, yellow; C, grey; O, red. Adapted from Ref. [155] with permission from Wiley.

some noticeable examples where two or more redox related MMCCs have been structurally characterized by SC-XRD.

The cases of $[Fe_3Pt_3(CO)_{15}]^{n-}$ (n = 0–2) [127,128] and $[Ag_{13}Fe_8(CO)_{32}]^{n-}$ (n = 3–5) [141,171] have been presented in Section 3.1 (Figs. 9 and 11). In the former case, the Pt-Pt bonds are sensibly shortened after each oxidation step, suggesting a slight anti-bonding character of HOMO with respect to the three Pt atoms [127,128,200]. In the case of $[Ag_{13}Fe_8(CO)_{32}]^{n-}$ (n = 3–5), the Ag-Ag distances tend to decrease, and the Ag-Fe ones tend to increase with the addition of electrons, even if the changes are very small and close to the experimental uncertainty. Thus, some care must be taken, but this might suggest that the LUMO of the cluster is bonding with respect to the Ag-cuboctahedron and antibonding with respect to the Ag-Fe interactions [50].

A further noticeable example is represented by $[Fe_6Ni_6N_2(CO)_{24}]^{2-}$, whose metal cage consists of a face-sharing trioctahedron based on an *abab* staking of four triangles, two external Fe_3 and two internal Ni_3 [142]. The two nitrides are located on the two external Fe_3Ni_3 octahedra, whereas the inner Ni_6 octahedron is empty. The CV of $[Fe_6Ni_6N_2(CO)_{24}]^{2-}$ displays two reductions and one oxidation, all chemically and electrochemically reversible. The three $[Fe_6Ni_6N_2(CO)_{24}]^{n-}$ (n = 2–4) anions have been characterized by SC-XRD, revealing very similar structures. The Fe-Fe and Fe-Ni bond distances are almost identical in the three species (Fig. 34), whereas the Ni-Ni distances, especially the Ni-$Ni_{(inter\text{-triangle})}$ ones, monotonically increase with the increase of the number of valence electrons. This suggests that the electrons are added to the central Ni_6 octahedron and populate an antibonding orbital [50].

The species $[Co_8Pt_4C_2(CO)_{24}]^{2-}$ is isostructural to $[Fe_6Ni_6N_2(CO)_{24}]^{2-}$, with the four Pt atoms disordered over the inner octahedron [153]. It displays two reductions and one oxidation processes displaying features of chemical reversibility. The oxidized monoanion $[Co_8Pt_4C_2(CO)_{24}]^{-}$ has been isolated and characterized by SC-XRD, ^{13}C NMR and ESR spectroscopy. The bonding parameters of $[Co_8Pt_4C_2(CO)_{24}]^{2-}$ and $[Co_8Pt_4C_2(CO)_{24}]^{-}$ are almost identical, but a slight elongation of the Co-$Pt_{(inner\ noncentered\ octahedron)}$ distances suggests that the fragment involved in the electron transfer process is the inner octahedron.

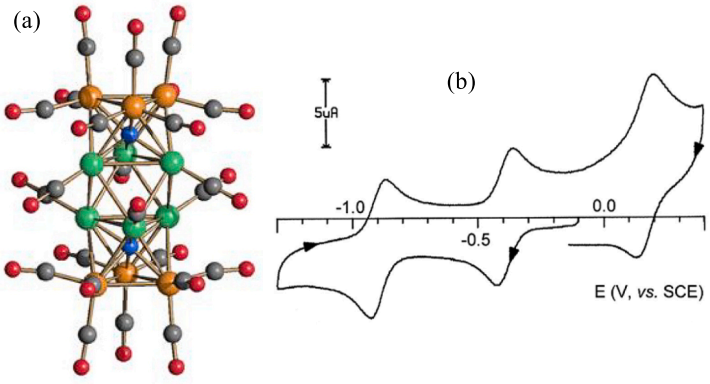

Complex	Fe-Ni	Fe-Fe	Ni-$Ni_{intra\text{-}triangle}$	Ni-$Ni_{inter\text{-}triangle}$
$[Fe_6Ni_6N_2(CO)_{24}]^{2-}$	2.63	2.61	2.79	2.62
$[Fe_6Ni_6N_2(CO)_{24}]^{3-}$	2.63	2.62	2.80	2.65
$[Fe_6Ni_6N_2(CO)_{24}]^{4-}$	2.63	2.62	2.81	2.72

Fig. 34. (a) Molecular structure of $[Fe_6Ni_6N_2(CO)_{24}]^{3-}$ (green, Ni; orange, Fe; blue, N; red, O; grey, C). (b) CV of $[Fe_6Ni_6N_2(CO)_{24}]^{2-}$ recorded at a Pt electrode on CH_3CN solution with $[N^nBu_4][ClO_4]$ at 0.5 V s^{-1}. The table reports the average bond lengths (Å) of $[Fe_6Ni_6N_2(CO)_{24}]^{n-}$ (n = 2–4). Adapted from Ref. [142] with permission from Elsevier.

Both the dicarbide clusters $[Co_{13}C_2(CO)_{24}]^{4-}$ [134] and $[Co_{11}C_2(CO)_{23}]^{2-}$ [133] display a rich electrochemistry and, interestingly, they have been used recently as efficient electrocatalysts for the hydrogen evolution reaction (HER) [56,57]. The $[Co_{13}C_2(CO)_{24}]^{4-}$ tetra-anion displays one oxidation and two reduction processes, all having features of chemical and electrochemical reversibility, and involving one electron each. The SC-XRD structures of $[Co_{13}C_2(CO)_{24}]^{4-}$ and $[Co_{13}C_2(CO)_{24}]^{3-}$ have been determined, and all the bonding parameters concerning the $Co_{13}C_2$ cage are identical within experimental error.

The CV of $[Co_{11}C_2(CO)_{23}]^{2-}$ displays two reversible processes, that is, one oxidation and one reduction (Fig. 35). Both $[Co_{11}C_2(CO)_{23}]^{2-}$ and $[Co_{11}C_2(CO)_{23}]^{-}$ have been structurally characterized by SC-XRD, and their common $Co_{11}C_2$ cage is based on two Co_6C octahedra sharing a common vertex and presenting three further inter-octahedra bonds. Ideally, such $Co_{11}C_2$ cage should display 27 Co-Co bonds (12 per each octahedron, 3 inter-octahedra) and should possess 148 CVE [86 × 2 (Oh) – 18 (vertex) – 2 × 3 (Oh-Oh bonds)]. Both $[Co_{11}C_2(CO)_{23}]^{2-}$ and $[Co_{11}C_2(CO)_{23}]^{-}$ are electron rich, possessing 155 and 154 CVE, respectively. This causes the loosening of some Co-Co bonds within the octahedral units. Indeed, $[Co_{11}C_2(CO)_{23}]^{-}$ contains 25 Co-Co bonds [2.459(3)–2.933(3) Å] and two weaker Co-Co contacts [3.058(7) and 3.249(3) Å], whereas $[Co_{11}C_2(CO)_{23}]^{2-}$ contains 23 Co-Co bonds [2.4532(16)–2.8301(15) Å] and four weaker Co-Co contacts [3.066(3), 3.138(4), 3.238(2), and 3.324(2) Å]. Also, the stereochemistry of the CO ligands is slightly different, since $[Co_{11}C_2(CO)_{23}]^{-}$ displays 13 t-CO and 10 μ-CO ligands, whereas $[Co_{11}C_2(CO)_{23}]^{2-}$ displays 14 t-CO and 9 μ-CO ligands. In this case, the addition of one electron transforms one μ-CO into a t-CO in contrast to what expected, and it is probably because also the Co-Co bonding significantly changes.

As reported in Section 3.3, $[Pt_{26}(CO)_{32}]^{2-}$ displays a very rich electrochemistry, and both the di-anion and mono-anion have been structurally characterized [166,174]. The SC-XRD of $[Pt_{26}(CO)_{32}]^{2-}$ and $[Pt_{26}(CO)_{32}]^{-}$ are almost superimposable, both concerning the metal cage and CO stereochemistry. It is likely that the addition/removal of a single electron on this large MMCC does not cause any significant structural change, or the changes are too small compared to the experimental precision of the SC-XRD analysis.

Heterometallic $[Fe_4Au(CO)_{16}]^{-}$ exists in solution as an equilibrium between $[Au\{\eta^2\text{-}Fe_2(CO)_8\}_2]^{-}$ and $[Au\{\eta^2\text{-}Fe_2(CO)_8\}\{\eta^2\text{-}Fe_2(CO)_6(\mu\text{-}CO)_2\}]^{-}$, being the unbridged species the major one [129]. In both cases, the central Au atom adopts a square-planar coordination, being bonded to two $Fe_2(CO)_8$ units. Its CV displays two reversible one-electron reductions at −0.68 and −0.89 V, and both the dianion and trianion have been characterized by IR SEC (Fig. 36). They may be also chemically generated, by reduction of $[Fe_4Au(CO)_{16}]^{-}$ in THF solution at −70 °C using one or two equivalents of $Na/C_{10}H_8$. IR spectroscopy clearly indicates the presence of bridging carbonyls in both the dianion and trianion. The structure of the trianion has been determined by SC-XRD, showing a tri-coordinated Au cluster with formula $[Au\{\eta^1\text{-}Fe_2(CO)_8\}\{\eta^2\text{-}Fe_2(CO)_6(\mu\text{-}CO)_2\}]^{3-}$. Based on IR spectroscopy, the radical dianion may be formulated as $[Au\{\eta^2\text{-}Fe_2(CO)_8\}\{\eta^2\text{-}Fe_2(CO)_6(\mu\text{-}CO)_2\}]^{2-}$. In this case, the addition of the first electron favors μ-CO coordination, whereas the second electron causes the breaking of one Fe-Au bond. The reduction processes have been investigated also by DFT methods, suggesting that the reduction of $[Au\{\eta^2\text{-}Fe_2(CO)_8\}_2]^{-}$ to $[Au\{\eta^2\text{-}Fe_2(CO)_8\}\{\eta^2\text{-}Fe_2(CO)_6(\mu\text{-}CO)_2\}]^{2-}$ is accompanied by a slight elongation of the Au-Fe and Fe-Fe bonds, together with the stereochemical change of two carbonyls from terminal to edge bridging mode, as observed by IR spectroscopy. The addition of a second electron further elongates one

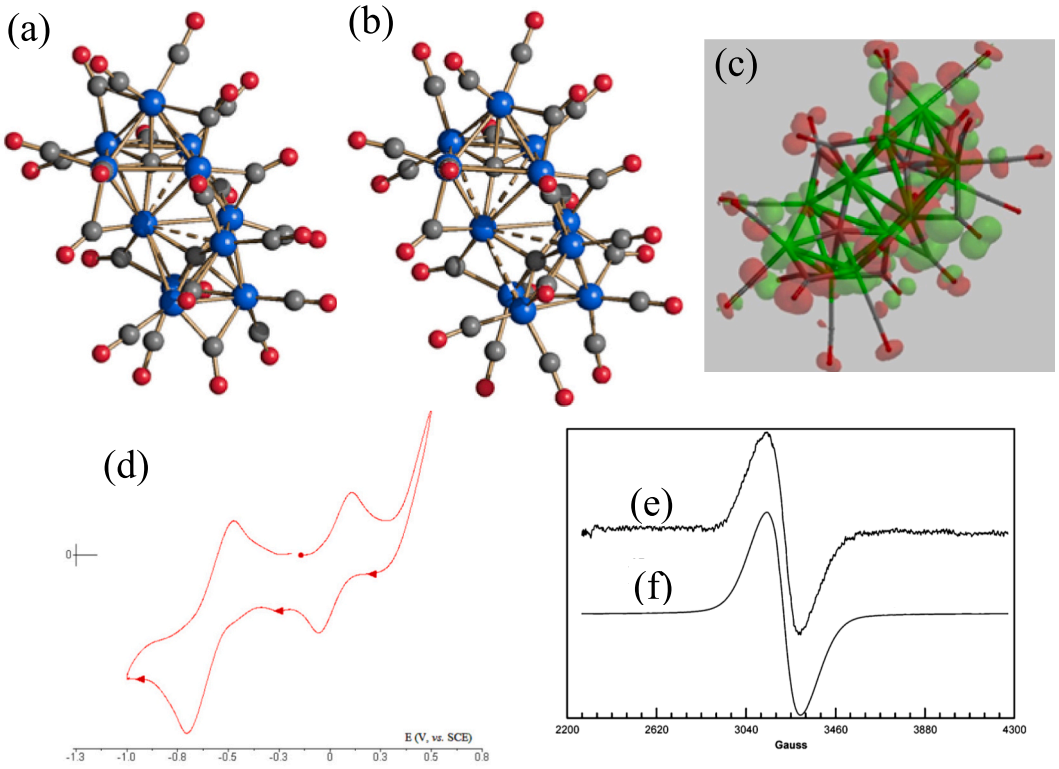

Fig. 35. Molecular structures of (a) $[Co_{11}C_2(CO)_{23}]^{-}$ and (b) $[Co_{11}C_2(CO)_{23}]^{2-}$ (blue, Co; red, O; grey, C). Co-Co contacts ≤ 3.02 Å are represented as full lines, those in the range 3.02–3.35 Å as fragmented lines. (c) DFT calculated spin density surface (0.002 electron/au^3) of $[Co_{11}C_2(CO)_{23}]^{2-}$ (red, negative spin density; green, positive spin density). (d) CV recorded at an Au electrode in THF of $[Co_{11}C_2(CO)_{23}]^{2-}$ (2.0×10^{-3} M). $[N^nBu_4][BF_4]$ (0.1 M) supporting electrolyte. Scan rate 0.1 V s^{-1}. X band EPR spectrum of $[Co_{11}C_2(CO)_{23}]^{2-}$ in CH_2Cl_2 solution registered at 193 K: (e) experimental and (f) simulation. Adapted with permission from Ref. [133]. Copyright 2014 American Chemical Society.

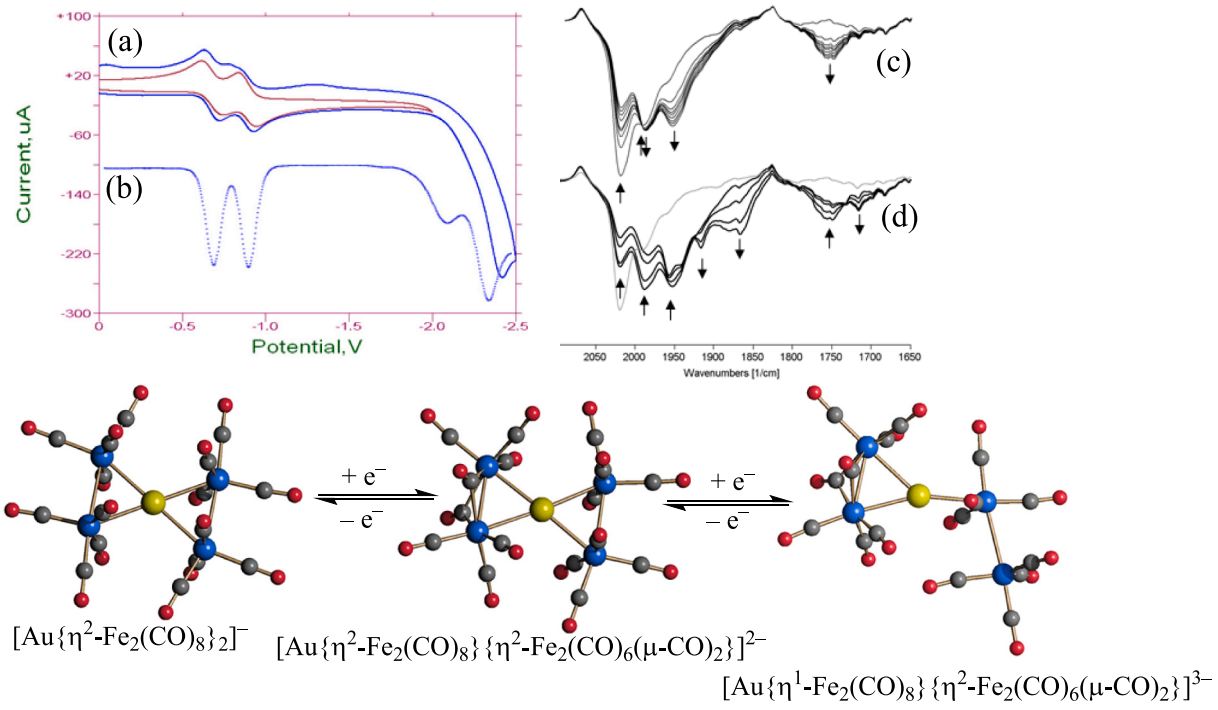

Fig. 36. (a) CV and (b) OSWV of a solution 3.8×10^{-4} M of $[Fe_4Au(CO)_{16}]^-$ in THF/$[N^nBu_4][PF_6]$ 0.2 M. Scan rate 0.2 V s^{-1}. IR-SEC during the stepwise overall reduction of $[Fe_4Au(CO)_{16}]^-$ (0.9×10^{-3} M) in CH_3CN solution $[N^nBu_4][PF_6]$ (0.10 M) as supporting electrolyte: (c) first reduction, E_w from −0.40 V to −0.60 V, *vs.* pseudo-Ag electrode; (d) second reduction, E_w from −0.60 V to −0.75 V, *vs.* pseudo-Ag electrode; grey line, initial spectrum. The structures of $[Au\{\eta^2\text{-}Fe_2(CO)_8\}_2]^-$ and $[Au\{\eta^1\text{-}Fe_2(CO)_8\}\{\eta^2\text{-}Fe_2(CO)_6(\mu\text{-}CO)_2\}]^{3-}$ have been determined by SC-XRD, whereas $[Au\{\eta^2\text{-}Fe_2(CO)_8\}\{\eta^2\text{-}Fe_2(CO)_6(\mu\text{-}CO)_2\}]^{2-}$ has been optimized by DFT. Adapted with permission from Ref. [129]. Copyright 2022 American Chemical Society.

Au-Fe bond up to its breakage.

4.2. *Effects of structural changes on the redox properties of MMCCs*

The effect of M/M' substitution on the redox properties of heterometallic MMCCs has been discussed in Section 3.4. Similarly, modulation of the redox properties may be obtained by changing the nature of main group elements within MMCCs. This is well exemplified by the series of E-centered icosahedral clusters $[Rh_{12}Ge(CO)_{27}]^{4-}$, $[Rh_{12}Sn(CO)_{27}]^{4-}$, $[Rh_{12}Sb(CO)_{27}]^{3-}$, $[Rh_{12}Bi(CO)_{27}]^{3-}$, and $[Rh_{12}In(CO)_{28}]^{3-}$, all possessing 170 CVE [104,180,181]. A part $[Rh_{12}Sn(CO)_{27}]^{4-}$ which displays a single reversible oxidation process, all the other species show by CV or IR-SEC three or four reversible redox processes. In the case of $[Rh_{12}Ge(CO)_{27}]^{4-}$ and $[Rh_{12}Sb(CO)_{27}]^{3-}$, all the four redox processes are mono-electronic. Conversely, in the case of $[Rh_{12}Bi(CO)_{27}]^{3-}$ and $[Rh_{12}In(CO)_{28}]^{3-}$, two redox processes are mono-electronic, whereas the most cathodic event involves two electrons. Further details can be found in Section 3.5.

The redox properties of MMCCs may be also modulated by replacement of some carbonyls with other ligands, such as phosphines. The

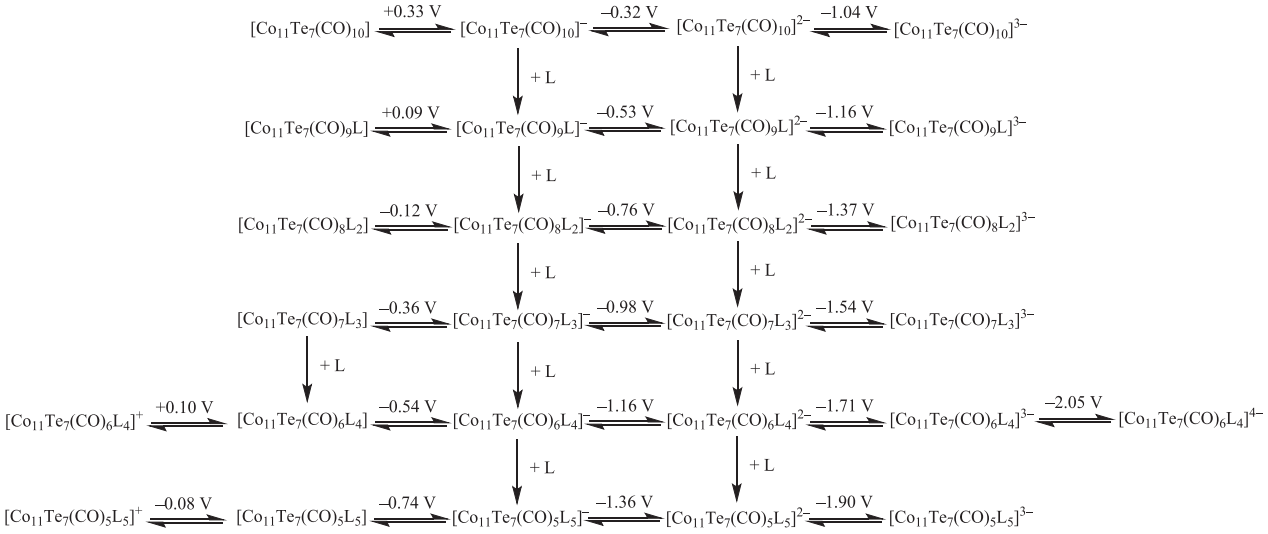

Fig. 37. Global presentation of the reaction of $[Co_{11}Te_7(CO)_{10}]^-$ with L = PMe_2Ph. Verified redox couples (horizontal) and CO substitution steps (vertical). Adapted from Ref. [150] with permission from Wiley.

substitution of one CO with a more σ-basic ligand should shift the redox processes to more negative potentials and favor less negatively charged species [184,201]. As a matter of fact, the heteroleptic clusters $[Co_{11}Te_7(CO)_{10-x}(PMe_2Ph)_x]$ (x = 0–5) are all multivalent and display three reversible mono-electronic reductions [150]. Each reduction step is shifted of 0.12–0.24 V towards more negative potentials upon each CO/PMe_2Ph substitution (Fig. 37). Moreover, in the case of the compounds containing 4–5 PMe_2Ph ligands, also one reversible oxidation process is observed, affording the $[Co_{11}Te_7(CO)_6(PMe_2Ph)_4]^+$ and $[Co_{11}Te_7(CO)_5(PMe_2Ph)_5]^+$ cations. SC-XRD structures have been determined in the case of $[Co_{11}Te_7(CO)_{10}]^{2-}$, $[Co_{11}Te_7(CO)_{10}]^-$, and $[Co_{11}Te_7(CO)_5(PMe_2Ph)_5]$.

As outlined in Section 3.4, protonation/deprotonation reactions represent a very straightforward and simple way for tuning the redox properties of MMCCs. Protonation of anionic MMCCs may be accomplished using stoichiometric amounts of strong acids, such as $HBF_4{\cdot}Et_2O$, CF_3SO_3H, H_2SO_4 or CF_3COOH. The process may be reversed using strong bases, such as NaOH, $[N^nBu_4][OH]$, MeONa, or Bu^tOK [30,71,154,158,160–162,202–211]. In some cases, protonation/deprotonation may spontaneously occur by changing the solvent: more polar solvents favor deprotonation, whereas less polar solvents favor protonation (Fig. 38). From one side, acid/base reactions represent a very simple way to tune the redox properties of MMCCs. On the other side, the occurrence of acid-base equilibria, in conjunction with redox activity, may complicate the electrochemical investigation of MMCCs. Indeed, the charge of a hydride multivalent MMCCs may be changed both by acid-base and redox reactions. At the same time, electrochemistry may considerably help the study of multivalent polyhydride MMCCs.

As previously discussed (Section 3.4), the same redox change occurs at more negative potential in the hydride species compared to the non-hydride MMCC. The same applies by increasing the number of hydrides in polyhydride MMCCs, even though sometimes the presence of two or more hydride ligands may be detrimental to the redox aptitude of the cluster. For instance, $[H_2Ni_{38}Pt_6(CO)_{48}]^{4-}$ displays a limited number of (not well defined) reversible redox processes, compared to $[HNi_{38}Pt_6(CO)_{48}]^{5-}$ and $[Ni_{38}Pt_6(CO)_{48}]^{6-}$, probably because of reductive H_2 elimination in polyhydride species. At this regard, it is noteworthy that some MMCCs have been found to be active as electrocatalysts for the hydrogen evolution reaction (HER) [25,53–58,201]. The proposed mechanisms involve a combination of two proton transfer (PT) and two electron transfer (ET) processes, with formation of hydride MMCCs as intermediates and final release of H_2 (see Section 5).

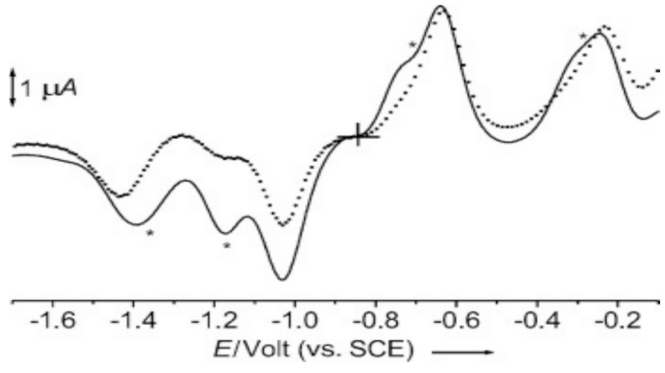

Fig. 38. OSWV profiles of an approximately 1:1 mixture of $[Ni_{35}Pt_9(CO)_{48}]^{6-}$ and $[HNi_{35}Pt_9(CO)_{48}]^{5-}$ (7×10^{-4} mol dm^{-3}) recorded under the following conditions: a) immediately after its dissolution in DMF solution (—), b) after 90 min (----). Scan rate 0.1 Vs^{-1}, supporting electrolyte $[N^nBu_4][PF_6]$ (0.2 mol dm^{-3}), Au WE. $[HNi_{35}Pt_9(CO)_{48}]^{5-}$ spontaneously deprotonates to $[Ni_{35}Pt_9(CO)_{48}]^{6-}$ with time in DMF. Adapted from Ref. [161] with permission from Wiley.

4.2.1. *Electrochemistry as an indirect tool to circumstantiate the hydride nature of larger MMCCs*

The different redox properties of MMCCs related by protonation/deprotonation reactions have been revealed to be a useful indirect method for the assessment of the polyhydride nature of larger MMCCs. As mentioned above, often anionic MMCCs behave as Bronsted bases and may be protonated by acids resulting in hydride MMCCs. It must be remarked that, due to the π-character of CO, hydride ligands of MMCCs behave more like H^+ than H^-. Thus, polyhydride MMCCs may be viewed as polyprotic acids which can be reversibly deprotonated/protonated upon reactions with Bronsted bases and acids [30]. The decrease of one unit of the negative charge of the cluster upon each protonation step can be easily monitored by the shift to higher wavenumbers of its ν_{CO} bands by IR spectroscopy. The crucial point is that the same effect may be obtained upon one-electron oxidation. Indeed, H^+ may act toward the MMCC as a protonating agent or as an oxidizer via the H^+/H_2 couple. So, how to discriminate between protonation and oxidation of MMCCs by acids? In the case of low to mid nuclearity MMCCs, the answer can be easily found by means of ^1H NMR spectroscopy, which can be used for the direct detection of hydride ligands. However, as thoroughly discussed in the literature, the direct detection of hydrides in MMCCs by ^1H NMR fails above a nuclearity of *ca.* 30 metal atoms [212]. Similarly, the direct location of hydride ligands by SC-XRD become increasingly difficult as MMCC nuclearity increases, and it becomes almost impossible in the case of larger MMCCs. Very few hydride MMCCs have been characterized by single crystal neutron diffraction, and the examples are limited to low or mid nuclearity MMCCs [30].

In all these cases, electrochemistry may be used to indirectly determine if the two differently charged MMCCs are related by protonation/deprotonation or oxidation/reduction. Indeed, in the latter case, they should display the same electrochemical properties, whereas in the former case they should present different electrochemical behavior. Some examples have been presented in Section 3.4, and further examples may be found in Tables 2–4 and in the cited literature. A few further representative cases will be briefly discussed herein.

The two anions $[Ni_{25}(C_2)_4(CO)_{32}]^{4-}$ and $[HNi_{25}(C_2)_4(CO)_{32}]^{3-}$ can be easily interconverted by acid-base reactions, and both have been structurally characterized by SC-XRD (Fig. 39) [157]. Their molecular structures are almost superimposable, even though it has not been possible to locate the hydride ligand by SC-XRD. Also, all the attempts to detect the hydride of $[HNi_{25}(C_2)_4(CO)_{32}]^{3-}$ by ^1H NMR failed, and the reader can find details on this problem in the literature. CV, OSWV and IR-SEC studies indicate that, in CH_3CN solution, $[HNi_{25}(C_2)_4(CO)_{32}]^{3-}$ undergoes three reversible reductions, whereas $[Ni_{25}(C_2)_4(CO)_{32}]^{4-}$ displays one oxidation and four reductions with features of reversibility. The fact that the two species obtained upon protonation/deprotonation display different electrochemical behavior, clearly suggests that they are different chemical species, in accord with the hydride nature of $[HNi_{25}(C_2)_4(CO)_{32}]^{3-}$. Moreover, $[HNi_{25}(C_2)_4(CO)_{32}]^{3-}$ spontaneously deprotonates to $[Ni_{25}(C_2)_4(CO)_{32}]^{4-}$ by standing in DMF or CH_3CN solution, as demonstrated by time-dependent OSWV (Fig. 39).

Similar considerations apply to the isostructural (as determined by SC-XRD) $[HNi_{31}P_4(CO)_{39}]^{5-}$ and $[H_2Ni_{31}P_4(CO)_{39}]^{4-}$ (hydrides have not been located by SC-RD nor detected by ^1H NMR) (Fig. 40 and Table 7) [102]. $[HNi_{31}P_4(CO)_{39}]^{5-}$ displays two oxidations and six reductions all reversible in the timescale of IR-SEC, allowing the spectroscopic characterization of the species $[HNi_{31}P_4(CO)_{39}]^{n-}$ (n = 3–11). Conversely, $[H_2Ni_{31}P_4(CO)_{39}]^{4-}$ shows only three reversible reductions leading to $[H_2Ni_{31}P_4(CO)_{39}]^{n-}$ (n = 4–7); its poorer electrochemistry compared to $[HNi_{31}P_4(CO)_{39}]^{5-}$ agrees with the di-hydride nature of the tetra-anion generated by protonation of the penta-anion as discussed above. As a further proof of the poly-hydride nature of these clusters, $[HNi_{31}P_4(CO)_{39}]^{5-}$ may be further deprotonated by NaOH to $[Ni_{31}P_4(CO)_{39}]^{6-}$, whereas the hepta-anion $[Ni_{31}P_4(CO)_{39}]^{7-}$ can be generated only by addition of Na/naphthalene to the hexa-anion. In this way, also the number of hydride ligands has been indirectly assessed.

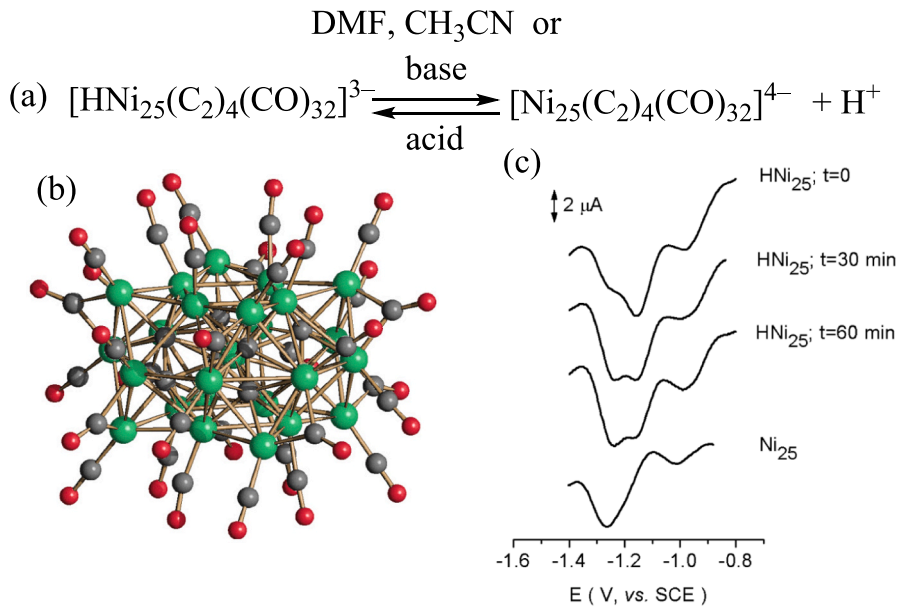

Fig. 39. (a) Protonation/deprotonation equilibrium involving $[HNi_{25}(C_2)_4(CO)_{32}]^{3-}$ and $[Ni_{25}(C_2)_4(CO)_{32}]^{4-}$. (b) Molecular structure of $[Ni_{25}(C_2)_4(CO)_{32}]^{4-}$ (green. Ni; red, O; grey, C). (c) Time evolution of the Osteryoung square wave voltammogram of a 0.9×10^{-5} M solution of $[HNi_{25}(C_2)_4(CO)_{32}]^{3-}$ in CH_3CN compared with that of a 7×10^{-5} M solution of $[Ni_{25}(C_2)_4(CO)_{32}]^{4-}$ (bottom), showing gradual deprotonation. GC WE and $[N^nBu_4][PF_6]$ (0.1 mol dm^{-3}) as supporting electrolyte. Adapted from Ref. [157], with permission from The Royal Society of Chemistry.

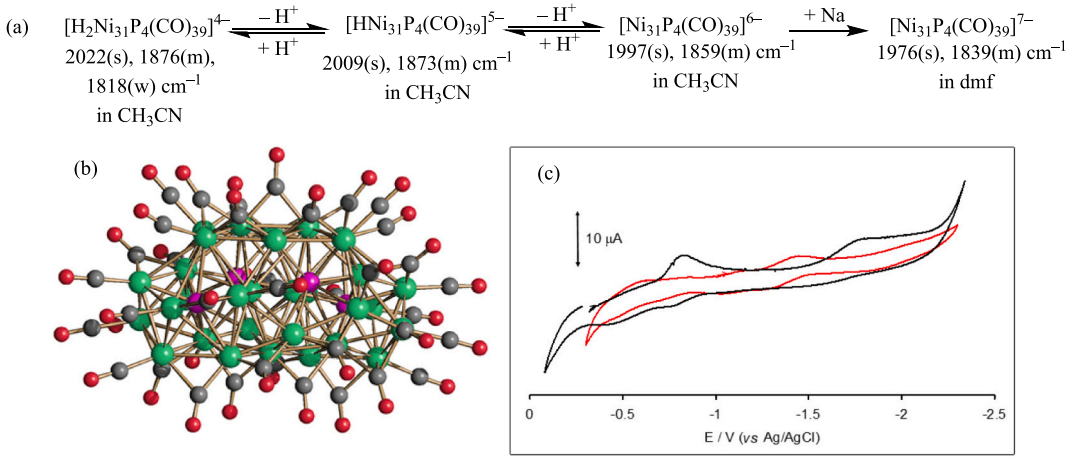

Fig. 40. (a) Protonation/deprotonation equilibria involving the $[H_{6-n}Ni_{31}P_4(CO)_{39}]^{n-}$ (n = 4, 5, 6) clusters and chemical reduction of $[Ni_{31}P_4(CO)_{39}]^{6-}$ to $[Ni_{31}P_4(CO)_{39}]^{7-}$. (b) Molecular structure of $[H_{6-n}Ni_{31}P_4(CO)_{39}]^{n-}$ (n = 4, 5) (Ni, green; P, purple; C, grey; O, red). (c) CVs recorded at a Pt electrode in CH_3CN solution of $[H_2Ni_{31}P_4(CO)_{39}]^{4-}$ (black) and $[HNi_{31}P_4(CO)_{39}]^{5-}$ (red). $[N^nBu_4][PF_6]$ (0.1 mol dm^{-3}) as the supporting electrolyte. Scan rate 0.1 V s^{-1}. Adapted with permission from Ref. [102]. Copyright 2018 American Chemical Society.

$[H_4Rh_{22}(CO)_{35}]^{4-}$ and $[H_3Rh_{22}(CO)_{35}]^{5-}$ can be distinguished based on their CV and DPV profiles (Fig. 41) [154]. In this case, the presence of the hydride ligands in both species has been supported also by ^1H NMR spectroscopy, which clearly indicates that a mixture of both species is present in CH_3CN, whereas pure $[H_3Rh_{22}(CO)_{35}]^{5-}$ is present in more polar solvents such as DMF and DMSO. The equilibrium between $[H_4Rh_{22}(CO)_{35}]^{4-}$ and $[H_3Rh_{22}(CO)_{35}]^{5-}$ can be evidenced also by electrochemistry, since the signals of both species have been detected by CV and DPV in CH_3CN, whereas the electrochemical profile of only $[H_3Rh_{22}(CO)_{35}]^{5-}$ is present in DMF. Even though such acid-base equilibria might complicate the electrochemical study of hydride MMCCs, suitable combinations of electrochemical and SEC techniques can be very helpful to study them. This point is nicely exemplified also by the series of clusters $[H_{6-n}Ni_{30}C_4(CO)_{30}(CdCl)_2]^{n-}$ (n = 4–6) [79]. CV and DPV analyses in CH_3CN are complicated because of an equilibrium between $[H_2Ni_{30}C_4(CO)_{30}(CdCl)_2]^{4-}$ and $[HNi_{30}C_4(CO)_{30}(CdCl)_2]^{5-}$, whereas pure $[Ni_{30}C_4(CO)_{30}(CdCl)_2]^{6-}$ has been detected in DMF.

A further point of interest may be found in the electrochemical studies of the acid-base related species $[H_2Co_{15}Pd_9C_3(CO)_{38}]^-$, $[HCo_{15}Pd_9C_3(CO)_{38}]^{2-}$, and $[Co_{15}Pd_9C_3(CO)_{38}]^{3-}$, whose structures have been determined by SC-XRD [135]. The CV profiles of these three MMCCs display only reversible oxidation processes (Fig. 42), which are different for the three of them. This clearly indicates that they are different chemical species, and the conversion of the mono-anion into the di- and tri-anion, as well as the conversion of the di-anion into the tri-anion, may be accomplished only by deprotonation and not by reduction. Moreover, SQUID studies of $[HCo_{15}Pd_9C_3(CO)_{38}]^{2-}$ show that it is an even-electron species with two unpaired electrons, corroborating the presence of a single H-atom.

$[H_{6-n}Ni_{30}C_4(CO)_{34}\{Cu(CH_3CN)\}_2]^{n-}$ (n = 4–6) represent a further

Table 7
IR stretching frequencies (cm^{-1}) of terminal (ν^t_{CO}) and bridging (ν^b_{CO}) carbonyl groups for $[HNi_{31}P_4(CO)_{39}]^{n-}$ and $[H_2Ni_{31}P_4(CO)_{39}]^{n-}$ in CH_3CN as a function of the cluster charge *n* and of the potential *E* as measured by IR-SEC. The starting $[HNi_{31}P_4(CO)_{39}]^{5-}$ and $[H_2Ni_{31}P_4(CO)_{39}]^{4-}$ are evidenced in bold.

Cluster charge *n*	ν^t_{CO}	ν^b_{CO}	*E*
$[HNi_{31}P_4(CO)_{39}]^{n-}$			
3	2040	1892	−0.30 V
4	2022	1882	−0.60 V
5	**2009**	**1873**	**−1.0 V**
6	1995	1864	−1.41 V
7	1982	1852	−1.68V
8	1965	1841	−1.92 V
9	1951	1825	−2.19 V
10	1939	1809	−2.34V
11	1928	1799	−2.55 V
$[H_2Ni_{31}P_4(CO)_{39}]^{n-}$			
4	**2022**	**1876, 1818**	**−0.40 V**
5	2011	1864, 1806	−0.70 V
6	1994	1847, 1780	−1.15 V
7	1980	1841	−1.75 V

family of poly-hydride MMCCs which display different CV profiles, and whose inter-conversion may be fully accomplished only by means of acid-base reactions [163]. To conclude this Section, the CV profiles of $[Ni_{36}Co_8C_8(CO)_{48}]^{6-}$ and $[HNi_{36}Co_8C_8(CO)_{48}]^{5-}$ display only irreversible redox processes and, thus, their interconversion can be achieved only by acid-base reactions [213]. This is apparently a trivial conclusion, but it may be applied to other non-redox active MMCCs to prove their hydride nature.

5. Further chemical information obtained by electrochemical studies of MMCCs

In the previous Sections, several examples of MMCCs displaying reversible or quasi-reversible electrochemical processes have been presented. It has been shown that, in these cases, electrochemical and SEC studies may give information on the electronic and structural features of MMCCs. This Section will focus on MMCCs with irreversible redox processes or presenting reversible (or quasi-reversible) electrochemical processes followed by further chemical reactions. In these cases, electrochemistry and SEC studies may give information on the chemical properties of these MMCCs and, in some favorable cases, on the products of chemical reactions.

A general chemical information that can be obtained from electrochemical studies, independently of the fact that the processes are reversible or irreversible, is the potential at which the cluster may be oxidized or reduced. This information can help the selection of a suitable oxidizing or reducing agent to chemically modify the cluster [76,214–216].

The irreversible oxidation or reduction of a MMCC may lead to different events, such as fragmentation, condensation, structural rearrangement, elimination/addition of ligands, decomposition. Reviews are available in the literature on the synthesis and chemical reactivity of MMCCs and, therefore, only a few examples combining chemical reactivity and electrochemical analyses will be presented herein [24–36].

Formally, two electrons may replace one CO ligand leaving the number of CVE unaltered. Indeed, in several instances, the two-electron reduction of a MMCC results in the increase of two units of its anionic charge and elimination of one CO ligand. For instance, controlled potential electrolysis of $[Rh_{12}C_2(CO)_{24}]^{2-}$ affords $[Rh_{12}C_2(CO)_{23}]^{4-}$ with retention of the $Rh_{12}C_2$ cage [46]. Similarly, $[FeIr_5(CO)_{16}]^-$ undergoes to an irreversible two-electron reduction (E_P = −1.27 V) affording

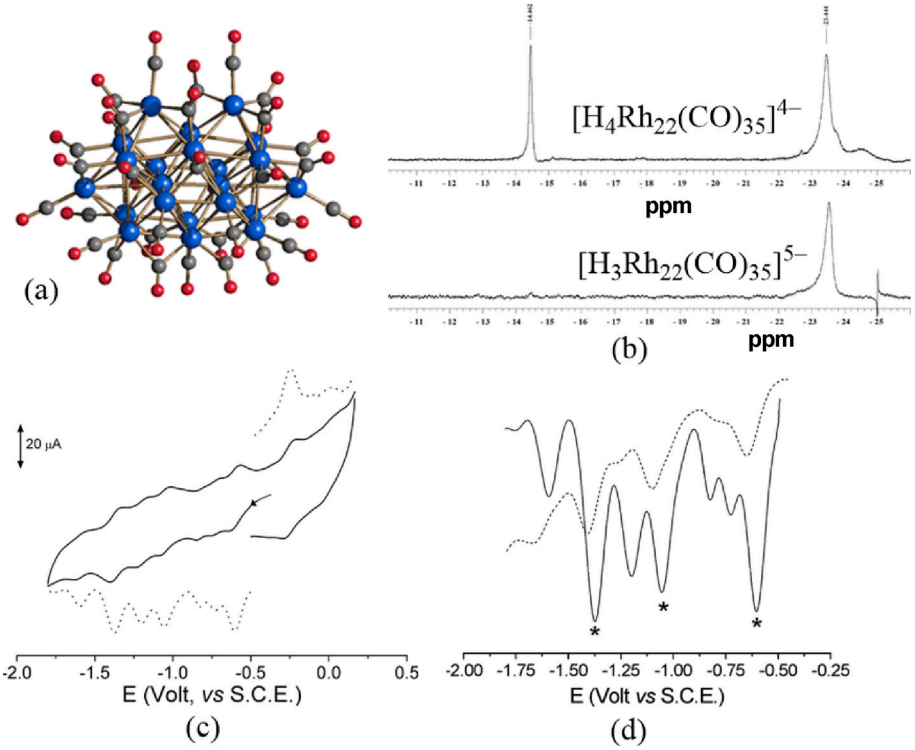

Fig. 41. (a) Molecular structure of $[H_{8-n}Rh_{22}(CO)_{35}]^{n-}$ (n = 4, 5) (blue, Rh; red, O; grey, C). Hydride ligands have not been located by SC-XRD. (b) ^1H NMR spectra of (upper trace) a mixture of $[H_4Rh_{22}(CO)_{35}]^{4-}$ (δ_H −14.5 ppm) and $[H_3Rh_{22}(CO)_{35}]^{5-}$ (δ_H −23.4 ppm) in CD_3CN, and (lower trace) $[H_3Rh_{22}(CO)_{35}]^{5-}$ in d_6-DMSO. (c) CV (full line) and DPV (dotted line) of a mixture of $[H_4Rh_{22}(CO)_{35}]^{4-}$ and $[H_3Rh_{22}(CO)_{35}]^{5-}$ in CH_3CN. (d) Comparison between the DPV profiles of the mixture of the two clusters in CH_3CN (full line) and pure $[H_3Rh_{22}(CO)_{35}]^{5-}$ in DMF (dotted line). Adapted with permission from Ref. [154] Copyright 2011 American Chemical Society.

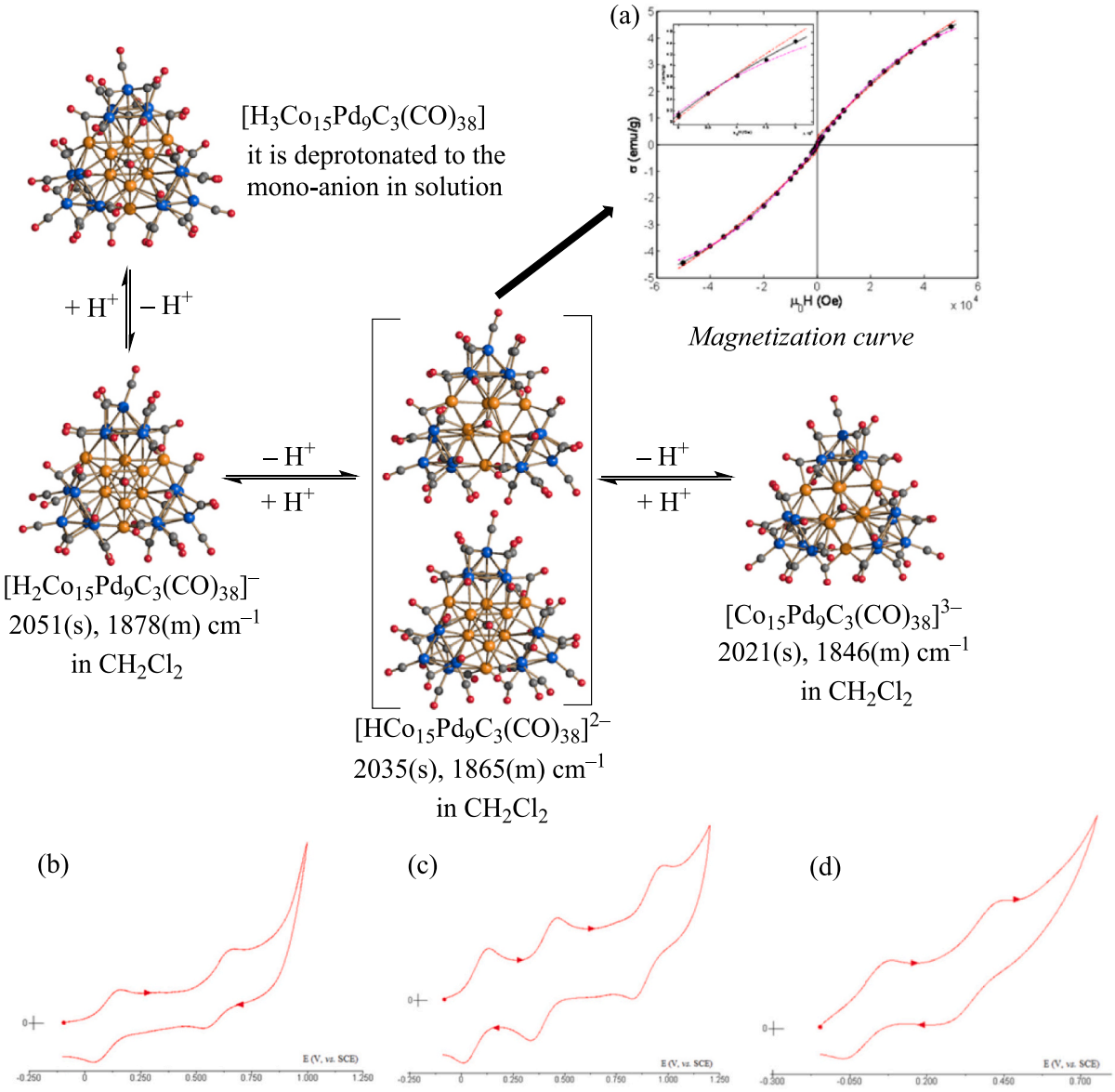

Fig. 42. Protonation/deprotonation reactions of $[H_{3-n}Co_{15}Pd_9C_3(CO)_{38}]^{n-}$ (n = 0–3) (orange, Pd; blue, Co; red, O; grey, C). Hydride ligands have not been located by SC-XRD. $[H_3Co_{15}Pd_9C_3(CO)_{38}]$ and $[H_2Co_{15}Pd_9C_3(CO)_{38}]^-$ display an Oh-Pd_9 core, whereas $[Co_{15}Pd_9C_3(CO)_{38}]^{3-}$ adopt a TP-Pd_9 structure (Oh = octahedron; TP = trigonal prism). Both isomers have been found in the case of $[HCo_{15}Pd_9C_3(CO)_{38}]^{2-}$. (a) Magnetization in function of field of $[NMe_3(CH_2Ph)]_2[HCo_{15}Pd_9C_3(CO)_{38}]\cdot C_6H_{14}$ as measured at 5 K (black dots). The data were fitted with the Brillouin function for different S values and Landé g-factor of free electron. Dashed lines are the best fits for S = 1/2 (red) and S = 3/2 (magenta). The black solid line represents the best-fitting curve from least-squares analysis for S = 1. Inset: zoom of the high field region. Cyclic voltammograms recorded at a glassy carbon electrode in CH_2Cl_2 of (b) $[H_2Co_{15}Pd_9C_3(CO)_{38}]^-$, (c) $[HCo_{15}Pd_9C_3(CO)_{38}]^{2-}$ and (d) $[Co_{15}Pd_9C_3(CO)_{38}]^{3-}$ (2.0×10^{-3} M). $[N^nBu_4][BF_4]$ (0.1 M) supporting electrolyte. Scan rate 0.2 V s^{-1}. Solvent discharge occurs at high potentials. Adapted from Ref. [135] with permission from The Royal Society of Chemistry.

$[FeIr_5(CO)_{15}]^{3-}$ (Fig. 43); both clusters display octahedral structures, in agreement with their electron count (86 CVE) [121].

From a chemical point of view, a two-electron reduction may be accomplished using Na/naphthalene (or similar reducing agents) or using NaOH in a polar solvent such as MeOH or DMSO. In the latter case, the OH^- ion attacks a CO ligand of the cluster resulting in its oxidation to CO_2 with concomitant two-electron reduction of the cluster. This approach has been often employed for synthetic purposes [217–219].

Considering the reverse process, a two-electron oxidation of a MMCC may favor the addition of a ligand. This represents an important synthetic route for the preparation of heteroleptic MMCCs. The use of both reduction and oxidation reactions for the preparation of new MMCCs is well represented by the $[M_6C(CO)_{16}]^{2-}$ and $[M_6C(CO)_{15}]^{4-}$ species (M = Fe, Ru), whose redox properties have been studied by electrochemical and computational methods (Sections 2.3 and 4.1.1) [105,106]. Indeed, $[M_6C(CO)_{15}]^{4-}$ may be obtained upon chemical or electrochemical reduction of $[M_6C(CO)_{16}]^{2-}$.

IR SEC and DFT investigation point out that the chemical and electrochemical oxidation of $[M_6C(CO)_{16}]^{4-}$ in CH_3CN, under N_2 or Ar atmosphere, is likely to proceed via unsaturated labile $[M_6C(CO)_{15}]^{2-}$ species. Due to stronger Ru-Ru bonds, the Ru species is sufficiently stable to add CH_3CN leading to $[Ru_6C(CO)_{15}(CH_3CN)]^{2-}$. Conversely, the Fe species rapidly decomposes forming some free CO, which can saturate the remaining dianion with formation of $[Fe_6C(CO)_{16}]^{2-}$. Performing the chemical oxidation of $[Fe_6C(CO)_{15}]^{4-}$ in the presence of suitable trapping agents (e.g., PTA, CO_3^{2-}, RS^-) it is possible to trap the

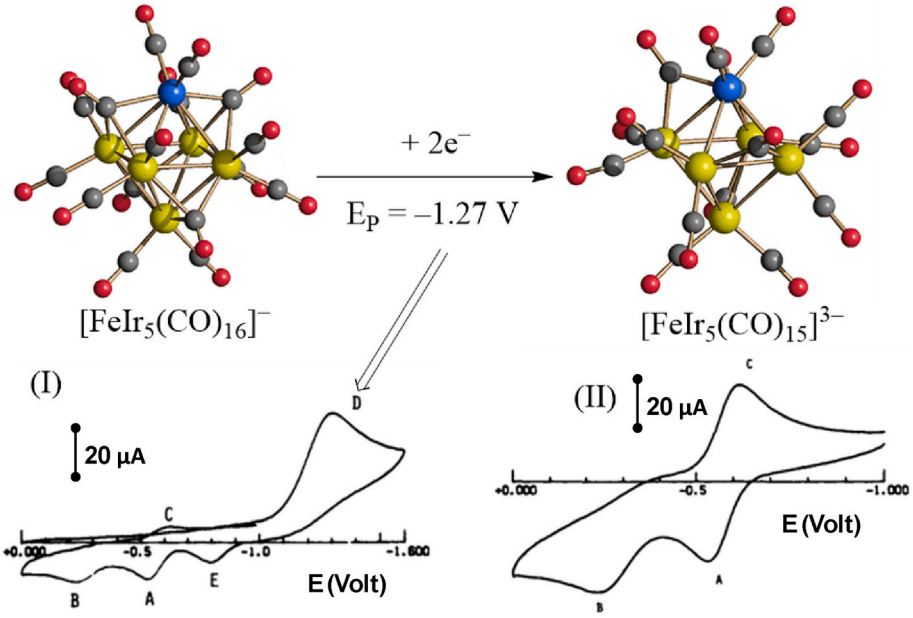

Fig. 43. The irreversible electrochemical reduction of $[FeIr_5(CO)_{16}]^-$ in CH_3CN affords $[FeIr_5(CO)_{15}]^{3-}$ (yellow, Ir; blue, Fe; red, O; grey, C). Cyclic voltammograms of (I) $[FeIr_5(CO)_{16}]^-$ and (II) $[FeIr_5(CO)_{15}]^{3-}$ (CH_3CN solution, Pt WE, $[NEt_4][ClO_4]$ supporting electrolyte, scan rate 0.2 V s^{-1}). Adapted with permission from ref. [121] Copyright 1991 American Chemical Society.

unsaturated species resulting in the formation of species such as $[Fe_6C(CO)_{15}(PTA)]^{2-}$, $[Fe_6C(CO)_{14}(CO_3)]^{4-}$ and $[Fe_6C(CO)_{14}(SR)]^{3-}$ [106,220].

As a further example, tetrahedral $[H_3Os_4(CO)_{12}]^-$ (60 CVE), in CH_3CN solution, undergoes a single-stepped two-electron oxidation at $E_p = +0.78$ V, which is apparently irreversible being coupled to the coordination of two CH_3CN molecules with formation of butterfly $[H_3Os_4(CO)_{12}(CH_3CN)_2]^+$ (62 CVE) (Fig. 44) [221]. The resulting $[H_3Os_4(CO)_{12}(CH_3CN)_2]^+$ is irreversibly reduced to $[H_3Os_4(CO)_{12}]^-$ at $E_p = -1.35$ V.

Several other examples have been reported in the literature where an electron transfer involving a MMCC is coupled to a chemical reaction. It is not possible here to describe all of them, but only a few representative examples will be presented.

The cluster $[Ni_{12}C(CO)_{18}]^{4-}$ was obtained by chemical reduction of $[Ni_9C(CO)_{17}]^{2-}$; it undergoes two oxidations and one reduction, reversible in the CV timescale [156]. The IR SEC investigation of the three processes showed that the products of the reduction and of the first oxidation, namely $[Ni_{12}C(CO)_{18}]^{5-}$ and $[Ni_{12}C(CO)_{18}]^{3-}$, respectively, are fairly stable clusters, while a fragmentation follows the second oxidation with formation of its precursor $[Ni_9C(CO)_{17}]^{2-}$.

As already said in Section 3.3, multivalent MMCCs usually display a greater number of reduction processes than oxidations. In several cases, the latter are followed by fragmentation reactions to give stable and known products that can be easily identified by their characteristic IR spectrum. Thus, two carbonyl bands at 2120 and 2063 cm^{-1} [222] demonstrated the formation of the mononuclear cationic $[Rh(CO)_2(CH_3CN)_2]^+$ by oxidation in the case of $[Rh_{16}Au_6(CO)_{36}]^{5-}$ [155] and $[Rh_{12}E(CO)_{27}]^{n-}$ (E = Sb or Ge) [180], while often the IR absorption of $Ni(CO)_4$ was found after oxidation of MMCCs containing Ni, as for example $[Ni_{11}P(CO)_{18}]^{3-}$, $[HNi_{31}P_4(CO)_{39}]^{5-}$ [102], or $[Ni_{29-x}Pd_{6+x}(CO)_{42}]^{6-}$ (x = 0.09) [80].

A peculiar case is represented by MMCCs that can be described as complexes composed of a central M^{n+} ion bonded to MMCC fragments. In these cases, the redox processes may be centered on the metal ion or on MMCC ligands. Moreover, the primary electron transfer may be followed by intra-molecular redox processes involving M^{n+} and the MMCC fragments.

The cluster $[\{Co_5C(CO)_{12}\}_2Au]^-$ is composed of two square-pyramidal $[Co_5C(CO)_{12}]^-$ anionic cluster ligands η^3-coordinated to an Au(I) center [82]. Its CV displays one oxidation and two reduction processes all with features of chemical reversibility and involving one electron each (Fig. 45). Thus, the four $[\{Co_5C(CO)_{12}\}_2Au]^{n-}$ (n = 0–3) species are stable in the timescale of CV, but partial decomposition is

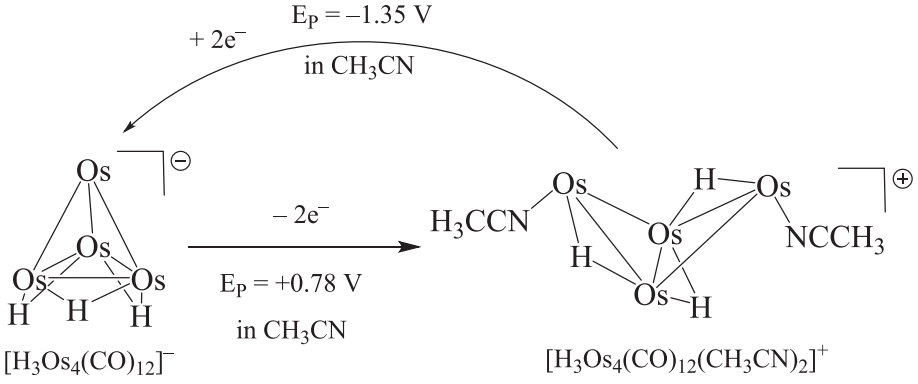

Fig. 44. The irreversible electrochemical oxidation of $[H_3Os_4(CO)_{12}]^-$ in CH_3CN affords $[H_3Os_4(CO)_{12}(CH_3CN)_2]^+$ (CO ligands have been omitted for clarity).

observed during IR-SEC experiments. Both LUMO and LUMO+1 are centered on the two $[Co_5C(CO)_{12}]^-$ fragments, which are reduced to $[Co_5C(CO)_{12}]^{2-}$ during the cathodic steps. The limited stability in the IR-SEC timescale of the reduced species is probably due to intramolecular redox reactions, which lead to Au(0) and $[Co_5C(CO)_{12}]^-$.

A similar behavior has been observed for $[\{Ni_6(CO)_{12}\}_2Au]^{3-}$ and $[\{Ni_6(CO)_{12}\}_2Cd_2Cl_3]^{3-}$, which are composed of two $[Ni_6(CO)_{12}]^{2-}$ units acting as ligands towards a central Au^+ and $[Cd_2(\mu\text{-}Cl)_3]^+$ unit, respectively [223]. Their CV profiles display an irreversible reduction ($E_p = -2.01$ and -1.52 V for $[\{Ni_6(CO)_{12}\}_2Au]^{3-}$ and $[\{Ni_6(CO)_{12}\}_2Cd_2Cl_3]^{3-}$, respectively), followed by a reversible two-electron reduction at $E^{\circ\prime} = -2.42$ V for both clusters (Fig. 46). The latter reversible two-electron process has been observed at the same $E^{\circ\prime}$ for $[Ni_6(CO)_{12}]^{2-}$. It is likely that the first irreversible reduction leads to the detachment of $[Ni_6(CO)_{12}]^{2-}$ from $[\{Ni_6(CO)_{12}\}_2Au]^{3-}$ and $[\{Ni_6(CO)_{12}\}_2Cd_2Cl_3]^{3-}$. This has been confirmed by IR-SEC experiments, which corroborate the formation of free $[Ni_6(CO)_{12}]^{2-}$ in correspondence of the first reduction. Similarly, electrochemical studies of $[Ni_9(CO)_{18}]^{2-}$ show that this is irreversibly reduced to $[Ni_6(CO)_{12}]^{2-}$.

Chemical reactions coupled with electron transfer processes are fundamental for electrocatalytic applications. Different MMCCs are active homogeneous electrocatalysts for reduction reactions as, for example, HER, and this topic has been recently reviewed [25,53–58,201,224–229]. Electrochemical studies (*e.g.*, CV, IR-SEC, controlled potential electrolysis) are very useful to optimize the experimental conditions, fine tuning the properties of the MMCC electrocatalyst, determining the kinetic parameters and the electrocatalytic mechanism. Overall, HER involves two PT and two ET processes, and adopts an ECEC or ECCE mechanism (Fig. 47). After ET1 and PT1, a monohydride MMCC intermediate is usually formed. For HER electrocatalysis, such monohydride undergoes ET2/PT2 (ECEC path) or PT2/ET2 (ECCE path) leading to a labile di-hydride that rapidly liberates H_2 restoring the catalytic cycle. Slowing down PT2 compared to PT1 can favor hydride-transfer (HT) from the monohydride MMCC intermediate to a substrate other than H^+. Indeed, following this strategy, it has been possible to extend MMCC electrocatalysis to CO_2 reduction (Fig. 48).

6. Conclusion and outlook

A survey of the electrochemical and SEC methods for the investigation of MMCCs has been herein reported. A major goal of any electrochemical study is to determine if a MMCC (or any other species) is redox active. This, in turn, sheds light on the electronic properties of the compound under investigation. Indeed, the redox aptitude of MMCCs increases with their nuclearity, even though *ad hoc* conditions may prompt redox activity also within smaller MMCCs. As a matter of fact, larger MMCCs are often multivalent and behave as electron-sinks, envisioning an incipient metallization of their metal cores.

Electrochemical and SEC studies unravel a subtle interplay between the electrochemical properties and the structural features of MMCCs. The multi-electron redox activity of MMCCs, often coupled with structural rearrangements or ligand dissociation, complicates the interpretation of electrochemical data. Radical anions may be transient and prone to rapid degradation or aggregation. Working at low temperatures, employing rapid scan rates, and combining electrochemical data with *in situ* spectroscopic monitoring is often necessary to capture and stabilize reactive intermediates. A multimethod approach, based on chemical, electrochemical, SEC, spectroscopic, structural and computational studies, is often necessary to fully understand the chemical and structural processes accompanying a redox event. At the same time, the redox properties of multivalent MMCCs may be fine-tuned by slight variations of their structures, such as protonation/deprotonation, ligand substitution, selective metal or hetero-atom replacement.

Overall, the electrochemical characterization of MMCCs reveals not only their redox potentials and stability domains but also the extent of electron delocalization and structural robustness, key features for their application in catalysis, electrocatalysis, molecular electronics, and nanomaterials.

As outlined throughout this review, several electrochemical techniques are currently available and can be effectively applied to the study of MMCCs. CV and IR-SEC are the most powerful ways to investigate reversible, quasi-reversible, or irreversible redox processes of MMCCs. These methods can be complemented by other electrochemical approaches (DPV, SWV, EIS) to gain deeper insights into the number of exchanged electrons, kinetic parameters of the electron transfer process, coupling with subsequent chemical reactions, and deconvolution of

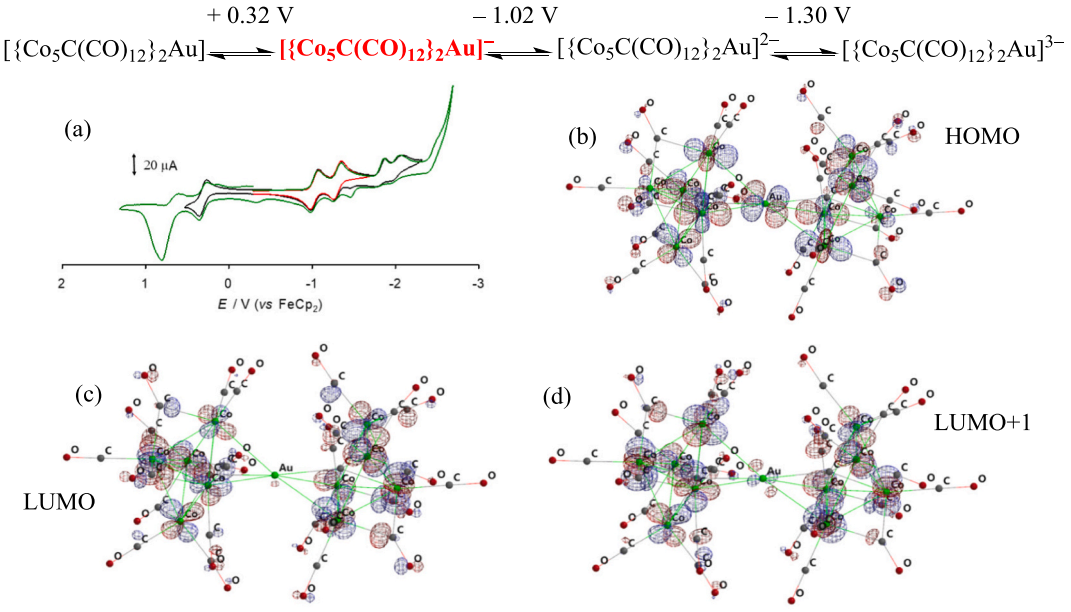

Fig. 45. Reversible electrochemical redox processes of $[\{Co_5C(CO)_{12}\}_2Au]^-$. (a) Cyclic voltammograms (recorded at a Pt electrode in a CH_2Cl_2 solution; $[N^nBu_4][PF_6]$ 0.2 mol dm^{-3} as supporting electrolyte; scan rate 0.1 V s^{-1}), (b) HOMO, (c) LUMO and (d) LUMO+1 (DFT EDF2 calculations, isovalue = 0.04 a.u) of $[\{Co_5C(CO)_{12}\}_2Au]^-$. Adapted from ref. [82] with permission from The Royal Society of Chemistry.

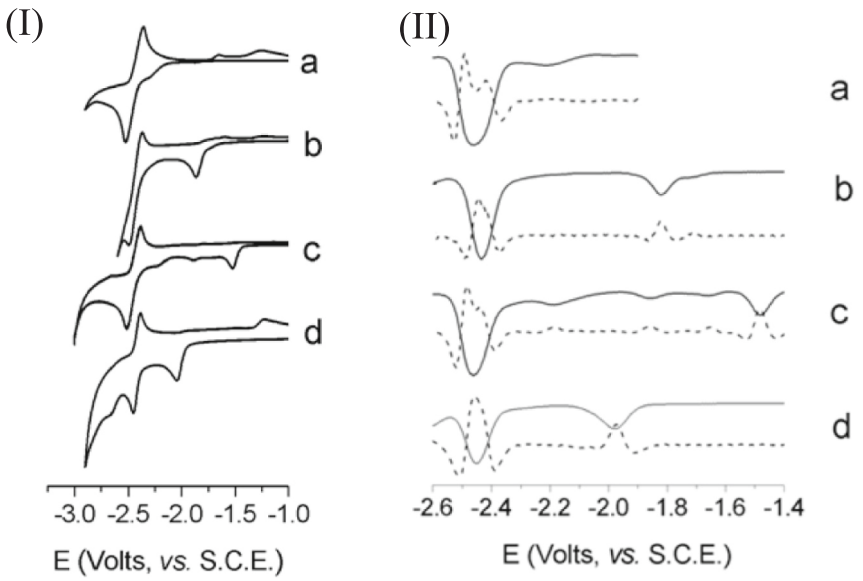

Fig. 46. (I) Cyclic voltammograms recorded at an Au electrode in THF solution of: (a) $[Ni_6(CO)_{12}]^{2-}$; (b) $[Ni_9(CO)_{18}]^{2-}$; (c) $\{Cd_2Cl_3[Ni_6(CO)_{12}]_2\}^{3-}$; (d) $[Ni_{12}Au(CO)_{24}]^{3-}$. Normalized currents of samples in mM concentration. $[N^nBu_4][PF_6]$ (0.2 M) supporting electrolyte. Scan rate 0.2 V s^{-1}. (II) Osteryoung square-wave voltammograms (full line) and its second derivative (dashed line) recorded at an Au electrode in a T solution of (a) $[Ni_6(CO)_{12}]^{2-}$; (b) $[Ni_9(CO)_{18}]^{2-}$; (c) $\{Cd_2Cl_3[Ni_6(CO)_{12}]_2\}^{3-}$; (d) $[Ni_{12}Au(CO)_{24}]^{3-}$. $[N^nBu_4][NPF_6]$ supporting electrolyte (0.2 M). Scan rates: 0.1 Vs^{-1}. Adapted with permission from Ref. [223] Copyright 2012 American Chemical Society.

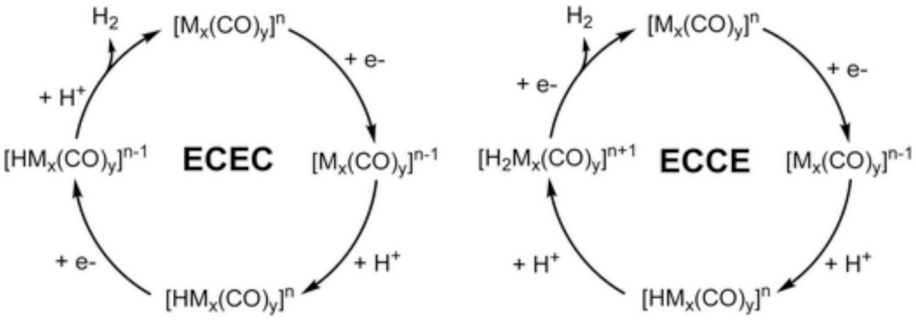

Fig. 47. Proposed ECEC and ECCE mechanisms for the electrocatalytic hydrogen-evolution reaction promoted by MCCs. Reproduced from ref. [25] with permission from The Royal Society of Chemistry.

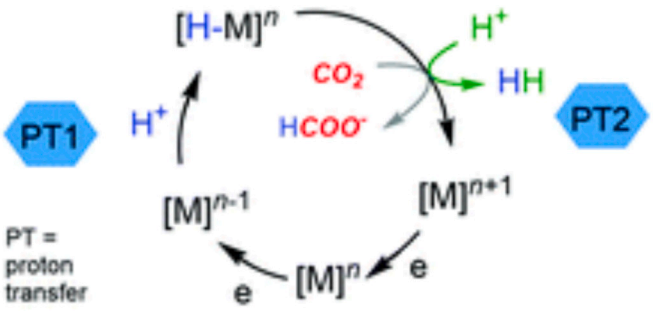

Fig. 48. Schematic showing the two possible reaction pathways for a metal hydride – which can (a) react with protons to form H_2 or (b) react with CO_2 to form formate. Reproduced from ref. [58] with permission from Wiley.

overlapping processes among other effects.

MMCCs possess highly complex structures which can be determined with atomic precision only by SC-XRD [24–37]. Once the structure of a MMCC has been determined by SC-XRD, electrochemical methods are particularly valuable, not only to study its redox properties, but also to get detailed information on the structures of the electrogenerated species. Indeed, because of the presence of CO ligands, IR-SEC allows real-time monitoring of structural (relative intensity of terminal/bridging ν_{CO} bands), and electronic (ν_{CO} shifts) changes associated with redox processes of MMCCs. Additional insight can be obtained from complementary *in situ* or *ex situ* spectroscopic techniques. In general, a multi-method approach, combining structural (SC-XRD), spectroscopic (IR, NMR, EPR, mass spectrometry), electrochemical and computational techniques, is required to fully investigate molecular nanoclusters such as MMCCs.

Low nuclearity MMCCs are often electron precise and show a direct relationship between structure and number of CVEs. Different electron counting rules have been developed (EAN, Wade's rules, PSEPT, TEC) which apply to different size-regimes and/or types of clusters [42,111–118]. However, their application becomes more difficult as MMCC nuclearity increases, and larger MMCCs are often multivalent and behave as electron sinks. These multivalent clusters exhibit from three to seven reversible electrochemical processes, meaning that the same molecular structure can exist in multiple oxidation states with distinct charges and CVE counts. In some smaller MMCCs, multivalence may arise from specific combinations of electronic, steric, and bonding

factors, although their redox activity remains less pronounced than in high-nuclearity systems.

Electrochemically generated oxidized or reduced MMCCs are often sufficiently stable to be observed not only within the timescale of CV but also during IR-SEC. Sometimes, they can be also chemically generated, isolated and spectroscopically characterized. In a few cases, it has been possible to structurally characterize by SC-XRD two or more MMCCs related by direct redox reactions.

Further information on the variation with nuclearity of the electronic status of multivalent MMCCs can be obtained from the Z-plots of the formal redox potential ($E^{\circ\prime}$). Mid-nuclearity clusters typically exhibit staircase-like Z-plots, whereas higher-nuclearity clusters display nearly linear ones. This difference suggests that mid-sized MMCCs possess well-separated frontier orbitals with energy gaps larger than the electron-pairing energy, while in larger MMCCs the spacing between consecutive orbitals approaches the pairing energy.

The average separation between the formal electrode potentials of consecutive redox couples of multivalent MMCC ($\Delta E^{\circ\prime}_{av}$) roughly decreases as MMCC nuclearity increases. Smaller MMCCs (6–10 metal atoms) exhibit $\Delta E^{\circ\prime}_{av} \approx 0.7$–$0.8$ V, whereas the largest investigated systems (38–44 metal atoms) show $\Delta E^{\circ\prime}_{av} \approx 0.2$–$0.3$ V. These values indicate a semiconducting nature of the largest MMCC cores. A further decrease in $\Delta E^{\circ\prime}_{av}$ with increasing nuclearity could signal the onset of metallic behavior, representing one of the major challenges for future synthesis and electrochemical exploration of MMCCs.

The redox properties of multivalent MMCCs may be tuned by selective M/M' replacement in heterometallic clusters, or upon substitution of a few carbonyls with other ligands. Such modifications can induce subtle shifts in $E^{\circ\prime}$ values and modulate the tendency toward oxidation or reduction. Often, protonation/deprotonation (acid/base) reactions offer a straightforward and reversible method to fine tune the redox behavior of MMCCs. Moreover, it has been shown that electrochemistry represents a powerful and effective approach to indirectly confirm the hydride nature of larger MMCCs, which are systematically NMR silent [30,135,154,212].

Addition/removal of electrons to MMCCs may be completely reversible without any apparent structural change, or may be accompanied by small structural rearrangements, or may be accompanied by irreversible chemical reactions, or may lead to complete decomposition. Electrochemical studies are, therefore, fundamental for identifying the mechanisms and optimal experimental conditions for the selected process. Small (reversible) structural changes may involve variations of CO stereochemistry, M–M bond lengthening, cage distortion, or a combination of these. Related irreversible processes leading to effective chemical reactions include CO elimination (or addition), M–M bond breakage, complete rearrangement of the metal cage, cluster condensation or fragmentation.

A complete understanding of these redox-induced processes (and the corresponding experimental conditions), which may be induced in a MMCC by redox events, is of paramount importance for their exploitation in synthetic purposes and electrocatalytic applications. Electrochemical studies, in combination with structural, spectroscopic and computational methods, are therefore required to fully unravel the potentialities of MMCCs and molecular nanoclusters in general. In view of the rich information that can be obtained by electrochemical methods and their complementarity to other techniques, electrochemistry should be employed more systematically in the future for the study of MMCCs and other molecular nanoclusters.

The synthesis, structural characterization, and electrochemical investigation of larger MMCCs are key issues for the future of the topic herein described. The main aim is to experimentally observe a further decrease of $\Delta E^{\circ\prime}_{av}$, up to complete metallization of the metal core of the cluster. Moreover, widening the number and size of investigated MMCCs should lead to a better understanding of the relationships among structure and composition of the metal core, ligand interactions, electronic status, chemical properties and electrochemical features of MMCCs. A value of $\Delta E^{\circ\prime}_{av}$ close to thermal energy (RT) could lead to auto-disproportionation equilibria in solution. A hint of such disproportionation processes has been, for instance, observed in some large Pt MMCCs whose electrochemistry indicates that odd-electron electrogenerated species are sometimes less stable than even-electron species [72,83,164]. It is expected that disproportionation processes will become more common with further increasing cluster nuclearity, and their experimental study should be a fascinating challenge. To add complexity and richness to the system, also protonation/deprotonation reactions could be present in larger MMCCs, as already observed in several instances.

Paramagnetism of odd and even electron MMCCs is well-established, even though the number of investigated clusters is limited [98,153]. This is due to synthetic limitations and to the high sensitivity to impurities of magnetic measurements. *In situ* EPR-SEC could be particularly effective in investigating the magnetic properties of electrogenerated MMCCs, especially if conducted at low temperatures. Some examples have already appeared in the literature [137,143], but a more systematic approach would be highly beneficial for understanding magnetism especially in larger MMCCs. This could lead to the application of MMCCs as molecular nanomagnets or as components of charge-transfer materials.

Finally electrocatalysis by MMCCs has gained significant attention in recent years [25,53–58,201,224–229]. Fundamental electrochemical studies are very important for fully elucidating the role of MMCCs in electrocatalytic processes and to select the best electrocatalysts.

Declaration of competing interest

The authors declare that they have no known competing financial interests or personal relationships that could have appeared to influence the work reported in this paper.

Acknowledgements

We gratefully thank the University of Bologna and Pisa for financial support. We thank the referees for useful suggestions in revising the manuscript.

Data availability

No data was used for the research described in the article.

References

[1] A.J. Bard, M. Stratmann, Encyclopedia of Electrochemistry, Wiley-VCH, New York, 2002.
[2] J.O'.M. Bockris, A.K.N. Reddy, M.G. Aldeco, Modern Electrochemistry 2A, Springer, New York, NY, 2000.
[3] P. Zanello, Inorganic Electrochemistry, RSC, Cambridge, 2003.
[4] P. Zanello, F. Fabrizi de Biani, C. Nervi, Inorganic Electrochemistry, 2nd edition, RSC Publishing, Cambridge, 2012.
[5] A.J.L. Pombeiro, J.A. McCleverty, Molecular Electrochemistry of Inorganic, Bioinorganic and Organometallic Compounds, in: Nato Science Series C, Springer, Dordrecht, 1993.
[6] R.W. Murray, Nanoelectrochemistry: metal nanoparticles, nanoelectrodes, and nanopores, Chem. Rev. 108 (2008) 2688–2720.
[7] R. Jin, C. Zeng, M. Zhou, Y. Chen, Atomically precise colloidal metal nanoclusters and nanoparticles: fundamentals and opportunities, Chem. Rev. 116 (2016) 10346–10413.
[8] S. Li, N.-N. Li, X.-Y. Dong, S.-Q. Zang, T.C.W. Mak, Chemical flexibility of atomically precise metal clusters, Chem. Rev. 124 (2024) 7262–7378.
[9] X. Zou, X. Kang, M. Zhu, Recent developments in the investigation of driving forces for transforming coinage metal nanoclusters, Chem. Soc. Rev. 52 (2023) 5892–5967.
[10] M.F. Matus, H. Häkkinen, Understanding ligand-protected noble metal nanoclusters at work, Nat. Rev. Mater. 8 (2023) 372–389.
[11] C. Sun, B.K. Teo, C. Deng, J. Lin, G.-G. Luo, C.-H. Tung, D. Sun, Hydrido-coinage-metal-clusters: rational design, synthetic protocols and structural characteristics, Coord. Chem. Rev. 427 (2021) 213576.

[12] T.-H. Chiu, J.-H. Liao, R.P. Brocha Silahi, M.N. Pillay, C.W. Liu, Hydride-doped coinage metal superatom and their catalytic applications, Nanoscale Horiz. 9 (2024) 675–692.
[13] X. Kang, Y. Li, M. Zhu, R. Jin, Atomically precise alloy nanoclusters: syntheses, structures, and properties, Chem. Soc. Rev. 49 (2020) 6443–6514.
[14] T. Kawawaki, T. Okada, D. Hirayama, Y. Negishi, Atomically precise metal nanoclusters as catalysts for electrocatalytic CO_2 reduction, Green Chem. 26 (2024) 122–163.
[15] R. Jin, G. Li, S. Sharma, Y. Li, X. Du, Toward active-site tailoring in heterogeneous catalysis by atomically precise metal nanoclusters with crystallographic structures, Chem. Rev. 121 (2021) 567–648.
[16] H.-H. Xie, L.-J. Zhou, P.-F. Cui, W.-C. Zhang, Icosahedral carboranes-based metal nanoclusters: From fascinating structures to polychrome properties and applications, Coord. Chem. Rev. 542 (2025) 216803.
[17] H. Li, X. Kang, M. Zhu, Nanocluster-based aggregates: assembled forms, driving forces, and structure-related properties, Coord. Chem. Rev. 539 (2025) 216738.
[18] K. Kwak, D. Lee, Electrochemsitry of atomically precise metal nanoclusters, Acc. Chem. Res. 52 (2019) 12–22.
[19] J.A. Trindell, Z. Duan, G. Henkelman, R.M. Criiks, Well-defined nanoparticle electrocatalyts for the refinement of theory, Chem. Rev. 120 (2020) 814–850.
[20] T. Kawawaki, Y. Negishi, Elucidation of the electronic structures of thiolate-protected gold nanoclusters by electrochemical measurements, Dalton Trans. 52 (2023) 15152–15167.
[21] E.S. Varo, R.E. Tankard, J.L. Needham, E. Gioria, F. Romeggio, I. Chorkendorff, C. D. Damsgaard, J. Kibsgaard, An experimental perspective on nanoparticle electrochemistry, Phys. Chem. Chem. Phys. 26 (2024) 17456.
[22] J. Zhao, A. Ziarati, T. Bürgi, Tuning atomically precise gold nanoclusters for selective electroreduction of CO_2, Angew. Chem. Int. Ed. 64 (2025) e202504320.
[23] X. Yuan, M. Zhu, Recent advances in atomically precise metal nanoclusters for electrocatalytic applications, Inorg. Chem. Front. 10 (2023) 3995–4007.
[24] S. Zacchini, Using metal carbonyl clusters to develop a molecular approach towards metal nanoparticles, Eur. J. Inorg. Chem. (2011) 4125–4145.
[25] C. Cesari, J.-H. Shon, S. Zacchini, L.A. Berben, Metal carbonyl clusters of groups 8-10: synthesis and catalysis, Chem. Soc. Rev. 50 (2021) 9503–9539.
[26] C. Cesari, C. Femoni, F. Forti, M.C. Iapalucci, G. Scorzoni, S. Zacchini, Surface decorated metal carbonyl clusters: bridging organometallic molecular clusters and atomically precise ligated nanoclusters, Dalton Trans. 54 (2025) 2224–2251.
[27] C. Cesari, C. Femoni, F. Forti, M.C. Iapalucci, G. Scorzoni, S. Zacchini, Isomerism in molecular metal carbonyl clusters, Eur. J. Inorg. Chem. 27 (2024) e202400220.
[28] P.R. Raithby, The growth of higher nuclearity carbonyl clusters of ruthenium and osmium, J. Organomet. Chem. 1005 (2024) 122979.
[29] E.G. Mednikov, L.F. Dahl, Syntheses, structures and properties of primarily nanosized homo/heterometallic palladium CO/PR_3-ligated clusters, Phil. Trans. R. Soc. A 368 (2010) 1301–1332.
[30] C. Cesari, C. Femoni, F. Forti, M.C. Iapalucci, G. Scorzoni, S. Zacchini, Molecular hydride carbonyl clusters and nanoclusters, Inorg. Chim. Acta 574 (2025) 122394.
[31] C. Cesari, C. Femoni, M.C. Iapalucci, S. Zacchini, Molecular Fe, Co and Ni carbide carbonyl clusters and nanoclusters, Inorg. Chim. Acta. 544 (2023) 121235.
[32] I. Ciabatti, C. Femoni, M.C. Iapalucci, S. Ruggieri, S. Zacchini, The role of gold in transition metal carbonyl clusters, Coord. Chem. Rev. 355 (2018) 27–38.
[33] B. Berti, C. Femoni, M.C. Iapalucci, S. Ruggieri, S. Zacchini, Functionalization, modification, and transformation of platinum chini clusters, Eur. J. Inorg. Chem. (2018) 3285–3296.
[34] C. Femoni, M.C. Iapalucci, S. Ruggieri, S. Zacchini, From mononuclear complexes to molecular nanoparticles: the buildup of atomically precise heterometallic rhodium carbonyl nanoclusters, Acc. Chem. Res. 51 (2018) 2748–2755.
[35] B.F.G. Johnson, S. McIndoe, Spectroscopic and mass spectrometric methods for the characterisation of metal clusters, Coord. Chem. Rev. 200-202 (2000) 901–932.
[36] G. Hogarth, S.E. Kabir, E. Nordlander, Cluster chemistry in the Noughties: new developments and their relationship to nanoparticles, Dalton Trans. 39 (2010) 6153–6174.
[37] M. Sellin, I. Krossing, Homoleptic transition metal carbonyl cations: synthetic approaches, characterization and follow-up chemistry, Acc. Chem. Res. 56 (2023) 2776–2787.
[38] A.V. Virovets, E. Peresypkina, M. Scheer, Structural chemistry of giant metal based supramolecules, Chem. Rev. 121 (2021), 14885-14554.
[39] F.A. Cotton, Transition-metal compounds containing clusters of metal atoms, Q. Rev. Chem. Soc. 20 (1966) 389–401.
[40] E.I. Muetterties, T.N. Rhodin, E. Band, C.F. Brucker, W.R. Pretzer, Clusters and surfaces, Chem. Rev. 79 (1979) 91–137.
[41] E.I. Muetterties, J. Stein, Mechanistic features of catalytic carbon monoxide hydrogenation reactions, Chem. Rev. 79 (1979) 479–490.
[42] C. Femoni, M.C. Iapalucci, F. Kaswalder, G. Longoni, S. Zacchini, The possible role of metal carbonyl clusters in nanoscience and nanotechnologies, Coord. Chem. Rev. 250 (2006) 1580–1604.
[43] P. Zanello, Electrochemistry of metal-sulfur clusters: stereochemical consequences of thermodynamically characterized redox changes, Part I. Homometal clusters, Coord. Chem. Rev. 83 (1988) 199–275.
[44] P. Zanello, Electrochemistry of metal-sulfur clusters: stereochemical consequences of thermodynamically characterized redox changes, Part II. Heterometal clusters, Coord. Chem. Rev. 87 (1988) 1–54.
[45] P. Zanello, Stereochemical aspects associated with the redox behaviour of heterometal clusters, Struct. Bond. 79 (1992) 101–214.
[46] P. Zanello, Stereochemical aspects of the redox propensity of homometal carbonyl clusters, in: P. Zanello (Ed.), Stereochemistry of Organometallic and Inorganic Compounds Vol. 5, Elsevier, Amsterdam, 1994, pp. 163–408.
[47] P. Zanello, F. Fabrizi de Biani, Bimetallic effects on the redox activity of transition-metal carbonyl clusters, in: P. Braunstein, L.A. Oro, P.R. Raithby (Eds.), Metal Clusters in Chemistry Vol. 2, Wiley-VCH, 1999, pp. 1104–1136.
[48] G. Longoni, C. Femoni, M.C. Iapalucci, P. Zanello, Electron-sink features of homoleptic transition-metal carbonyl clusters, in: P. Braunstein, L.A. Oro, P. R. Raithby (Eds.), Metal Clusters in Chemistry Vol. 2, Wiley-VCH, 1999, pp. 1137–1158.
[49] P. Zanello, Structure and electrochemistry of transition metal carbonyl clusters with interstitial or semi-interstitial atoms: contrast between nitrides or phosphides and carbides, in: M. Gielen, R. Willem, B. Wrackmeyer (Eds.), Physical Organometallic Chemistry, Vol. 3: Unusual Structures and Physical Properties in Organometallic Chemistry, John Wiley, Chichester, UK, 2002, pp. 1–49.
[50] F. Rossi, P. Zanello, Electron reservoir activity of high-nuclearity transition metal carbonyl clusters, Portug. Electrochim. Acta 29 (2011) 309–327.
[51] P. Lemoine, Progress in cluster electrochemistry, Coord. Chem. Rev. 83 (1988) 169–197.
[52] P. Lemoine, Electrochemistry of transition metal clusters, Coord. Chem. Rev. 47 (1982) 55–88.
[53] S. Pattanayak, R.E. Siegel, Y. Liu, J.C. Fettinger, L.A. Berben, Amine groups alter product selectivity and rate of catalytic hydride transfer reactions, Chem. Sci. 16 (2025) 13241–13248.
[54] R.E. Siegel, M. Aceves, L.A. Berben, Direct electrochemical conversion of CO_2 sorbent solution to formate by a molecular iron catalyst, ACS Energy Lett. 9 (2024) 2896–2901.
[55] S. Pattanayak, N.D. Loewen, L.A. Berben, Using substituted $[Fe_4N(CO)_{12}]^-$ as platform to probe the effect of cation and Lewis acid location on redox potential, Inorg. Chem. 62 (2023) 1919–1925.
[56] C.R. Carr, A. Taheri, L.A. Berben, Fast proton transfer and hydrogen evolution reactivity mediated by $[Co_{13}C_2(CO)_{24}]^{4-}$, J. Am. Chem. Soc. 142 (2020) 12299–12305.
[57] S. Pattanayak, L.A. Berben, Cobalt carbonyl clusters enable independent control of two proton transfer rates in the mechanism for hydrogen evolution, ChemElectroChem 8 (2021) 2488–2494.
[58] N.D. Loewen, T.V. Neelakantan, L.A. Berben, Renewable formate from C-H Bond formation with CO_2: using iron carbonyl clusters as electrocatalysts, Acc. Chem. Res. 50 (2017) 2362–2370.
[59] S. He, Z. Ding, Progress in electrochemistry and electrochemiluminescence of metal clusters, Curr. Opin. Electrochem. 7 (2018) 109–117.
[60] K. Izutsu, Electrochemistry in Nonaqueous Solutions, 2nd ed, John Wiley & Sons Incorporated, Hoboken, 2009.
[61] F. Scholz, Electroanalytical Methods: Guide to Experiments and Applications, 2nd ed, Springer, Berlin / Heidelberg, Berlin, Heidelberg, 2010.
[62] N. Elgrishi, K.J. Rountree, B.D. McCarthy, E.S. Rountree, T.T. Eisenhart, J. L. Dempsey, A practical beginner's guide to cyclic voltammetry, J. Chem. Educ. 95 (2018) 197–206.
[63] R. Holze, Experimental Electrochemistry: A Laboratory Textbook, Wiley-VCH, Weinheim, 2009.
[64] A.J. Bard, L.R. Faulkner, H.S. White, Electrochemical Methods: Fundamentals and Applications, Third edition, Wiley, Hoboken, NJ, 2022.
[65] S.J. Hendel, E.R. Young, Introduction to electrochemistry and the use of electrochemistry to synthesize and evaluate catalysts for water oxidation and reduction, J. Chem. Educ. 93 (2016) 1951–1956.
[66] S. Ranganathan, T.-C. Kuo, R.L. McCreery, Facile preparation of active glassy carbon electrodes with activated carbon and organic solvents, Anal. Chem. 71 (1999) 3574–3580.
[67] B. Schmidt, D. King, J. Kariuki, Designing and using 3D-printed components that allow students to fabricate low-cost, adaptable, disposable, and reliable Ag/AgCl reference electrodes, J. Chem. Educ. 95 (2018) 2076–2080.
[68] J.M. Thomas, Student construction of a gel-filled Ag/AgCl reference electrode for use in a potentiometric titration, J. Chem. Educ. 76 (1999) 97.
[69] R.G. Compton, C.E. Banks, Understanding voltammetry, Fourth edition, World Scientific, New Jersey, 2025.
[70] P.T. Kissinger, W.R. Heineman, Cyclic voltammetry, J. Chem. Educ. 60 (1983) 702.
[71] C. Cesari, T. Funaioli, B. Berti, C. Femoni, M.C. Iapalucci, F.M. Vivaldi, S. Zacchini, Atomically precise Ni–Pd alloy carbonyl nanoclusters: synthesis, total structure, electrochemistry, spectroelectrochemistry, and electrochemical impedance spectroscopy, Inorg. Chem. 60 (2021) 16713–16725.
[72] E. Cattabriga, I. Ciabatti, C. Femoni, T. Funaioli, M.C. Iapalucci, S. Zacchini, Syntheses, structures, and electrochemistry of the defective *ccp* $[Pt_{33}(CO)_{38}]^{2-}$ and the *bcc* $[Pt_{40}(CO)_{40}]^{6-}$ molecular nanoclusters, Inorg. Chem. 55 (2016) 6068–6079.
[73] E. Pungor, Z. Fehér, M. Váradi, B.H. Campbell, Hydrodynamic Voltammetry, C R C Crit. Rev. Anal. Chem. 9 (1980) 97–165.
[74] J.V. Macpherson, Recent advances in hydrodynamic modulation voltammetry, Electroanalysis 12 (2000) 1001–1011.
[75] C. Batchelor-McAuley, E. Kätelhön, E.O. Barnes, R.G. Compton, E. Laborda, A. Molina, Recent advances in voltammetry, ChemistryOpen 4 (2015) 224–260.
[76] C. Femoni, M.C. Iapalucci, G. Longoni, S. Zacchini, S. Fedi, F. Fabrizi De Biani, Cage rearrangements in dodecanuclear Co–Pt dicarbido clusters promoted by redox reactions, Eur. J. Inorg. Chem. 2012 (2012) 2243–2250.

[77] A. Escuer, R. Vicente, M.S.E. Fallah, E.C. Sañudo, S.J. Teat, F.F. De Biani, P. Zanello, Octanuclear manganese(II,III) clusters stabilized with diamino-alcoxo ligands, Dalton Trans. 9924 (2009).

[78] D. Collini, F.F. De Biani, S. Fedi, C. Femoni, F. Kaswalder, M.C. Iapalucci, G. Longoni, C. Tiozzo, S. Zacchini, P. Zanello, Synthesis and electrochemistry of new Rh-centered and conjuncto rhodium carbonyl clusters. X-ray structure of $[NEt_4]_3[Rh_{15}(CO)_{27}]$, $[NEt_4]_3[Rh_{15}(CO)_{25}(MeCN)_2]\cdot 2MeCN$, and $[NEt_4]_3[Rh_{17}(CO)_{37}]$, Inorg. Chem. 46 (2007) 7971–7981.

[79] A. Bernardi, C. Femoni, M.C. Iapalucci, G. Longoni, S. Zacchini, S. Fedi, P. Zanello, Synthesis, Structures and electrochemistry of new carbonylnickel octacarbide clusters: the distorting action of carbide atoms in the growth of Ni cages and the first example of the inclusion of a carbon atom within a (distorted) Ni octahedral cage, Eur. J. Inorg. Chem. 2010 (2010) 4831–4842.

[80] B. Berti, C. Cesari, C. Femoni, T. Funaioli, M.C. Iapalucci, S. Zacchini, Redox active Ni–Pd carbonyl alloy nanoclusters: syntheses, molecular structures and electrochemistry of $[Ni_{22-x}Pd_{20+x}(CO)_{48}]^{6-}$ ($x = 0.62$), $[Ni_{29-x}Pd_{6+x}(CO)_{42}]^{6-}$ ($x = 0.09$) and $[Ni_{29+x}Pd_{6-x}(CO)_{42}]^{6-}$ (x = 0.27), Dalton Trans. 49 (2020) 5513–5522.

[81] J.G. Osteryoung, R.A. Osteryoung, Square wave voltammetry, Anal. Chem. 57 (1985) 101–110.

[82] M. Bortoluzzi, I. Ciabatti, C. Femoni, T. Funaioli, M. Hayatifar, M.C. Iapalucci, G. Longoni, S. Zacchini, Homoleptic and heteroleptic Au(I) complexes containing the new $[Co_5C(CO)_{12}]^-$ cluster as ligand, Dalton Trans. 43 (2014) 9633–9646.

[83] C. Cesari, B. Berti, T. Funaioli, C. Femoni, M.C. Iapalucci, D. Pontiroli, G. Magnani, M. Riccò, M. Bortoluzzi, F.M. Vivaldi, S. Zacchini, Atomically precise platinum carbonyl nanoclusters: synthesis, total structure, and electrochemical investigation of $[Pt_{27}(CO)_{31}]^{4-}$ displaying a defective structure, Inorg. Chem. 61 (2022) 12534–12544.

[84] O. Cador, H. Cattey, J.-F. Halet, W. Meier, Y. Mugnier, J. Wachter, J.-Y. Saillard, B. Zouchoune, M. Zabel, Electron-sponge behavior and electronic structures in cobalt-centered pentagonal prismatic $Co_{11}Te_7(CO)_{10}$ and $Co_{11}Te_5(CO)_{15}$ cluster anions, Inorg. Chem. 46 (2007) 501–509.

[85] R.G. Compton, E. Kätelhön, K.R. Ward, E. Laborda, Understanding voltammetry: simulation of electrode processes, Second edition, World Scientific, New Jersey, 2020.

[86] Y. Mai, A.K. Balzen, R.K. Torres, M.P. Callahan, A.C. Colson, A modular strategy for expanding electron-sink capacity in noncanonical cluster assemblies, Inorg. Chem. 60 (2021) 17733–17743.

[87] B. Tulyathan, W.E. Geiger, Structural consequences of electron-transfer reactions. Part 12. Multi electron processes involving structural changes. The two-electron reduction of hexaosmium carbonyl cluster (Os6(CO)18), J. Am. Chem. Soc. 107 (1985) 5960–5967.

[88] H. Wadepohl, S. Gebert, H. Pritzkow, D. Osella, C. Nervi, J. Fiedler, Redox chemistry of $[Co_4(CO)_3(\mu_3\text{-}CO)_3(\mu_3\text{-}C_7H_7)(\eta^5\text{-}C_7H_9)]$ – reversible carbon–carbon coupling versus metal cluster degradation, Eur. J. Inorg. Chem. 2000 (2000) 1833–1843.

[89] J.B. Fernandes, L.Q. Zhang, F.A. Schultz, Correlation of heterogeneous electron transfer rate with structural change and environmental factors in the two-electron oxidation of $W_2(CO)_8(\mu\text{-}SBz)_2^{2-}$, J. Electroanal. Chem. Interf. Electrochem. 297 (1991) 145–161.

[90] A. Albinati, F. Balzano, F. Fabrizi De Biani, P. Leoni, G. Manca, L. Marchetti, S. Rizzato, G. Uccello Barretta, P. Zanello, Synthesis, structure, and electrochemistry of the dicluster molecular pincer $[Pt_3(\mu\text{-}PBu^t_2)_3(CO)_2]_2(\mu\text{-}1',1'''\text{-}$diethynylbiferrocene), Inorg. Chem. 49 (2010) 3714–3720.

[91] J.H. Brown, Development and use of a cyclic voltammetry simulator to introduce undergraduate students to electrochemical simulations, J. Chem. Educ. 92 (2015) 1490–1496.

[92] S. Wang, J. Wang, Y. Gao, Development and use of an open-source, user-friendly package to simulate voltammetry experiments, J. Chem. Educ. 94 (2017) 1567–1570.

[93] M. Rudolph, D.P. Reddy, S.W. Feldberg, A simulator for cyclic voltammetric responses, Anal. Chem. 66 (1994) 589A–600A.

[94] W. Kaim, J. Fiedler, Spectroelectrochemistry: the best of two worlds, Chem. Soc. Rev. 38 (2009) 3373–3382.

[95] W. Kaim, A. Klein, Spectroelectrochemistry, The Royal Society of Chemistry, 2008.

[96] Y. Zhai, Z. Zhu, S. Zhou, C. Zhu, S. Dong, Recent advances in spectroelectrochemistry, Nanoscale 10 (2018) 3089–3111.

[97] F. Hartl, R.P. Groenestein, T. Mahabiersing, Air-tight three-electrode design of coaxial electrochemical-EPR cell for redox studies at low temperatures, Collect. Czech. Chem. Commun. 66 (2001) 52–66.

[98] M.P. Cifuentes, M.G. Humphrey, J.E. McGrady, P.J. Smith, R. Stranger, K. S. Murray, B. Moubaraki, High nuclearity ruthenium carbonyl cluster chemistry. 5. Local density functional, electronic spectroscopy, magnetic susceptibility, and electron paramagnetic resonance studies on (carbido)decaruthenium carbonyl clusters, J. Am. Chem. Soc. 119 (1997) 2647–2655.

[99] P. Rapta, R. Fáber, L. Dunsch, A. Neudeck, O. Nuyken, In situ EPR and UV-vis spectroelectrochemistry of hole-transporting organic substrates, Spectrochim. Acta Part A: Mol. Biomol. Spectrosc. 56 (2000) 357–362.

[100] E. Dmitrieva, A.A. Popov, H. Hartmann, EPR/UV–Vis–NIR spectroelectrochemical characterization of 10H-phenothiazinyl-substituted oligothiophenes, Electrochim. Acta 515 (2025) 145714.

[101] M. Krejčik, M. Daněk, F. Hartl, Simple construction of an infrared optically transparent thin-layer electrochemical cell, J. Electroanal. Chem. Interf. Electrochem. 317 (1991) 179–187.

[102] C. Capacci, I. Ciabatti, C. Femoni, M.C. Iapalucci, T. Funaioli, S. Zacchini, V. Zanotti, Molecular nickel phosphide carbonyl nanoclusters: synthesis, structure, and electrochemistry of $[Ni_{11}P(CO)_{18}]^{3-}$ and $[H_{6-n}Ni_{31}P_4(CO)_{39}]^{n-}$ (n = 4 and 5), Inorg. Chem. 57 (2018) 1136–1147.

[103] C. Femoni, T. Funaioli, M.C. Iapalucci, S. Ruggieri, S. Zacchini, Rh-Sb nanoclusters: synthesis, structure, and electrochemical studies of the atomically precise $[Rh_{20}Sb_3(CO)_{36}]^{3-}$ and $[Rh_{21}Sb_2(CO)_{38}]^{5-}$ carbonyl compounds, Inorg. Chem. 59 (2020) 4300–4310.

[104] G. Bussoli, A. Boccalini, M. Bortoluzzi, C. Cesari, M.C. Iapalucci, T. Funaioli, G. Scorzoni, S. Zacchini, S. Ruggieri, C. Femoni, Atomically precise rhodium-indium carbonyl nanoclusters: synthesis, characterization, crystal structure and electron-sponge features, Nanoscale 16 (2024) 17852–17867.

[105] C. Cesari, M. Bortoluzzi, T. Funaioli, C. Femoni, M.C. Iapalucci, S. Zacchini, Highly reduced ruthenium carbide carbonyl clusters: synthesis, molecular structure, reactivity, electrochemistry, and computational investigation of $[Ru_6C(CO)_{15}]^{4-}$, Inorg. Chem. 62 (2023) 14590–14603.

[106] T. Funaioli, C. Cesari, B. Berti, M. Bortoluzzi, C. Femoni, F. Forti, M.C. Iapalucci, G. Scorzoni, S. Zacchini, Chemical and electrochemical investigation of the oxidation of a highly reduced Fe_6C iron carbide carbonyl cluster: a synthetic route to heteroleptic Fe_6C and Fe_5C clusters, Inorg. Chem. 64 (2025) 9744–9757.

[107] N.T. Lucas, J.P. Blitz, S. Petrie, R. Stranger, M.G. Humphrey, G.A. Heath, V. Otieno-Alego, Mixed-metal cluster chemistry. 19. Crystallographic, spectroscopic, electrochemical, spectroelectrochemical, and theoretical studies of systematically varied tetrahedral group 6−iridium clusters, J. Am. Chem. Soc. 124 (2002) 5139–5153.

[108] R.E. Benfield, Magnetic Properties and UV-Visible Spectroscopic Studies of Metal Cluster Compounds, in: L.J. de Jongh (Ed.), Physics and Chemistry of Metal Cluster Compounds, Kluwer Academic Publishers, Dordrecht, 1994, pp. 249–275.

[109] M.P. Cifuentes, M.G. Humphrey, G.A. Heath, High nuclearity ruthenium carbonyl cluster chemistry VI. Cyclic voltammetric and spectroelectrochemical studies of $[Ru_{10}(\mu\text{-}H)(\mu_6\text{-}C)(CO)_{24}]^-$ and $[Ru_{10}(\mu_6\text{-}C)(CO)_{24}]^{2-}$, Inorg. Chim. Acta 259 (1997) 273–280.

[110] B. Suo, K. Shen, Z. Li, W. Liu, Performance of TD-DFT for excited states of open-shell transition metal compounds, J. Phys. Chem. A 121 (2017) 3929–3942.

[111] D.M.P. Mingos, Structural and bonding patterns in gold clusters, Dalton Trans. 44 (2015) 6680–6695.

[112] S.M. Owen, Electron counting in clusters: a view of the concepts, Polyhedron 7 (1988) 253–283.

[113] D.M.P. Mingos, Polyhedral skeletal electron pair approach, Acc. Chem. Res. 17 (1984) 311–319.

[114] B.K. Teo, G. Longoni, F.R.K. Chung, Applications of topological electron-counting theory to polyhedral metal clusters, Inorg. Chem. 23 (1984) 1257–1266.

[115] J. Wei, R. Marchal, D. Astruc, S. Kahlal, J.-F. Halet, J.-Y. Saillard, Looking at platinum carbonyl nanoclusters as superatoms, Nanoscale 14 (2022) 3946–3957.

[116] W. Unkrig, K. Kloiber, B. Butschke, D. Kratzert, I. Krossing, Altering charges on heterobimetallic transition-metal carbonyl clusters, Chem. Eur. J. 26 (2020) 12373–12381.

[117] A. Muñoz-Castro, sp^3-hybridization in superatomic clusters. Analogues to simple molecules involving the Au_6 core, Chem. Sci. 5 (2014) 4749–4754.

[118] C. Amatore, J.-N. Verpeaux, Electrochemical reduction of $Fe(CO)_5$ revisited, Organometallics 7 (1988) 2426–2428.

[119] R. Hourihane, T.R. Spalding, G. Ferguson, T. Deeney, P. Zanello, Characterisation of a new solid-state isomer of the $[Fe_5N(CO)_{14}]^-$ ion, J. Chem. Soc., Dalton Trans. (1993) 43–46.

[120] B.M. Peake, P.H. Rieger, B.H. Robinson, J. Simpson, Paramagnetic organometallic molecules. 11. The $SFeCo_2(CO)_9^-$ radical anion and the electronic structure of capped m_3 clusters, Inorg. Chem. 20 (1981) 2540–2543.

[121] A. Ceriotti, R. Della Pergola, L. Garlaschelli, F. Laschi, M. Manassero, N. Masciocchi, M. Sansoni, P. Zanello, Iron-iridium mixed-metal carbonyl clusters. 3. synthesis, chemical characterization, electrochemical behavior, and solid-state structures of $[NEt_4]_3[FeIr_5(CO)_{15}]$, $[NMe_3(CH_2Ph)]_2[HFeIr_5(CO)_{15}]$, and $[NMe_3(CH_2Ph)][FeIr_5(CO)_{16}]$. spectroscopic and chemical evidence for the existence of $[HFe_3Ir(CO)_{12}]^{2-}$, $[H_2Fe_3Ir(CO)_{12}]^-$, and $[H_2FeIr_5(CO)_{15}]^-$, Inorg. Chem. 30 (1991) 3349–3357.

[122] D. Osella, E. Stein, C. Nervi, P. Zanello, F. Laschi, A. Cinquantini, E. Rosenberg, J. Fledler, Redox behavior of the electronically unsaturated clusters $Os_3(\mu\text{-}H)_2(CO)_9L$ and their saturated congeners $Os_3(\mu\text{-}H)(H)(CO)_{10}L$ (L = CO, PPh_3, $AsPh_3$), Organometallics 10 (1991) 1929–1934.

[123] R.J. Goudsmit, J.G. Jeffrey, B.F.G. Johnson, J. Lewis, R.C.S. McQueen, A. J. Sanders, J.-C. Liu, An improved synthesis of Os_6 raft-like clusters, J. Chem. Soc., Chem. Commun. (1986) 24–26.

[124] T.A. Albright, K.A. Yee, J.-Y. Saillard, S. Kahlal, J.-F. Halet, J.S. Leigh, K. H. Whitmire, Capping considerations in main-group/transition-metal clusters: synthetic, structural, and theoretical discussions of $[E_2Co_4(CO)_{10}(\mu\text{-}CO)]^{-/2-}$ (E = Sb. Bi), Inorg. Chem. 30 (1991) 1179–1190.

[125] C.S. Hong, L.A. Berben, J.R. Long, Synthesis and characterization of a decacobalt carbonyl cluster with two semi-interstitial phosphorus atoms, Dalton Trans. (2003) 2119–2120.

[126] F. Calderoni, F. Demartin, M.C. Iapalucci, F. Laschi, G. Longoni, P. Zanello, Synthesis and chemical and electrochemical characterization of Fe-S carbonyl clusters. X-ray crystal structures of $[N(PPh_3)_2]_2[Fe_5S_2(CO)_{14}]$ and $[N(PPh_3)_2]_2[Fe_6S_6(CO)_{12}]$, Inorg. Chem. 35 (1996) 898–905.

[127] R. Della Pergola, L. Garlaschelli, C. Mealli, D.M. Proserpio, P. Zanello, Electrochemistry of the two-dimensional heteronuclear $[Fe_3Pt_3(CO)_{15}]^n$ clusters (n = 2-, 1-, o): MO treatment of the skeletal adjustments in 86-84e^- congeners, J. Clust. Sci. 1 (1990) 93–106.

[128] R.D. Adams, I. Arafa, G. Chen, J.-C. Lii, J.-G. Wang, New platinum-iron carbonyl cluster complexes and their reactions with alkynes, Organometallics 9 (1990) 2350–2357.

[129] G. Manca, F. Fabrizi de Biani, M. Corsini, C. Cesari, C. Femoni, M.C. Iapalucci, S. Zacchini, A. Ienco, Inverted ligand field in a pentanuclear bow tie Au/Fe carbonyl cluster, Inorg. Chem. 61 (2022) 3484–3492.

[130] S.R. Drake, B.F.G. Johnson, J. Lewis, R.C.S. McQueen, High nuclearity osmium cluster radicals, J. Chem. Soc., Dalton Trans. (1987) 1051–1054.

[131] S.R. Drake, M.H. Barley, B.F.G. Johnson, J. Lewis, Redox chemistry of the cluster $[Os_{10}C(CO)_{24}]^{2-}$, Organometallics 7 (1988) 806–812.

[132] R.D. Adams, M.S. Alexander, I. Arafa, W. Wu, Cluster Synthesis, 36. New platinum-ruthenium and platinum-osmium carbonyl cluster complexes from the reactions of the complexes $Pt_2M_4(CO)_{18}$ (M = Ru, Os) with cycloocta-a,5-diene in the presence of UV irradiation, Inorg. Chem. 30 (1991) 4717–4723.

[133] I. Ciabatti, C. Femoni, M. Hayatifar, M.C. Iapalucci, G. Longoni, C. Pinzino, M. V. Solmi, S. Zacchini, The redox chemistry of $[Co_6C(CO)_{15}]^{2-}$: a synthetic route to new co-carbide carbonyl clusters, Inorg. Chem. 53 (2014) 3818–3831.

[134] A. Fumagalli, M. Costa, R. Della Pergola, P. Zanello, F. Fabrizi de Biani, P. Macchi, A. Sironi, Synthesis, structural and electrochemical characterization of the nitrido-carbonyl cluster anion $[Co_{13}N_2(CO)_{24}]^{3-}$. The different redox propensity of the two isostructural families $[Co_{13}N_2(CO)_{24}]^{n-}$ and $[Co_{13}C_2(CO)_{24}]^{m-}$, Inorg. Chim. Acta 350 (2003) 187–192.

[135] I. Ciabatti, C. Femoni, M. Gaboardi, M.C. Iapalucci, G. Longoni, D. Pontiroli, M. Riccò, S. Zacchini, Structural rearrangements induced by acid-base reactions in metal carbonyl clusters: the case of $[H_{3-n}Co_{15}Pd_9C_3(CO)_{38}]^{n-}$ (n = 0-3), Dalton Trans. 43 (2014) 4388–4399.

[136] A. Cinquantini, P. Zanello, R. Della Pergola, L. Garlaschelli, S. Martinengo, Electrochemistry of $[M_6(CO)_{15}]^{2-}$ anionic clusters (M = Co and Ir). Preparation and chemical characterization of $[Ir_6(CO)_{14}(NCO)]^-$ and the radical anion $[Ir_6(CO)_{15}]^-$. Proposed mechanism of formation of the hexanuclear substituted cluster $[Ir_6(CO)_{15}Cl]^-$, J. Organomet. Chem. 412 (1991) 215–224.

[137] R. Della Pergola, L. Garlaschelli, M. Manassero, N. Masciocchi, P. Zanello, Structure and electrochemical behavior of the paramagnetic anion $[Ir_{14}(CO)_{27}]^-$, possessing a trigonal bipyramidal arrangement of metal atoms, Angew. Chem. Int. Ed. 32 (1993) 1347–1349.

[138] V.G. Albano, F. Demartin, C. Femoni, M.C. Iapalucci, G. Longoni, M. Monari, P. Zanello, Synthesis and characterization of new paramagnetic nickel carbonyl clusters containing antimony atoms: X-ray structure of $[NEt_3CH_2Ph]_2[Ni_{15}(\mu_{12}\text{-}Sb)(CO)_{24}]$ and $[NEt_4]_3[Ni_{10}Sb_2(\mu_{12}\text{-}Ni)(CO)_{18}]$, J. Organomet. Chem. 593-594 (2000) 325–334.

[139] V.G. Albano, F. Demartin, M.C. Iapalucci, G. Longoni, M. Monari, P. Zanello, New icosahedral heterometallic nickel carbonyl clusters containing bismuth, J. Chem. Soc., Dalton Trans. (1992) 497–502.

[140] V.G. Albano, F. Demartin, M.C. Iapalucci, F. Laschi, G. Longoni, A. Sironi, P. Zanello, Icosahedral carbonyl clusters $[Ni_{10}Sb_2(\mu_{12}\text{-}Ni)\{Ni(CO)_3\}_2(CO)_{18}]^{n-}$ (n = 2, 3 or 4); synthesis, spectroscopic, electrochemical and bonding analysis. Crystal structures of $[Ni_{10}Sb_2(\mu_{12}\text{-}Ni)\{Ni(CO)_3\}_2(CO)_{18}]^{n-}$ (n = 2 or 3), J. Chem. Soc., Dalton Trans. (1991) 739–748.

[141] V.G. Albano, F. Calderoni, M.C. Iapalucci, G. Longoni, M. Monari, P. Zanello, Synthesis, chemical, and electrochemical characterization of the $[Ag_{13}\{\mu_3\text{-}Fe(CO)_4\}_8]^{n-}$ (n = 3, 4, 5) cluster anions: X-ray structural determination of $[N(PPh_3)_2]_3[Ag_{12}(\mu_{12}\text{-}Ag)\{\mu_3\text{-}Fe(CO)_4\}_8]$, J. Clust. Sci. 6 (1995) 107–123.

[142] R. Della Pergola, M. Bruschi, F. Fabrizi de Biani, A. Fumagalli, L. Garlaschelli, F. Laschi, M. Manassero, M. Sansoni, P. Zanello, A new multivalent cluster: synthesis, electrochemistry, solid state structure and computational studies on the iron-nickel mixed-metal nitride anions $[Fe_6Ni_6N_2(CO)_{24}]^{n-}$ (n = 2-4), C. R. Chim. 8 (2005) 1850–1855.

[143] E. Brivio, A. Ceriotti, R. Della Pergola, L. Garlaschelli, F. Demartin, M. Manassero, M. Sansoni, P. Zanello, F. Laschi, B.T. Heaton, Synthesis and solid-state structure of $[Pd_6Ru_6(CO)_{24}]^{2-}$. Electrochemistry and ^{13}C nuclear magnetic resonance spectra of [Fe6Pd6H(CO)24]3− and [Pd6Ru6(CO)24]2−,, J. Chem. Soc., Dalton Trans. (1994) 3237–3242.

[144] A.J. Amoroso, L.H. Gade, B.F.G. Johnson, J. Lewis, P.R. Raithby, W.-T. Wong, $(^nBu_4P)_2[Os_{20}(CO)_{40}]$, a thermolytically generated high-nuclearity cluster with a tetrahedral cubic-close-packed metal core, Angew. Chem. Int. Ed. 30 (1991) 107–109.

[145] J.P.-K. Lau, Y.-J. Gu, W.-T. Wong, High-yield synthesis of a new layered high-nuclearity carbonyl osmium-rhodium cluster complex – synthesis, structural characterization, and electrochemistry of $[PPN][Os_9Rh_3(\mu\text{-}CO)_2(CO)_{26}]$, Eur. J. Inorg. Chem. (2007) 3011–3014.

[146] K.-F. Yung, W.-T. Wong, $[\{N(PPh_3)\}_2\{Os_{18}Pd_3(\mu_6\text{-}C)_2(CO)_{42}\}]$: an osmium-palladium mixed-metal high-nuclearity carbonyl cluster, Angew. Chem. Int. Ed. 42 (2003) 553–555.

[147] J. Rimmelin, P. Lemoine, M. Gross, R. Mathieu, D. De Montauzon, The unusual electrochemical behaviour of $[Co_8(CO)_{18}C]^{2-}$ compared to $[M_6(CO)_{15}C]^{2-}$ (M = Co, Rh) and $[Fe_6(CO)_{16}C]^{2-}$ carbido clusters, J. Organomet. Chem. 309 (1986) 355–362.

[148] A. Fumagalli, P. Ulivieri, M. Costa, O. Crispu, R. Della Pergola, F. Fabrizi de Biani, F. Laschi, P. Zanello, P. Macchi, A. Sironi, Electron transfer and CO addition to polynitrido cobalt carbonyl clusters: parallel pathways for conversion of the $[Co_{10}N_2(CO)_{19}]^{4-}$ anion to the novel $[Co_{11}N_2(CO)_{21}]^{3-}$ anion, Inorg. Chem. 43 (2004) 2125–2131.

[149] G. Ciani, A. Sironi, S. Martinengo, L. Garlaschelli, R. Della Pergola, P. Zanello, F. Laschi, N. Masciocchi, Synthesis and X-ray characterization of the phosphido-carbonyl cluster anions $[Co_9(\mu_8\text{-}P)(CO)_{21}]^{2-}$ and $[Co_{10}(\mu_8\text{-}P)(CO)_{22}]^{3-}$, Inorg. Chem. 40 (2001) 3905–3911.

[150] H. Brunner, H. Cattey, W. Meier, Y. Mugnier, A.C. Stückl, J. Wachter, R. Wanninger, M. Zabel, Preparative and electrochemical investigations on the electron sponge behavior of cobalt telluride clusters: CO substitution in $[Co_{11}Te_7(CO)_{10}]^{n-}$ Ions (n = 1, 2) by PMe_2Ph and crystal structure of $[Co_{11}Te_7(CO)_5(PMe_2Ph)_5]$, Chem. Eur. J. 9 (2003) 3796–3802.

[151] R. Della Pergola, L. Garlaschelli, P. Macchi, I. Facchinetti, R. Ruffo, S. Racioppi, A. Sironi, From small metal clusters to molecular nanoarchitectures with a core-shell structure: the synthesis, redox fingerprint, theoretical analysis, and solid-state structure of $[Co_{38}As_{12}(CO)_{50}]^{4-}$, Inorg. Chem. 61 (2022) 9888–9896.

[152] R. Della Pergola, A. Fumagalli, F. Fabrizi de Biani, L. Garlaschelli, F. Laschi, M. C. Malatesta, M. Manassero, E. Roda, M. Sansoni, P. Zanello, Carbonyl-nitrido mixed-metal clusters: synthesis, reactivity, electrochemical behavior and solid-state structure of $[Co_5MoN(CO)_{14}]^{2-}$ and $[Co_5MoN(CO)_{14}AuPPh_3]^-$, Eur. J. Inorg. Chem. (2004) 3901–3906.

[153] C. Femoni, M.C. Iapalucci, G. Longoni, J. Wolowska, S. Zacchini, P. Zanello, S. Fedi, M. Riccò, D. Pontiroli, M. Mazzani, Magnetic behavior of odd- and even-electron metal carbonyl clusters: the case study of $[Co_8Pt_4C_2(CO)_{24}]^{n-}$ (n = 1, 2) carbide cluster, J. Am. Chem. Soc. 132 (2010) 2919–2927.

[154] D. Collini, F. Fabrizi de Biani, D.S. Dolzhnikov, C. Femoni, M.C. Iapalucci, G. Longoni, C. Tiozzo, S. Zacchini, P. Zanello, Synthesis, structure, and spectroscopic characterization of $[H_{8-n}Rh_{22}(CO)_{35}]^{n-}$ (n = 4, 5) and $[H_2Rh_{13}(CO)_{24}\{Cu(MeCN)\}_2]^-$ clusters: assessment of CV and DPV as techniques to circumstantiate the presence of elusive hydride atoms, Inorg. Chem. 50 (2011) 2790–2798.

[155] S. Ruggieri, G. Bussoli, M. Bortoluzzi, C. Cesari, T. Funaioli, S. Zacchini, M. C. Iapalucci, C. Femoni, Atomically precise rhodium-gold carbonyl nanoclusters: in-depth synthesis and multivalence of $[Rh_{16}Au_6(CO)_{36}]^{6-}$, and its correlation with $[Rh_{10}Au(CO)_{26}]^{3-}$, Eur. J. Inorg. Chem. (2024) e202400526.

[156] I. Ciabatti, C. Femoni, T. Funaioli, M.C. Iapalucci, S. Merighi, S. Zacchini, The redox chemistry of $[Ni_9C(CO)_{17}]^{2-}$ and $[Ni_{10}(C_2)(CO)_{16}]^{2-}$: synthesis, electrochemistry and structure of $[Ni_{12}C(CO)_{18}]^{4-}$ and $[Ni_{22}(C_2)_4(CO)_{28}(Et_2S)]^{2-}$, J. Organomet. Chem. 849-850 (2017) 299–305.

[157] C. Femoni, M.C. Iapalucci, G. Longoni, S. Zacchini, S. Fedi, F. Fabrizi de Biani, Nickel poly-acetylide carbonyl clusters: structural features, bonding and electrochemical behaviour, Dalton Trans. 41 (2012) 4649–4663.

[158] F. Calderoni, F. Demartin, F. Fabrizi de Biani, C. Femoni, M.C. Iapalucci, G. Longoni, P. Zanello, Electron-Sink behaviour of the carbonylnickel clusters $[Ni_{32}C_6(CO)_{36}]^{6-}$ and $[Ni_{38}C_6(CO)_{42}]^{6-}$: synthesis and characterization of the anions $[Ni_{32}C_6(CO)_{36}]^{n-}$ (n = 5-10) and $[Ni_{38}C_6(CO)_{42}]^{n-}$ (n = 5-9) and crystal structure of $[PPh_3Me]_6[Ni_{32}C_6(CO)_{36}]\cdot 4MeCN$, Eur. J. Inorg. Chem. (1999) 663–671.

[159] D. Collini, C. Femoni, M.C. Iapalucci, G. Longoni, P.H. Svensson, P. Zanello, tuning electronic behavior of carbonyl metal clusters by substitution of interstitial and capping atoms, Angew. Chem. Int. Ed. 114 (2002) 3837–3840.

[160] F. Demartin, F. Fabrizi de Biani, C. Femoni, M.C. Iapalucci, G. Longoni, P. Macchi, P. Zanello, Synthesis, electrochemistry and crystal structure of the $[Ni_{36}Pt_4(CO)_{45}]^{6-}$ and $[Ni_{37}Pt_4(CO)_{46}]^{6-}$ hexaanions, J. Cluster Sci. 12 (2001) 61–74.

[161] C. Femoni, M.C. Iapalucci, G. Longoni, P.H. Svensson, P. Zanello, F. Fabrizi de Biani, Synthesis, and characterization of ν_3-octahedral $[Ni_{36}Pd_8(CO)_{48}]^{6-}$ and $[Ni_{35}Pt_9(CO)_{48}]^{6-}$ clusters displaying unexpected surface segregation of Pt atoms and molecular and/or crystal substitutional Ni/Pd and Ni/Pt disorder, Chem. Eur. J. 10 (2004) 2318–2326.

[162] F. Fabrizi de Biani, C. Femoni, M.C. Iapalucci, G. Longoni, P. Zanello, A. Ceriotti, Redox behavior of $[H_{6-n}Ni_{38}Pt_6(CO)_{48}]^{n-}$ (n = 4–6) anions: a series of metal carbonyl clusters displaying electron-sink features, Inorg. Chem. 38 (1999) 3721–3724.

[163] A. Bernardi, I. Ciabatti, C. Femoni, M.C. Iapalucci, G. Longoni, S. Zacchini, Ni-Cu tetracarbide carbonyls with vacant Ni(CO) fragments as borderline compounds between molecular and quasi-molecular clusters, Dalton Trans. 42 (2013) 407–421.

[164] S. Fedi, P. Zanello, F. Laschi, A. Ceriotti, S. El Afefey, A joint electrochemical/spectroelectrochemical inspection (and re-inspection) of high-nuclearity platinum carbonyl clusters, J. Solid State Electrochem. 13 (2009) 1497–1504.

[165] C. Cesari, B. Berti, M. Bortoluzzi, C. Femoni, T. Funaioli, F.M. Vivaldi, M. C. Iapalucci, S. Zacchini, From M_6 to M_{12}, M_{19} and M_{38} molecular alloy Pt-Ni carbonyl nanoclusters: selective growth of atomically precise heterometallic nanoclusters, Dalton Trans. 52 (2023) 3623–3642.

[166] J.D. Roth, G.J. Lewis, L.K. Safford, X. Jiang, L.F. Dahl, M.J. Weaver, Exploration of the ionizable metal cluster-electride surface analogy: infrared spectroelectrochemistry of $[Pt_{24}(CO)_{30}]^n$, $[Pt_{26}(CO)_{32}]^n$, and $[Pt_{38}(CO)_{44}]^n$ (n = 0 to –10) and comparisons with potential-dependent spectra of CO adlayers on platinum surfaces, J. Am. Chem. Soc. 114 (1992) 6159–6169.

[167] R. Holze, Optical and electrochemical band gaps in mono-, oligo-, and polymeric systems: a critical reassessment, Organometallics 33 (2014) 5033–5042.

[168] G. Longoni, P. Chini, Synthesis and chemical characterization of platinum carbonyl dianions $[Pt_3(CO)_6]_n^{2-}$ (n = ~ 10, 6, 5, 4, 3, 2, 1). A new series of inorganic oligomers, J. Am. Chem. Soc. 98 (1976) 7225–7231.

[169] B.R. Barnett, A.L. Rheingold, J.S. Figueroa, Monomeric chini-type triplatinum clusters featuring dianionic and radical-anionic π*-systems, Angew. Chem. Int. Ed. 55 (2016) 9253–9258.

[170] S.M. Tiefenthaler, N. Korber, $[K([2.2.2]\text{-crypt})]K[Pt_3(\mu^2\text{-}CO)_3(PPh_3)_3]\cdot 3NH_3$ – a new *Chini*-type platinum carbonyl complex, Z. Anorg. Allg. Chem. 649 (2023) e202200286.

[171] V.G. Albano, L. Grossi, G. Longoni, M. Monari, S. Mulley, A. Sironi, Synthesis and characterization of the paramagnetic $[Ag_{13}Fe_8(CO)_{32}]^{4-}$ tetraanion: a

cuboctahedral Ag_{13} cluster stabilized by $Fe(CO)_4$ groups behaving as four-electron donors, J. Am. Chem. Soc. 114 (1992) 5708–5713.
[172] G. Pacchioni, S. Krüger, N. Rösch, Electronic structure of naked, ligated and supported transition metal clusters from 'first principles' density functional calculations, in: P. Braunstein, L.A. Oro, P.R. Raithby (Eds.), Metal Clusters in Chemistry Vol. 3, Wiley-VCH, 1999, pp. 1392–1433.
[173] I. Ciabatti, C. Femoni, M.C. Iapalucci, G. Longoni, S. Zacchini, Platinum carbonyl clusters chemistry: four decades of challenging nanoscience, J. Clust. Sci. 25 (2014) 115–146.
[174] E. Cattabriga, I. Ciabatti, C. Femoni, M.C. Iapalucci, G. Longoni, S. Zacchini, Globular molecular platinum carbonyl nanoclusters: synthesis and molecular structures of the $[Pt_{26}(CO)_{32}]^-$ and $[Pt_{14+x}(CO)_{18+x}]^{4-}$ anions and their comparison to related platinum "browns", Inorg. Chim. Acta 470 (2018) 238–249.
[175] B. Berti, M. Bortoluzzi, A. Ceriotti, C. Cesari, C. Femoni, M.C. Iapalucci, S. Zacchini, Further insights into platinum carbonyl Chini clusters, Inorg. Chim. Acta 512 (2020) 119904.
[176] C. Femoni, M.C. Iapalucci, G. Longoni, T. Lovato, S. Stagni, S. Zacchini, Self-assembly of $[Pt_{3n}(CO)_{6n}]^{2-}$ (n = 4-8) carbonyl clusters: from molecules to conducting molecular metal wires, Inorg. Chem. 49 (2010) 5992–6004.
[177] S. Bhaduri, G.K. Lahiri, D. Mukesh, H. Paul, K. Sarma, Kinetic investigations on the redox reactions of platinum carbonyl clusters with dihydrogen and acid, Organometallics 20 (2001) 3329–3336.
[178] G.J. Lewis, J.D. Roth, R.A. Montag, L.K. Safford, X. Gao, S.-C. Chang, L.F. Dahl, M. J. Weaver, Electroactive metal clusters as models of electrode surfaces: vibrational spectroelectrochemistry of seven redox forms of $[Pt_{24}(CO)_{30}]^n$ (n = 0 to –6) and comparison with potential-dependent spectra of CO chemisorbed on platinum, J. Am. Chem. Soc. 112 (1990) 2831–2832.
[179] A. Ceriotti, P. Macchi, A. Sironi, S. El Afefey, M. Daghetta, S. Fedi, F. Fabrizi de Biani, R. Della Pergola, Cooperative effects of electron donors and acceptors for the stabilization of elusive metal cluster frameworks: synthesis and solid-state structure of $[Pt_{19}(CO)_{24}(\mu_4\text{-}AuPPh_3)_3]^-$ and $[Pt_{19}(CO)_{24}\{\mu_4\text{-}Au_2(PPh_3)_2\}_2]$, Inorg. Chem. 52 (2013) 1960–1964.
[180] C. Cesari, C. Femoni, T. Funaioli, M.C. Iapalucci, I. Rivalta, S. Ruggieri, S. Zacchini, Heterometallic rhodium clusters as electron reservoirs: Chemical, electrochemical, and theoretical studies of the centered-icosahedral $[Rh_{12}E(CO)_{27}]^{n-}$ atomically precise carbonyl compounds, J. Chem. Phys. 155 (2021) 104301.
[181] C. Femoni, M.C. Iapalucci, G. Longoni, C. Tiozzo, S. Zacchini, B.T. Heaton, J. A. Iggo, P. Zanello, S. Fedi, M.V. Garland, C. Li, The loss of CO from $[Rh_{12}(\mu_{12}\text{-}Sn)(CO)_{27}]^{4-}$: synthesis, spectroscopic and structural characterization of the electron-deficient, icosahedral $[Rh_{12}(\mu_{12}\text{-}Sn)(CO)_{25}]^{4-}$ and $[Rh_{12}(\mu_{12}\text{-}Sn)(CO)_{26}]^{4-}$ tetra-anions, Dalton Trans. (2009) 2217–2223.
[182] F. Ragaini, J.-S. Song, D.L. Ramage, G.L. Geoffroy, G.A.P. Yap, A.L. Rheingold, Radical processes in the reduction of nitrobenzene promoted by iron carbonyl clusters. X-ray crystal structures of $[Fe_3(CO)_9(\mu_3\text{-}NPh)]^{2-}$, $[HFe_3(CO)_9(\mu_3\text{-}NPh)]^-$, and the radical anion $[Fe_3(CO)_{11}]^-$, Organometallics 14 (1995) 387–400.
[183] C. Cesari, M. Bortoluzzi, C. Femoni, M.C. Iapalucci, S. Zacchini, One-pot atmospheric pressure synthesis of $[H_3Ru_4(CO)_{12}]^-$, Dalton Trans. 50 (2021) 9610–9622.
[184] J. Fu, G.J. Moxey, M. Morshedi, A. Barlow, M.D. Randles, P.V. Simpson, T. Schwich, M.P. Cifuentes, M.G. Humphrey, Mixed-metal cluster chemistry. 37. Synthesis, structural, spectroscopic, electrochemical, and optical power limiting studies of tetranuclear molybdenum-iridium clusters, J. Organomet. Chem. 812 (2016) 135–144.
[185] S. Alvarez, P. Alemany, D. Casanova, J. Cirera, M. Llunell, D. Avnir, Shape maps and polyhedral interconversion paths in transition metal chemistry, Coord. Chem. Rev. 249 (2005) 1693–1708.
[186] T. Lu, F. Chen, Calculation of molecular orbital composition, Acta Chim. Sin. 69 (2011) 2393–2406.
[187] C.R. Wick, T. Clark, On bond-critical points in QTAIM and weak interactions, J. Mol. Mod. (2018) 24 142.
[188] B. Tulyathan, W.E. Geiger, Multielectron processes involving structural changes. the two-electron reduction of $Os_6(CO)_{18}$, J. Am. Chem. Soc. 107 (1985) 5960–5967.
[189] P.L. Rodríguez-Kessler, A. Muñoz-Castro, Structure search for transition metal clusters. Towards a rational understanding of their size-dependent properties, Inorg. Chim. Acta 574 (2025) 122376.
[190] C. Bannwarth, S. Ehlert, S.J. Grimme, Chem. Theory Comput. 15 (2019) 1652–1671.
[191] J. Cuni, N. Tarrat, F. Spiegelman, A. Huguenot, M. Rapacioli, Density-functional tight-binding approach for metal clusters, nanoparticles, surfaces and bulk: application to silver and gold, J. Phys.: Condens. Matter 30 (2018) 303001.
[192] C. Lepetit, P. Fau, K. Fajerwerg, M.L. Kahn, B. Silvi, Topological analysis of the metal-metal bond: a tutorial review, Coord. Chem. Rev. 345 (2017) 150–162.
[193] B. Berti, M. Bortoluzzi, C. Cesari, C. Femoni, M.C. Iapalucci, R. Mazzoni, F. Vacca, S. Zacchini, Polymerization isomerism in $[\{MFe(CO)_4\}_n]^{n-}$ (M = Cu, Ag, Au; n = 3, 4) molecular clusters supported by metallophilic interactions, Inorg. Chem. 58 (2019) 2911–2915.
[194] T. Tsuneda, J.-W. Song, S. Suzuki, K. Hirao, On Koopmans' theorem in density functional theory, J. Chem. Pyhs. 133 (2010) 174101.
[195] V.L. Chevrier, S.P. Ong, R. Armiento, M.K.Y. Chan, G. Ceder, Hybrid density functional calculations of redox potentials and formation energies of transition metal compounds, Phys. Rev. B 82 (2010) 075122.
[196] R. Jono, Y. Tateyama, K. Yamashita, Phys. Chem. Chem. Phys. 17 (2015) 27103–27108.
[197] H. Harb, R.S. Assary, Systematic improvement of redox potential calculation of Fe (III)/Fe(II) complexes using a three-layer micro-solvation model, Phys. Chem. Chem. Phys. 27 (2025) 10717–10729.
[198] J.R. Schmidt, N. Shenvi, J.C. Tully, Controlling spin contamination using constrained density functional theory, J. Chem. Phys. 129 (2008) 114110.
[199] A.D. Becke, Perspective: Fifty years of density-functional theory in chemical physics, J. Chem. Phys. 140 (2014) 18A301.
[200] C. Femoni, M.C. Iapalucci, G. Longoni, C. Tiozzo, J. Wolowska, S. Zacchini, E. Zazzaroni, New hybrid semiconductor materials based on viologen salts of bimetallic Fe-Pt and Fe-Au carbonyl clusters: first structural characterization of the diradical π-dimer of the diethylviologen monocation and EPR evidence of its triplet state, Chem. Eur. J. 13 (2007) 6544–6554.
[201] A. Rahaman, G.C. Lisensky, J. Browder-Long, D.A. Hrovat, M.G. Richmond, E. Nordlander, G. Hogarth, Electrocatalytic proton-reduction behavior of telluride-capped triiron clusters: tuning of overpotentials and stabilization of redox states relative to lighter chalcogenide analogues, Dalton Trans. 49 (2020) 7133–7143.
[202] A. Bernardi, C. Femoni, M.C. Iapalucci, G. Longoni, F. Ranuzzi, S. Zacchini, P. Zanello, S. Fedi, Synthesis, molecular structure and properties of the $[H_{6-n}Ni_{30}C_4(CO)_{34}(CdCl)_2]^{n-}$ (n = 3-6) bimetallic carbide carbonyl cluster: a model for the growth of noncompact interstitial metal carbides, Chem. Eur. J. 14 (2008) 1924–2934.
[203] I. Ciabatti, F. Fabrizi de Biani, C. Femoni, M.C. Iapalucci, G. Longoni, S. Zacchini, Metal segregation in bimetallic Co-Pd carbide carbonyl clusters: synthesis, structure, reactivity and electrochemsitry of $[H_{6-n}Co_{20}Pd_{16}C_4(CO)_{48}]^{n-}$ (n = 3-6), ChemPlusChem 78 (2013) 1456–1465.
[204] F. Forti, C. Cesari, M. Bortoluzzi, C. Femoni, M.C. Iapalucci, S. Zacchini, Heterometallic Ru-Ir carbonyl clusters as catalyst precursors for hydrogenation and hydrogen transfer reactions, New J. Chem. 47 (2023) 19289–19303.
[205] C. Cesari, I. Ciabatti, C. Femoni, M.C. Iapalucci, S. Zacchini, Capping $[H_{8-n}Ni_{42}C_8(CO)_{44}]^{n-}$ (n = 6, 7, 8) octacarbide carbonyl nanoclusters with [Ni(CO)] and [CuCl] fragments, J. Clust. Sci. 28 (2017) 1963–1979.
[206] B. Berti, I. Ciabatti, C. Femoni, M.C. Iapalucci, S. Zacchini, Cluster core isomerism induced by crystal packing effects in the $[HCo_{15}Pd_9C_3(CO)_{38}]^{2-}$ molecular nanocluster, ACS Omega 3 (2018) 13239–13250.
[207] A. Bernardi, I. Ciabatti, C. Femoni, M.C. Iapalucci, G. Longoni, S. Zacchini, Molecular nickel poly-carbide carbonyl nanoclusters: the octa-carbide $[HNi_{42}C_8(CO)_{44}(CuCl)]^{7-}$ and the deca-carbide $[Ni_{45}C_{10}(CO)_{46}]^{6-}$, J. Organomet. Chem. 812 (2016) 229–239.
[208] M. Bortoluzzi, I. Ciabatti, C. Femoni, M. Hayatifar, M.C. Iapalucci, S. Zacchini, $[H_{3-n}Fe_4(CO)_{12}(IrCOD)]^{n-}$ (n = 1, 2) and "$[H_2Fe_3(CO)_{10}(IrCOD)]^-$ bimetallic Fe-Ir hydride carbonyl clusters", Organometallics 34 (2015) 189–197.
[209] I. Ciabatti, C. Femoni, M.C. Iapalucci, G. Longoni, S. Zacchini, Tetrahedral $[H_nPt_4(CO)_4(P\hat{}P)_2]^{n+}$ (n = 1,2; P^P = CH_2=C(PPh_2)$_2$) cationic mono- and dihydrido carbonyl clusters obtained by protonation of the neutral $Pt_4(CO)_4(P\hat{}P)_2$, Organometallics 32 (2013) 5180–5189.
[210] I. Ciabatti, C. Femoni, M.C. Iapalucci, G. Longoni, S. Zacchini, Bimetallic nickel-cobalt hexacarbido carbonyl clusters $[H_{6-n}Ni_{22}Co_6C_6(CO)_{36}]^{n-}$ (n = 3-6) possessing polyhidride nature and their base-induced degradation to the monoacetylide $[Ni_9CoC_2(CO)_{16-x}]^{3-}$ (x = 0, 1), Organometallics 31 (2012) 4593–4600.
[211] I. Ciabatti, C. Femoni, M.C. Iapalucci, G. Longoni, S. Zacchini, S. Zarra, Surface decorated platinum carbonyl clusters, Nanoscale 4 (2012) 4166–4177.
[212] A. Bernardi, C. Femoni, M.C. Iapalucci, G. Longoni, S. Zacchini, The problems of detecting hydrides in metal carbonyl clusters by ^{1}H NMR: the case study of $[H_{4-n}Ni_{22}(C_2)_4(CO)_{28}(CdBr)_2]^{n-}$ (n = 2-4), Dalton Trans. 4245-4251 (2009).
[213] I. Ciabatti, F. Fabrizi de Biani, C. Femoni, M.C. Iapalucci, G. Longoni, S. Zacchini, Selective synthesis of the $[Ni_{36}Co_8C_8(CO)_{48}]^{6-}$ octa-carbide carbonyl cluster by thermal decomposition of the $[H_2Ni_{22}Co_6C_6(CO)_{36}]^{4-}$ hexa-carbide, Dalton Trans. 42 (2013) 9662–9670.
[214] M. Sellin, C. Friedmann, M. Mayländer, S. Richert, I. Krossing, Towards clustered carbonyl cations $[M_3(CO)_{14}]^{2+}$ (M = Ru, Os): the need for innocent deelectronation, Chem. Sci. 13 (2022) 9147–9158.
[215] Y.-H. Li, C.-H. Lin, H.-L. Chen, E.-C. Yang, M. Shieh, Stabilization of Sb_4 tetrahedra in paramagnetic transition metal carbonyl complexes, J. Am. Chem. Soc. 147 (2025) 9043–9048.
[216] Y.-H. Liu, C.-C. Li, W.-K. Cheng, Y.-H. Li, R.Y. Lin, M. Shieh, Paramagnetic semiconducting Se-Mn clusters: a Mn_3Se_4-stabilized selenide radical intermediate and its aggregated derivatives, Inorg. Chem. 61 (2022) 20433–20444.
[217] C. Cesari, M. Bortoluzzi, C. Femoni, M.C. Iapalucci, S. Zacchini, Synthesis, molecular structure and fluxional behavior of the elusive $[HRu_4(CO)_{12}]^{3-}$ carbonyl anion, Dalton Trans. 51 (2022) 2250–2261.
[218] M. Bortoluzzi, I. Ciabatti, C. Cesari, C. Femoni, M.C. Iapalucci, S. Zacchini, Synthesis of the highly reduced $[Fe_6C(CO)_{15}]^{4-}$ carbonyl carbide cluster and its reactions with H^+ and $[Au(PPh_3)]^+$, Eur. J. Inorg. Chem. (2017) 3135–3143.
[219] C. Femoni, M.C. Iapalucci, G. Longoni, S. Zacchini, S. Zarra, New findings in the chemistry of iron carbonyls: the previously unreported $[H_{4-n}Fe_4(CO)_{12}]^{n-}$ (n = 1, 2) series of clusters, which fills the gap with ruthenium and osmium, Inorg. Chem. 48 (2009) 1599–1605.
[220] F. Forti, A. Pellegrini, C. Cesari, C. Femoni, M.C. Iapalucci, M. Mancinelli, S. Zacchini, Single-step insertion of organic sulfur into a Fe_6C carbide carbonyl cluster, including the natural amino acid *L*-cysteine: vibrational circular dichroism and chirality transfer, Angew. Chem Int. Ed. 64 (2025) e202513702.
[221] B.F.G. Johnson, J. Lewis, W.J.H. Nelson, J. Puga, P.R. Raithby, M. Schröder, K. H. Whitmire, Synthesis and X-ray crystal structure of the cluster cation $[Os_4(\mu_2\text{-}$

H)$_3$(CO)$_{12}$(NCMe)$_2$]$^+$: an example of an unsupported butterfly Os$_4$ geometry, J. Chem. Soc., Chem. Commun. (1982) 610–612.
[222] M.E. Prater, L.E. Pence, R. Clerac, G.M. Finniss, C. Campana, P. Auban-Senzier, D. Jerome, E. Canadell, K.R. Dunbar, A remarkable family of rhodium acetonitrile compounds spanning three oxidation states and with nuclearities ranging from mononuclear and dinuclear to one-dimensional chains, J. Am. Chem. Soc. 121 (1999) 8005–8016.
[223] I. Ciabatti, C. Femoni, M.C. Iapalucci, G. Longoni, S. Zacchini, S. Fedi, F. Fabrizi de Biani, Synthesis, structure, and electrochemistry of the Ni-Au carbonyl Cluster [Ni$_{12}$Au(CO)$_{24}$]$^{3-}$ and its relation to [Ni$_{32}$Au$_6$(CO)$_{44}$]$^{6-}$, Inorg. Chem. 51 (2012) 11753–11761.
[224] A. Taheri, L.A. Berben, Making C-H bonds with CO_2: production of formate by molecular electrocatalysts, Chem. Commun. 52 (2016) 1768–1777.
[225] A. Taheri, L.A. Berben, Tailoring electrocatalysts for selective CO_2 or H^+ reduction: iron carbonyl clusters as a case study, Inorg. Chem. 55 (2016) 378–385.
[226] N.D. Loewen, S. Pattanayak, R. Herber, J.C. Fettinger, L.A. Berben, Quantification of the electrostatic effect on redox potential by positive charges in a catalyst microenvironment, J. Phys. Chem. Lett. 12 (2021) 3066–3073.
[227] N.D. Loewen, E.J. Thompson, M. Kagan, C.L. Banales, T.W. Myers, J.C. Fettinger, L.A. Berben, A pendant proton shuttle on [Fe$_4$N(CO)$_{12}$]$^-$ alters product selectivity in formate *vs.* H_2 production the hydride [H–Fe$_4$N(CO)$_{12}$]$^-$, Chem. Sci. 7 (2016) 2728–2735.
[228] C. Li, A. Rahaman, W. Lin, H. Mourad, J. Meng, A. Honarfar, M. Abdellah, M. Guo, M.G. Richmond, K. Zheng, E. Nordlander, Electron transfer mediated by iron carbonyl clusters enhance light-driven hydrogen evolution in water by quantum dots, ChemSusChem 13 (2020) 3252–3260.
[229] S. Ghosh, G. Hogarth, Trinuclear clusters containing 2-aminopyridinate/pyrimidinate ligands as electrocatalysts for proton reduction, J. Organomet. Chem. 851 (2017) 57–67.